

wearHEALTH group  
Department of Computer Science  
University of Kaiserslautern

---

# Master's Thesis

---

**Towards Inertial Musculoskeletal Analysis:  
Effects of Sensor-to-Segment Calibration  
on Predicted Ground Reaction Forces**

---

Felix Laufer  
June 06, 2017

---



# Master's Thesis

## **Towards Inertial Musculoskeletal Analysis: Effects of Sensor-to-Segment Calibration on Predicted Ground Reaction Forces**

wearHEALTH group  
Department of Computer Science  
University of Kaiserslautern

Felix Laufer

<b>Day of issue:</b>	6th of December 2016
<b>Day of release:</b>	6th of June 2017

<b>First Reviewer:</b>	Prof. Dr. Karsten Berns
<b>Second Reviewer:</b>	Dr. Bertram Taetz
<b>Supervisor:</b>	Dr. Bertram Taetz



Hereby I declare that I have self-dependently composed the Master's Thesis at hand. The sources and additives used have been marked in the text and are exhaustively given in the bibliography.

June 06, 2017 – Kaiserslautern

(Felix Laufer)



# Contents

<b>1</b>	<b>Introduction and Motivation</b>	<b>1</b>
1.1	Musculoskeletal Simulation and Analysis . . . . .	1
1.2	Motivation and Research Context . . . . .	3
1.3	Thesis Scope and Goals . . . . .	4
1.4	Overview . . . . .	4
<b>2</b>	<b>Foundations and Related Work</b>	<b>5</b>
2.1	Musculoskeletal Modeling . . . . .	5
2.1.1	Skeleton Graph . . . . .	5
2.1.2	Configuration Space Representations . . . . .	6
2.1.3	Anatomical Constraints . . . . .	8
2.1.4	Body Model Parameters . . . . .	11
2.1.5	Model Scaling . . . . .	12
2.1.6	Muscles . . . . .	12
2.2	Motion Capture . . . . .	14
2.2.1	Approaches in Human Motion Capture . . . . .	14
2.2.2	Optical Marker-Based Motion Capture . . . . .	15
2.2.3	Inertial Motion Capture . . . . .	16
2.2.4	Inertial Measurement Units . . . . .	17
2.2.5	Sensor Fusion . . . . .	19
2.3	Inverse Kinematics . . . . .	22
2.3.1	Marker-Driven Kinematics . . . . .	23
2.3.2	IMU-Driven Kinematics: Quattracker . . . . .	24
2.4	Inverse Dynamics . . . . .	26
2.4.1	Equations of Motion . . . . .	26
2.4.2	Ground Reaction Forces . . . . .	28
2.5	Static Optimization . . . . .	29
2.5.1	Muscular Redundancy Problem . . . . .	29
2.5.2	Muscle Recruitment Optimization . . . . .	30
2.6	Outline: IMU-Driven Musculoskeletal Analysis . . . . .	32

<b>3</b>	<b>Conception and Implementation</b>	<b>35</b>
3.1	Conceptual Methodology . . . . .	35
3.1.1	AMS Musculoskeletal Analysis Framework . . . . .	36
3.1.2	Ground Reaction Force Prediction . . . . .	38
3.1.3	Simulation of I2S Calibration Errors . . . . .	40
3.1.4	IMU-Trackable Anatomical Skeleton . . . . .	41
3.1.5	Design Overview . . . . .	43
3.2	Implementation Details . . . . .	44
3.2.1	Subsystems and Interfaces . . . . .	44
3.2.2	Pipeline Framework . . . . .	45
3.2.3	AMS GRF Prediction Integration . . . . .	46
3.2.4	Ground and Foot Marker Plane Correction . . . . .	47
<b>4</b>	<b>Study Design and Evaluation</b>	<b>49</b>
4.1	Setup . . . . .	49
4.1.1	Substudies . . . . .	49
4.1.2	Methods and Materials . . . . .	51
4.2	Results . . . . .	54
4.2.1	Functional Tests and GRF Prediction Validation . . . . .	54
4.2.2	Foot Posture Sensitivity . . . . .	55
4.2.3	I2S Calibration Errors . . . . .	56
4.2.4	Typical I2S Calibration Error Scenario . . . . .	63
4.2.5	Skeleton Trackability . . . . .	67
<b>5</b>	<b>Discussion and Outlook</b>	<b>69</b>
5.1	Conclusion . . . . .	69
5.2	Future Work . . . . .	70
	<b>Bibliography</b>	<b>73</b>
<b>A</b>	<b>Appendix</b>	<b>81</b>
A.1	Figures . . . . .	81
A.2	AMS Hill Type Muscle Model . . . . .	85
A.3	Shoulder and Spine Rhythm . . . . .	86
A.4	Qualitative I2S Error Distributions . . . . .	87



# 1. Introduction and Motivation

An essential branch within the growing field of computational biomechanics is the simulation and analysis of the human musculoskeletal anatomy. Various scientific and industrial areas of application benefit from the capability to evaluate the response of a biomechanical system's inner variables to certain physiological stresses or during any systemic or environmental conditions in a non-invasive, ethical and cost-effective manner. Diagnosis of musculoskeletal disorders, treatment planning and simulation within the fields of orthopedic and sports medicine as well as surgery are traditionally scenarios, where deep insights into the musculoskeletal system are required. The design of implants and prostheses or the analysis and optimization of motion sequences from a perspective of sports science are further typical applications. However, there is also a growing demand for biomechanical simulation in the scope of industrial ergonomics, human computer interaction and robotics.

## 1.1 Musculoskeletal Simulation and Analysis

Musculoskeletal analysis and simulation, in general, aim at understanding internal mechanisms of the musculoskeletal systems of living creatures while performing movements or being exposed to external, environmental forces. It promises to provide insights into anatomical variables and properties, which would typically require costly, inconvenient or invasive methods or cannot be measured in vivo at all. Hence, comprehensive models of an anatomy, i.e. the bones, muscles, tendons, ligaments and occasionally the neural system, are both a requirement and a research result. Various computational approaches exist, which address different aspects within this broad field; however, they might be classified into two major methodologies:

Forward dynamics or simulation estimates motions resulting from prescribed muscle activations that may be enriched with or are solely based on electromyography (EMG) measurements. Based on that, simulated motor patterns are used to drive a muscle actuated skeletal model [Barrett 07, Jonkers 02, Demircan 09, Sartori 12]. Dynamic optimization methods initiate a goal definition of motor tasks and apply aspects of optimal control theory to compute motor patterns and eventually motion trajectories subject to e.g. a minimum metabolic energy expenditure. These methods are bottom-up, constructive

approaches that focus on developing models of neural activation dynamics, synergy effects and muscle recruitment strategies and their qualitative validation in terms of movement predictions and anticipated classes of movements [Davy 87, Anderson 01, Gail 15].

Inverse dynamics or analysis, in contrast, is an analytical, top-down method, that takes measured motion sequences as an input and determines the inverse kinematics with respect to a skeletal model, i.e. the positions and orientations of all skeletal segments at each point in time. In a subsequent stage, eponymic for the entire method, classical equations of motion are solved for the net moments of forces at the segments' joints, which are then distributed among potentially several muscles spanning the respective joints subject to an optimality criterion. The latter stage is often referred to as static optimization where an optimization is performed, that minimizes the total muscle stress following the assumption of an efficient muscle recruitment. An also analytic but somewhat hybrid approach is computed muscle control (CMC), which repeatedly computes muscle activations, using static optimization in each time step, and then drives a dynamic musculoskeletal model forwardly towards the prescribed kinematic trajectories, following a PD control law [Thelen 03, Thelen 06].

### Musculoskeletal Analysis Pipeline

The inverse, analytic paradigm, mentioned above, provides the basis for clinical gait analyses, which aim to either gain deeper fundamental knowledge on the human gait in general or to diagnose and treat posture and movement-related disorders of individuals. To this end, a subject's motion is investigated in terms of various biomechanical parameters, such as anatomical joint angle trajectories, joint reaction forces and/or muscle activation patterns. In detail, a subject's motion is firstly captured (MoCap) and the inverse kinematics (IK) is computed with respect to a subject-scaled, anatomical skeleton model. Subsequently, the equations of motions are solved for net joint forces and moments, typically using measured ground reaction forces and moments or additional external forces (ID), and finally muscle activations are often estimated on the assumption of an somehow optimal muscle recruitment (SO). As to that, a rich, subject-tailored body model, including an anatomical skeleton with bone masses and moments of inertia and integrated muscle models, is necessary. Figure 1.1 shows the generic musculoskeletal analysis pipeline and the particular artifacts, i.e. the required measurements and models and the results of each process stage.

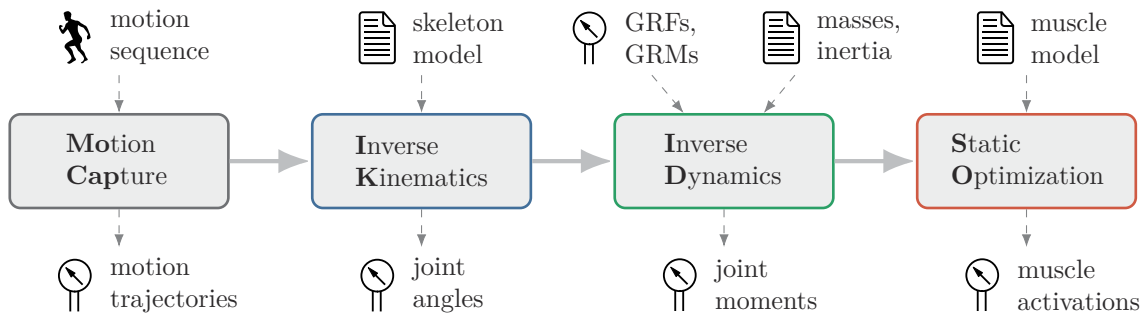


**Figure 1.1:** The generic musculoskeletal analysis pipeline.

## 1.2 Motivation and Research Context

The wearHEALTH group at the University of Kaiserslautern pursues the goal of developing mobile healthcare systems, whereat one major focus of research is on wearable systems for motion analyses in musculoskeletal rehabilitation. Suchlike ambulatory systems are envisaged to support physicians and physiotherapists during gait assessments through objective and reliable measures of biomechanical variables as well as patients during therapeutic exercises by providing an immediate, user-specific feedback. To this end, similar to clinical gait analyses, kinematic and kinetic movement parameters such as joint angle trajectories, joint and ground reaction forces, but also muscle activations, shall be captured and assessed. In contrast to conventional systems, the emphasis at this is laid on mobility, flexibility, usability and a real-time data acquisition and processing [wearHEALTH 15].

Traditionally, clinical gait analysis relies on the resources of a gait laboratory, which include an optical marker-based motion capture system, composed of several cameras and force plates required for ground reaction force measurements. These devices are usually stationary mounted in order to provide an adequate measuring precision, without too much setup and calibration effort. However, an initial calibration procedure for each new trial and subject is usually mandatory. This includes the attachment of several markers at the subject's bony landmarks, which demands some anatomical knowledge of the personnel and patience of the subject. In summary, these conditions of classical, golden standard motion capture procedures do not meet the requirements of a flexible and user-friendly ambulatory system very well [Lohnert 10].

Recently, integrated inertial and magnetic field sensors are emerging as a promising, inherently flexible alternative in motion capture, while progressively also satisfying higher demands on precision. Whereas wearable sensor hardware is available for quite some time [Roetenberg 06, Roetenberg 09, Young 10], clinical human motion capture systems driven with inertial measurement units and their implications on musculoskeletal analysis results are still in a stage of research [Fusion3D 09, Koning 11]. This derives on the one hand from the fact, that an adequate tracking precision is only achieved in combination of both, a high physical sensor measurement accuracy, but most notably a sophisticated sensor fusion algorithm. On the other hand, suchlike systems imply different sources of errors, compared to the optical marker-based standard, where effects of marker placement deviations on biomechanical parameters are well known and convenient marker protocols are developed [Leardini 05, Della Croce 06]. In particular, determining the calibration of sensors to the body segments is more challenging than palpating bony landmarks and attaching markers. Although some protocol standards for inertial systems have been proposed, e.g. in [Garofalo 10], they mainly focus on ensuring precision of resulting kinematic trajectories. These are, however, input to the further biomechanical analysis stages, and the influence of calibration errors on kinetic parameters such as reaction forces, but also muscle activations are still poorly understood.

In order to develop an easy usable, preferably autonomous, but yet reliable analysis technique, a self-configuring system that adjust itself to the anthropometric characteristics of the user, including the sensor positioning relative to the body segments, is intended, and approaches towards self-calibrating sensors have been proposed in [Taetz 16] and [Zimmermann 17]. However, any kinetic gait investigations still require knowledge of the ground reaction forces. A truly flexible, ambulatory system should not be dependent on rather inconvenient force plate measuring devices.

### 1.3 Thesis Scope and Goals

With the above mentioned requirements and challenges of an ambulatory musculoskeletal analysis system in mind, the goal of this thesis are twofold: As a basis for any flexible analysis, the limitations of conventional musculoskeletal analysis for this use case shall be minimized. These are firstly the restrictions of some established approaches to optical marker-based data and the dependency on ground reaction force measurements. Hence, an analysis pipeline driven with—in the first instance simulated—inertial motion capture data, and relying on a universal ground reaction force estimation method proposed in [Fluit 14] and [Skals 16], shall be conceptualized and finally taken into operation. The focus at this is on the genericity of the particular methods and the overall system.

The second goal is an investigation of the effects of sensor-to-segment calibration errors as one major source of errors on predicted ground reaction forces and eventually on muscle activations. To this end, calibration errors shall be systematically simulated and evaluated using the implemented analysis pipeline. In order to obtain a realistic impression of suchlike errors, inherent in inertial motion capture, it is important to not confuse them with any additional errors, which might also result in distortions of the kinematic trajectories, but are indeed induced due to modeling errors or any incautious utilization of methods that were technically designed for marker-based motion analyses.

By this means, this thesis aims at providing a contribution towards the long-term goal of a flexible inertial musculoskeletal analysis system, where the analysis pipeline implemented within this scope, must be seen as a proof of concept. The evaluation of sensor-to-segment calibration errors on predicted ground reaction forces may guide the development of self-calibration approaches and the determination of required precision targets. Moreover, it may and give an indication of the distortion of biomechanical analysis results to be expected from a suchlike procedure.

### 1.4 Overview

The thesis is structured into three major parts: To begin with, an overview of the theoretical foundations of musculoskeletal analysis and state of the art solution approaches to both, a conventional marker-based and a pipeline instantiation driven with inertial data, is given in chapter 2. The kind reader, who is familiar with those techniques, might want to skip this chapter. However, it should be noted that the concepts introduced in the sections on inertial motion capture and inverse kinematics as well as the notes in the outline might be essential in order to comprehend and asses the conceptualized system.

The conception and implementation details of the proposed analysis pipeline are discussed in chapter 3. These include a description of the utilized musculoskeletal analysis framework and the integration of the ground reaction force prediction method as well as the simulation of inertial sensor trajectories with calibration errors.

Finally, the pipeline itself and the conducted analyses are evaluated in chapter 4, where the setup of all substudies, the parametrization of methods, the used materials and the results are presented. An overall, summarizing conclusion is drawn in chapter 5, where also limitations of the proposed method as well as resultant issues and required further work is discussed.

## 2. Foundations and Related Work

This chapter is conceived to provide an overview of foundations and formalisms in musculoskeletal modeling as well as the steps involved in musculoskeletal analysis. The musculoskeletal analysis pipeline, describing a blueprint for this inverse, analytical paradigm, will be discussed in detail together with its particular process stages and appropriate solution approaches.

### 2.1 Musculoskeletal Modeling

Musculoskeletal analysis requires an adequate modeling of its object of interest—the (human) body. For convenience, a biomechanical system is modeled as a set of rigid bodies, representing the body segments and its properties of relevance. Hence, musculoskeletal analysis, and biomechanics in general, make an essential use of methods from the field of rigid body modeling and dynamics.

#### 2.1.1 Skeleton Graph

A model of the skeleton is a very first approximation of a body's anatomy and crucial for any further model refinements. It aims to provide an abstraction from the real skeleton by incorporating only major skeletal bones and their connecting joints, which are required to provide a sufficient kinematic model of a certain subject for a particular motion of interest. Bones are modeled as straight segments  $S \in \mathbb{S}$ , connected with joints  $J \in \mathbb{J}$ , consequently forming a skeleton graph  $G_{skel} = (\mathbb{S}, \mathbb{J})$ , with the segments as the nodes and the joints as the edges. Each segment holds a local Cartesian coordinate system (frame), in which segment points  $p^S \in \mathbb{R}^3$  can be defined. Segments are connected via joints at some of their segment points. Additional segment points may refer to any anatomical landmarks of interest. In general, a joint is associated with, at least, two segment points of different segments. However, it is convenient to allow exactly two interconnected segments per joint, so that a joint  $J_{i,j}$  can be described with its point set  $P^{J_{i,j}} = \{p_m^{S_i}, p_n^{S_j}\}$ , with  $p_m^{S_i}, p_n^{S_j}$  two segment points of different segments  $S_i, S_j, i \neq j$ . Furthermore, a skeleton graph is assumed to be connected and acyclic, and thus constitutes a tree, also often referred to as kinematic tree or kinematic chain, where the pelvis is naturally chosen to be the root segment as shown in figure 2.1.

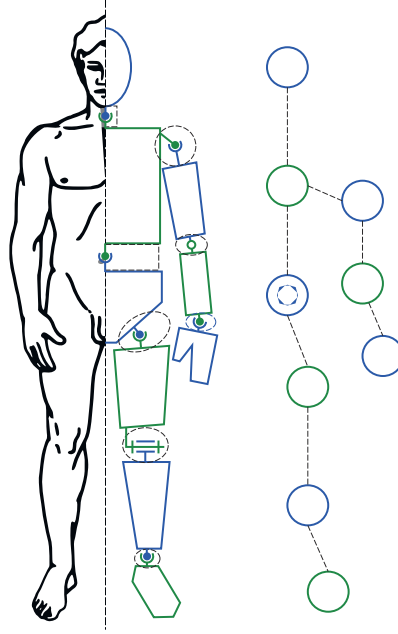


**Figure 2.1:** Skeleton graph with pelvic root node; adapted from [Wikimedia Commons 10].

### 2.1.2 Configuration Space Representations

While the aforementioned graph determines the topology of a skeleton model, a representation of the spatial configuration of segments in a real coordinate space is required in order to describe the skeleton's kinematics. A single segment's spatial configuration can be described by its pose composed of the position and orientation in respect to a reference frame. Generally, let  $A, B$  be two Cartesian coordinate systems, then  $A^B \in \mathbb{R}^3$  denotes the translation and  $R^{AB} \in SO(3)$  denotes the orientation of frame  $A$  in frame  $B$ . Alternatively, the rotation matrix  $R^{AB}$  can be represented as a unit quaternion  $q_R^{AB}$ . The inverse rotation is denoted  $(R^{AB})^T = R^{BA}$  or  $(q_R^{AB})^* = q_R^{BA}$ , respectively. Rotations may also be expressed interchangeably by Euler angles or axis-angle representations. Rotation and translation  $[R^{AB}, A^B]$  can be combined into a single matrix known as the homogenous transformation  $H^{AB}$ .

#### Free Segments Model and Segment Chain Model

In a global reference frame  $G$ , the pose of segment  $S$  is consequently  $H^{GS}$ , and the entire skeleton's kinematic state in 3-dimensional real coordinate space is described by the set  $\{H^{GS} | S \in \mathbb{S}\}$ . This representation is known as the free segments model and imposes no constraints on the segment's relative poses, thus especially allowing for arbitrary displacements between joint endpoints of topologically adjacent segments.

However, it might be sensible to model strict connections, so that joint endpoints are forced to coincide, which leads to another kinematic state representation: For the root segment still the global pose  $H^{GS^{(root)}}$  is required, whereas the zero displacement constraint ensures that only the relative orientations between all remaining adjacent segments describe their spatial states sufficiently. They can be obtained by traversing the path from the root node to the respective segment node and incorporating all relative rotations  $R^{S_i S_j}$  of parental

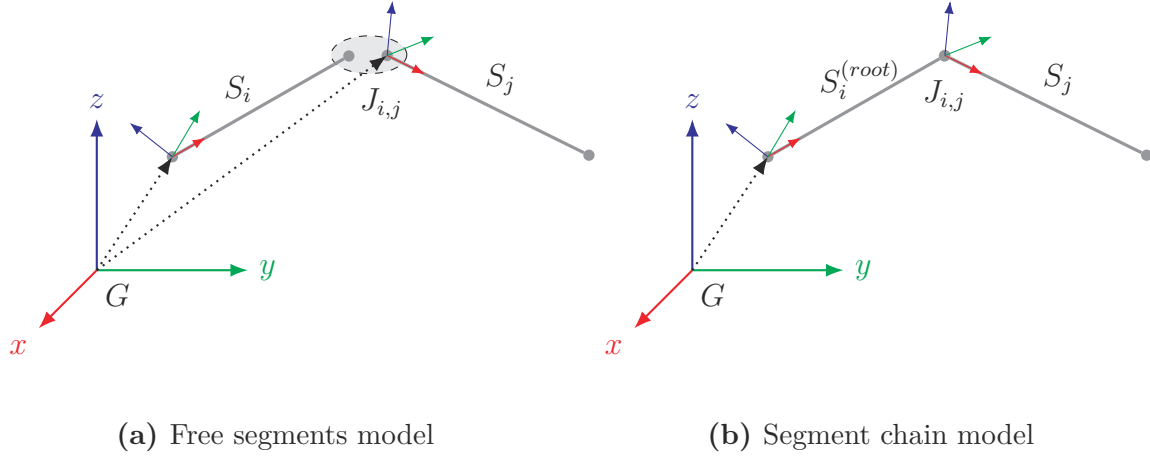


**Figure 2.2:** Two common kinematic representations in skeletal modeling.

nodes. The kinematic state is then fully described with set  $\{H^{GS^{(root)}}, R^{S_i S_j} | J_{i,j} \in \mathbb{J}\}$ . This representation is called segment chain model and is obviously a special, constrained variant of the free segments model. Both are sketched in comparison in figure 2.2.

### Constraints and Degrees of Freedom

In the free segments model, segments are thought of free rigid bodies or particles, with each three translational and rotational degrees of freedom (DoFs), in a 3-dimensional real coordinate space. The chain model, however, locks the translational DoFs by imposing the zero displacement constraint, keeping only the rotational ones. The displacement restriction is a holonomic constraint of the general form  $\gamma(x(t), t) = 0$  with  $\gamma$ , a function of (a subset of) all Cartesian segment coordinates  $x(t)$  and time  $t$ . In this case, it is time-invariant and  $\gamma(J_{i,j}) = \|p_m^{S_i} - p_n^{S_j}\| = 0$  for each joint  $J \in \mathbb{J}$ , with its linked segment endpoints  $p_m^{S_i}, p_n^{S_j}$ . Consequently,  $\{\gamma(J_{i,j}) | J \in \mathbb{J}\} \subseteq \mathbb{C}$  is the set of all displacement constraints in the model's constraint set  $\mathbb{C}$  and  $\Gamma$  is a matrix representation of the latter. Note, that  $\mathbb{C}$  is the empty set in case of the free segments model apriori, but may be extended likewise.

### Minimal Parametrizations

Now, supposed that the local segment frames are aligned with joint axes of incident joints, the model can be further constrained in terms of its natural angular degrees of freedom by simply omitting angles around the remaining axes. The common Denavit-Hartenberg (DH) convention is, for instance, a representation including this idea [Hartenberg 55]. In this way, parametrizations can be made minimal, matching the model's intended number of DoFs, and immediately providing the (anatomical) joint angles, which are of interest in most biomechanical application scenarios [Vignais 13, Bleser 15a, Bleser 15b]. Suchlike minimal orientation parametrizations, however, might suffer from singularities.

### Generalized Coordinates

Beyond denoting an alternative, more compact parametrization, the chain model is also an instance of the concept of generalized coordinates. The joint angles of a chain model where



frames are aligned with the axes of angular DoFs, for instance, are one possible choice of such a parametrization. In general, formulating appropriate transformations, Cartesian coordinates that are coupled via model constraints, and are thus not independent anymore, can be mapped to intrinsic model parameters in the respective model configuration space and vice versa. These co-called generalized coordinates are neither restricted to be Cartesian nor require a inertial reference frame. In case of a system of only holonomic constraints (holonomic system), a complete and independent, and thus minimal coordinate set, can be found (cf. [Williams 96]).

Generalized coordinates are subsequently denoted  $q(t) = (q_1(t), q_2(t), \dots, q_n(t))$  with  $n$ , the number of DoFs, and describe kinematic trajectories in the model's configuration space-time. For any fixed time  $\hat{t}$ ,  $q(t)|_{\hat{t}}$  determines the model's kinematic state in the configuration space. Kinematic trajectories of Cartesian coordinates  $r(t)$  and deduced segment transformations may now be formulated as (matrix) functions of generalized coordinates  $r(q(t))$  and  $H(r(q(t)))$ , respectively. This representation is of essential use for kinetic formulations in Lagrangian mechanics, but also for optimization based inverse kinematics [Andersen 10].

### 2.1.3 Anatomical Constraints

With the segment chain model, introduced above, and its implicit displacement restrictions, joint constraints have already been imposed on the translational DoFs between all segments. One might also want to further restrict the remaining rotational DoFs individually in order to model anatomically correct kinematics. This section will focus on the implementation of particular rotational constraints, after giving a brief overview of anatomical joint types and general constraint handling.

#### Degrees of Freedom of the Human Skeleton

The human skeleton comprises various types of joints, of which the most prominent are depicted in figure 2.3. Planar joints are found between the vertebrae of the spine or at the shoulder girdle, elbow and knee are often assumed to be hinges, elliptical joints are presumed between the radius and carpal bones of the wrist, the carpal and metacarpal bones of the thumb comprise a saddle joint, pivot joints connect the cervical vertebrae, and the hip and shoulder joints are finally prominent examples of spherical joints. Hinges and spherical joints are, by far, the most widely used types in skeletal modeling which is certainly a consequence of their relatively simple implementation. Moreover, these two types connect mainly major skeletal bones and are inevitable when modeling whole-body movements, whereas others are only of greater importance in detailed

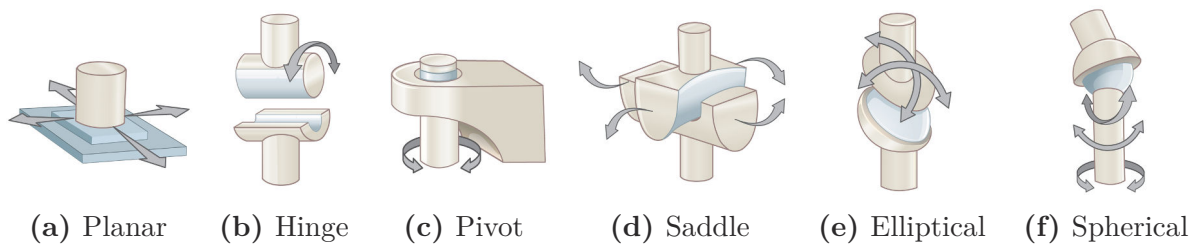


**Figure 2.3:** Schematic representation of synovial joints; figures from [OpenStax College 13].



models of particular body parts (e.g. hands incl. fingers). Some anatomical DoFs are considered passive and are known to be coupled with others as is, for instance, the case with internal knee rotation that is dependent on the flexion angle [Wilson 00]. Even so, the knee is often modeled as hinge joint for convenience [Horsman 07, Arnold 10]. Another part of the body, which is quite challenging to model, is the shoulder girdle with the sternoclavicular saddle joint and an physiological joint (muscular attachment) between clavicle and scapula [Crosbie 08]. Their respective DoFs are often modeled as functions of glenohumeral DoFs [De Groot 01, AnyBody Tech. 11]. Spinal vertebrae are mostly clustered into larger, comprising segments or even replaced by only a few virtual segments [Christophy 12]. Their relative offsets can be equality distributed based on multiple spinal measurements [Miezial 14] or approximated as functions of the overall rotation between pelvis and thorax [AnyBody Tech. 09].

### Generic Joint Constraints

Any joint may be modeled as a universal, transformational joint i.e. a spherical joint, allowing for additional displacements. However, as initially indicated, one might want to further constrain them expecting that inaccuracies resulting from motion tracking errors might be reduced with anatomically well-constrained joints. As the relative pose of any two segments  $S_i, S_j$  is described by the relative transformation  $H^{S_i S_j}$ , a connecting joint  $J_{i,j}$  may directly restrict this transformation. Note, that  $H^{S_i S_j}$  may be a matrix function of generalized coordinates (cf. equation 2.1), which then also allows to describe coupled motion (several DoFs as a function of one or more coordinates), which is supported in most musculoskeletal frameworks [OpenSim Doc. 17, AnyBody Doc. 17].

$$H^{S_i S_j}(r(q(t))) = \left[ R(\theta_x(q(t)), \theta_y(q(t)), \theta_z(q(t))), \begin{pmatrix} x(q(t)) \\ y(q(t)) \\ z(q(t)) \end{pmatrix} \right] \quad (2.1)$$

### Rotational Joints in Real Coordinate Space

For certain motion capture and inverse kinematics approaches, rotational constraints, directly expressed in real coordinate space, are often sufficient and more practical. Within optimization or filtering based approaches, constraining often implies penalizing unsatisfied

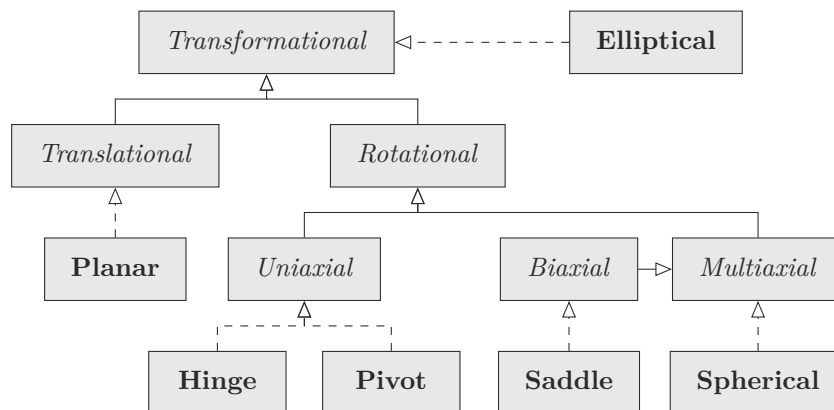


**Figure 2.4:** Functional hierarchy of joint models; cf. [Ribeiro 11].

constraints. Figure 2.4 shows a functional classification of joints, whereof the branch of rotational types is discussed subsequently.

**Uniaxial:** The uniaxial constraint is trivial supposed that the parental segment's frame is aligned with the joint axis as indicated earlier. In this case, the Euler angles associated with the two remaining axes can be penalized. If that is not possible (e.g. due to an anatomical axis not collinear with any of the technical frame axes), the fact that the rotation axis of any rotation matrix  $R$  is an eigenvector of  $R$ , corresponding to the eigenvalue one, can be exploited, and a penalty function for a relative segment rotation  $R^{S_i S_j}$  is denoted:

$$e_{axis} = a - R^{S_i S_j} a, \quad (2.2)$$

where  $a$  is the anatomical joint axis. Rotation angles outside a predefined range  $[\theta_{min}, \theta_{max}]$  can be penalized:

$$e_{range} = \begin{cases} \theta_{min} - \theta & \text{for } \theta < \theta_{min} \\ \theta - \theta_{max} & \text{for } \theta > \theta_{max} \\ 0 & \text{otherwise,} \end{cases} \quad (2.3)$$

where  $\theta = 2 \arccos([q_R^{S_i S_j}]_w)$  extracts the angle from the quaternion associated with the relative segment rotation (cf. [Miezial 16]). The method applies to both hinge and pivot joints, which can be transformed into each other.

**Multiaxial:** Handling multiaxial constraints requires a rotation decomposition around (pairwise orthogonal) rotation axis, which then can be constrained independently. This can be achieved using the so-called swing-twist decomposition which separates a rotation described by a quaternion  $q_R$  into a (possibly) 2-DoF swing and an 1-DoF twist component  $q_R = q_{R,swing} q_{R,twist}$ . One possible, straight forward method requires the twist axis to be aligned with any joint axis, here w.o.l.g the  $x$ -axis [Huyghe 11]. For a unit quaternion  $q_R = [q_R]_w + [q_R]_x i + [q_R]_y j + [q_R]_z k$  represented with its quaternion units  $i, j, k$ :

$$q_{R,twist} = \frac{[q_R]_w}{s} + \frac{[q_R]_x}{s} i \quad (2.4)$$

$$q_{R,swing} = s + \frac{[q_R]_w [q_R]_y - [q_R]_x [q_R]_z}{s} j + \frac{[q_R]_w [q_R]_z - [q_R]_x [q_R]_y}{s} k, \quad (2.5)$$

where  $s = \sqrt{w^2 + x^2}$ . The twist component can then be parametrized as Euler angle and constrained using the uniaxial method. However, constraining the swing component is more challenging. One possibility is to impose an ellipsis inequality constraint on the exponential map representation of the swing component [Grassia 98, van den Bergen 16]. With  $(\hat{j}, \hat{k})$  two basis vectors corresponding to the  $y$  and  $z$  axes of the joint frame, the swing can be reparametrized as axis-angle  $a_{R,swing} = \theta_y \hat{j} + \theta_z \hat{k}$ , where  $(\theta_y, \theta_z)$  is a vector composed of the two DoFs in the swing plane. For the two angular rotation limits  $\theta_{y,max}, \theta_{z,max}$  along both, the major and minor ellipse axes, the following constraint must hold:

$$\left( \frac{\theta_y}{\theta_{y,max}} \right)^2 + \left( \frac{\theta_z}{\theta_{z,max}} \right)^2 \leq 1 \quad (2.6)$$

Deviations from the angular limits may now be quantified through the distance of any point  $(\theta_y, \theta_z)$  to its closest point on the ellipse and penalized likewise. An approach constraining

swing rotations through a spherical polygon is discussed in [Baerlocher 01], and an overview of several methods for swing-twist decomposition is given in [Dobrowolski 15]. Biaxial joints are simply implemented omitting the twist component. Note that also uniaxial joints may be treated as the complementary case of this method.

### 2.1.4 Body Model Parameters

The modeling components introduced so far, are sufficient for purely kinematic analyses. An individual model can be instantiated by palpating the joints of a subject, measuring the joint-to-joint distances and appropriately scaling the segments. Both segment lengths and/or joint axes may be determined through an optical motion capture process, using appropriate marker protocols, that are capable of estimating joint centers and axes based on trajectories of bony landmarks. However, a further biomechanical analysis requires additional musculoskeletal models and parameters to be considered. Firstly, for any kinetic considerations also the dynamic properties of body segments must be incorporated in order to solve the equations of motion for determining the internal forces that cause the observed motion.

#### Dynamic Segment Properties

For each segment  $S_i \in \mathbb{S}$ , the mass  $m_i$ , center of mass (CoM)  $S_i^{CoM}$  and the inertia tensor  $\Theta_i$ , with respect to the CoM, must be determined. These parameters model the dynamic behavior of each body segment in its entirety, including the bone(s), related muscles and all soft tissues. Typically, they are determined through cadaver-based studies and pooled in anthropometric tables or averaged within a single, generic model, representing a certain population. Regression models can be derived from suchlike results and applied in order to estimate segment parameters according to a couple of readily identifiable predictor variables such as the subject's total mass, body height and joint-to-joint distances [Contini 63, Clauser 69, Vaughan 92].

#### Muscular System Properties

Although the above mentioned parameters are sufficient for conducting an inverse dynamics analysis in the classical sense, i.e. resolving the kinematic trajectories for their causal joint net forces and moments, an analysis of individual muscle contributions requires the modeling of muscular properties in addition. The macroscopic musculoskeletal geometry, which is, for instance, the muscle length, positioning relative to joints and tendon pathway affects the moment arm and hence the actual joint moment, generated by a certain muscle force. Furthermore, muscle intrinsic properties, such as neutral fiber lengths, pennation angles and tendon elasticity, must be defined reasonably [Horsman 07]. While section 2.1.6 will be dedicated to the conceptual modeling aspects of muscles, the focal point, at this place, is on the determination of appropriate parameters. Aside from generalized findings of cadaver-based studies and subsequent subject-specific adaptations, medical imaging techniques provide the possibility to determine individual body segment parameters in vivo [Ganley 04]. Although yielding optimal specificity, extensive personalized parameter estimations might be too time-consuming and costly in practice or even ethically questionable in case of X-ray imaging methods [Rossi 13].

### 2.1.5 Model Scaling

Building a musculoskeletal model from scratch would require all of the steps, indicated above, including cadaver dissections, a large-scale medical imaging analyses or an extensive meta-study of existing data. The results of suchlike research is often aggregated in form of a musculoskeletal meta-model, which is, to a certain degree, representative with respect to a particular population. A subject-tailored model is then instantiated by adjusting all the kinematic, dynamic and muscular body model parameters in a process called model scaling. Typically, this is a semi-automatic process, incorporating anthropometric measurements of the subject, kinematic marker trajectories and possibly medical images as inputs for an estimation of the skeletal dimensions. Subsequently, a fully parametrized subject model with estimated dynamic and muscular properties, based on the skeletal scaling, is generated and may be manually refined afterwards [OpenSim Doc. 17, AnyBody Doc. 17].

#### Kinematic Scaling

Formerly, kinematic model parameters, i.e. joint centers and axes, have been mainly determined through optical marker protocols, where the observed trajectories were considered as ground truth. This is still the golden standard for clinical gait analyses [Lohnert 10]. It is well-known that the proper attachment of markers to bony landmarks is critical, and marker trajectories are subject to soft tissue artifacts during movements [Della Croce 06]. Marker placements should hence also be considered as estimation variables and resulting trajectories need to be checked against known anatomical constraints [Leardini 05, Andersen 09]. Recent approaches treat the kinematic parameter estimation as an overall optimization problem with respect to anatomical constraints of the underlying meta-model, marker placement, trajectory tracking and user-provided anthropometric measurements [Andersen 10].

#### Kinetic Scaling

Dynamic and muscular parameters are mostly scaled within a second, separated step using a particular scaling law, which prescribes the predictor variables and applied regression models. Often segment masses are simply scaled using a mass distribution, given in the meta-model [Winter 09]. Muscle strengths may then be implicitly estimated based on the height and mass of the subject. However, in this case a high body fat percentage would also increase the total segment mass, and the proportion of muscle tissue could be overestimated. It is therefore convenient to incorporate the fat percentage, such that muscle strength is rather determined by the remaining proportion of tissues [Rasmussen 05].

### 2.1.6 Muscles

Eventually, for a complete musculoskeletal analysis, a comprehensive muscular system model has to be integrated in the skeletal model. After the previous section shortly discussed methods of muscular parametrization, the modeling aspects will be addressed subsequently. Resolving the net joint forces and moments for their individual muscle forces during movements remains the most challenging part of musculoskeletal analysis because of the mechanical complexity of the muscular system, but also due to the activation mechanisms through the central nervous system, which are still poorly understood [Manal 04, Nigg 07]. Furthermore, depending on the application, passive structures of the musculoskeletal system, such as cartilage, menisci and ligaments, which actually contribute to the joint

stiffness might be mandatory to model in order to obtain quantitatively realistic results. From a rather functional point of view on muscle force contribution, these components are often conveniently omitted [Pandy 01]. A brief introduction on muscle modeling, following the latter perspective, will be given subsequently, albeit this broad subject still cannot be covered extensively within the scope of this thesis.

### Physiological Muscles

Skeletal muscles are activated by neural stimuli and exert force through contraction on skeletal bones. Two basic building blocks of muscles are the actin and myosin filaments, which build cross-bridge connections in consequence of chemical processes, initiated by neural innervation. These intertwined myofilaments, repeatedly aligned in series of sarcomeres, slide into one another and thus generate a contractile force along the muscle fiber. Numerous parallel muscle fibers together form a muscle belly, which is then connected to skeletal bones via tendons that ensure for both force transmission and elasticity. While actin and myosin cross-bridges constitute the actual force generating component, which is often referred to as the active or contractile element, tendons and connective tissue coating, the muscle fibers act as passive elements providing resiliency and renitency to the muscular system [Greger 88, Jovanović 15].

### Muscle Models

There are two major paradigms of muscle modeling whereof the first is a rather phenomenological approach, based on the pioneering work of Hill [Hill 38]. Hereupon, muscles are modeled as mechanical units known as the three-elements model, composed of an active contractile element and passive elastic parallel and series elements, where the latter two model viscoelastic properties of connective tissues within a muscle and the additional elasticity contribution of tendons, respectively. Models following this paradigm are believed to describe general muscle behavior moderately well, while also being computationally efficient. Huxley, in contrast, incorporated the mechanisms of cross-bridge building dynamics of the filaments, which led to a class of models, extending the classical model on a deeper, microscopic level at the price of higher complexity and numerical effort [Huxley 57].

### Hill Type Model

The Hill type model is composed of three mechanical abstraction components: the contractile element (CE), a parallel elastic element (PE) and a series elastic element (SE), whereof the former models the muscle's active contraction, the second independently accounts for the muscle's passive response, when being stretched, and the latter adds the tendon's and the muscle's intrinsic elasticities. The active and passive forces  $F_{CE}$ ,  $F_{PE}$ , associated with the respective components, sum up to the total muscle force  $F_M$ . The pennation angle  $\gamma$  describes the angle between the muscle's direction of action and the alignment of fibers, thus relating the tendon and muscle force:  $F_T = F_M \cos \gamma$ . The pennation angle is actually dependent on the extent of contraction; however, a constant angle  $\bar{\gamma}$  in the muscle's neutral position is often used instead. Typically, the muscle's active force  $F_{CE}$  is dependent on its level of activation  $a$ , its specific maximum isometric force  $F_0$  and two characteristic force-length and force-velocity functions  $f_{CE,l}(l_M)$ ,  $f_{CE,v}(v_M)$  describing the contraction dynamics by mapping the muscle's length and shortening

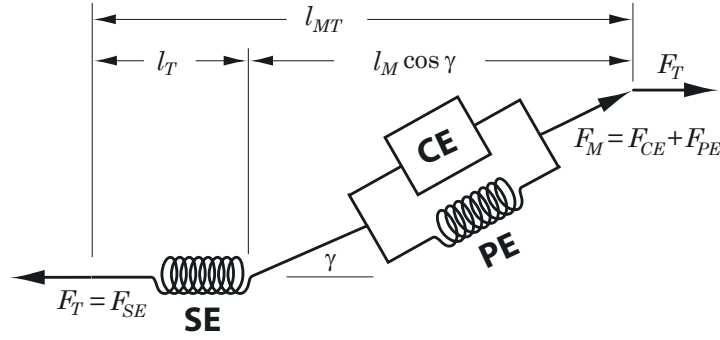


**Figure 2.5:** Hill type muscle model; adapted from [Arnold 10].

velocity to normalized forces:  $F_{CE} = a F_{M,0} f_{CE,l}(l_M) f_{CE,v}(v_M)$ . Two additional functions  $f_{PE,l}(l_M)$  and  $f_{SE,l}(l_T)$  describe the force-length relationships of passive and tendon force, depending on muscle and tendon lengths, respectively. Figure 2.5 shows the basic Hill type model and the forces acting on its components (cf. [Arnold 10]).

## 2.2 Motion Capture

With the formalisms and artifacts of musculoskeletal modeling, defined in the previous sections, the first process stage of the analysis pipeline will be discussed subsequently. Motion capture (MoCap) is a generic term of techniques for sensing, digitizing and recording motions of any objects in space-time, where in the scope of biomechanical applications the object of interest is mostly human, and the space of motion is 3-dimensional.

### 2.2.1 Approaches in Human Motion Capture

Several human motion capture methods exist, which might be classified according to the relation between sensors, emitters and their frame of reference into the categories outside-in, inside-out and inside-in tracking.

#### Exocentric Optical Tracking as Benchmark

Optical outside-in tracking is by far the most common approach in human motion capture, where a set of cameras is mounted in an environment and focused towards a subject. Usually, the subject is equipped with markers placed at bony landmarks, which are either actively emitting or passively reflecting light, sensed by the cameras. In this way the underlying skeleton can be estimated and tracked. Albeit there are marker-less vision-based alternatives, trying to fit skeletons in real-time [Theobalt 02], the marker-based approach providing very high tracking precision is the well-established golden standard, especially for clinical analyses [Lohnert 10].

#### Advantages of Egocentric Tracking

Egocentric inside-out systems with e.g. body-worn cameras, that orientate themselves by means of landmarks in an environmental reference frame, are rather uncommon for whole-body tracking and instead found in robotics and augmented reality scenarios [Miezal 12].



However, the idea of attaching sensors to the subject offers some advantages compared to the classical, stationary motion laboratory setup: the subject's range of motion is not limited by the sampling volume of the sensors and indeed independent of the environment. Moreover, no laborious, additional marker placement is necessary if the sensors' positioning relative to the skeleton is assumed to be known.

### Inertial Tracking as Promising Alternative

Recently, inside-in tracking methods using inertial sensors are emerging in the field of human motion capture and promise a high flexibility at lower costs, while progressively also fulfilling precision requirements of clinical applications [Young 10, Lohnert 10, Garofalo 10]. Compact, integrated smart sensors combine a triad of accelerometers, gyroscopes and magnetometers into miniature inertial measurement units, that measure change of position and orientation in a sensor-intrinsic frame. Sophisticated sensor fusion approaches exist, that try to compensate well-known inaccuracies inherent in inertial sensors, such as biases and drifts over time [Roetenberg 06, Woodman 07]. However, body-worn inertial tracking systems with high positioning precisions for biomechanical applications remain a challenging but very promising objective in human motion capture [Salehi 12, Salehi 13, Miezal 13].

## 2.2.2 Optical Marker-Based Motion Capture

Optical marker-based methods rely on a system of several cameras, spanning a volume of their angles of view, in which marker trajectories can be captured. In theory, a marker must be visible for at least two cameras at any time in order to determine its spacial position through triangulation. In practice of human motion capture, however, a much higher coverage is reasonable since markers are likely hidden for several cameras by the subject itself during motion. Furthermore, rigid body tracking requires in principle at least three marker points per segment in order to reconstruct its six DoFs. In skeleton tracking applications, the total number of markers can be reduced due to limiting joint constraints if markers are placed at appropriate anatomical landmarks. A certain amount of redundancy is, however, preferable. Markers close to one another might be confused during fast movements. A consistently high tracking precision of suchlike systems is only achieved if markers are always seen by several cameras. Systems of 12 or more cameras are common practice and require an appropriate calibration effort for each new trial, especially if the cameras are not stationary mounted in a laboratory environment.

Finally, for any further biomechanical processing, a precise attachment of markers at the anatomical landmarks, prescribed by the marker protocol, is mandatory. Moreover, marker positions might vary over time due to slippage during fast motion, but certainly, because of the movement of the skin and soft tissues relative to bony landmarks known as soft tissue artifacts [Leardini 05, Della Croce 06]. A post-processing of recorded data is often necessary due to small gaps or drifts in the marker trajectories, caused by any of the above mentioned issues. With all due elaborateness, optical marker-based systems achieve a sub-millimeter tracking precision and are thus still assumed to set the reference standard in human motion capture [OptiTrack Doc. 17]. An exemplary optical marker-based system is sketched in figure 2.6a and an extensive treatise of optical tracking methods in general and the theory behind can be found in [Dorfmueller-Ulhaas 02].

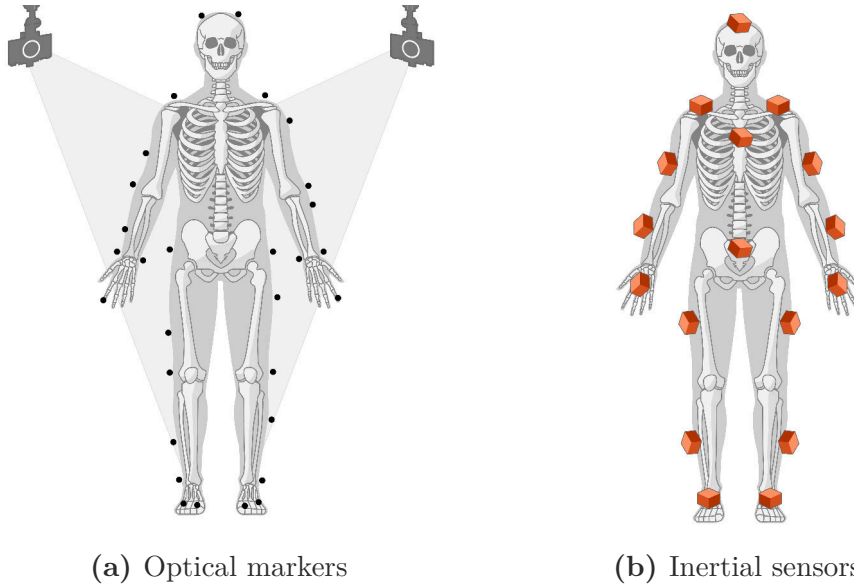


**Figure 2.6:** Optical marker-based versus inertial skeleton tracking equipment.

### 2.2.3 Inertial Motion Capture

After the classical human motion capture approach has been shortly described above, the emphasis will now be on inertial motion capture as an essential subject matter, within the scope of this thesis. Inertial motion tracking systems require an adequate amount of inertial sensors to be attached to the subject at each major body segment. A one-to-one sensor to segment mapping, with respect to the underlying skeleton model, is convenient since each sensor can in principle detect changes in all six DoFs. Even so, reliable, absolute inertial positioning requires advanced data processing and fusion methods since each inertial sensor provides technically only (distorted) information of the changes in orientation and position, i.e. angular velocities and accelerations. Tracking precision is hence less a result of only the sensors' accuracy, but also largely dependent on the algorithmic processing of measurements.

Although inertial tracking requires neither a calibrated camera system nor markers to be accurately attached, an essential source of error is the sensor-to-segment alignment. Inertial sensors might be placed at any location on the surface of body segments in principal. However, their relative placement with respect to the segment frame must be precisely known in order to recalculate the segmental location in space based on measurements obtained in the local sensor frames as illustrated in figure 2.6b. The determination of suchlike sensor-to-segment calibrations is considerably less intuitive than palpating marker landmarks. Some approaches towards self-calibration have been proposed, for instance, in [Taetz 16] and [Zimmermann 17] and are currently object of research. Within that scope usually the influences of suchlike calibration errors on kinematic trajectories are considered whereas their propagation through further stages of musculoskeletal analysis remain rather unclear.



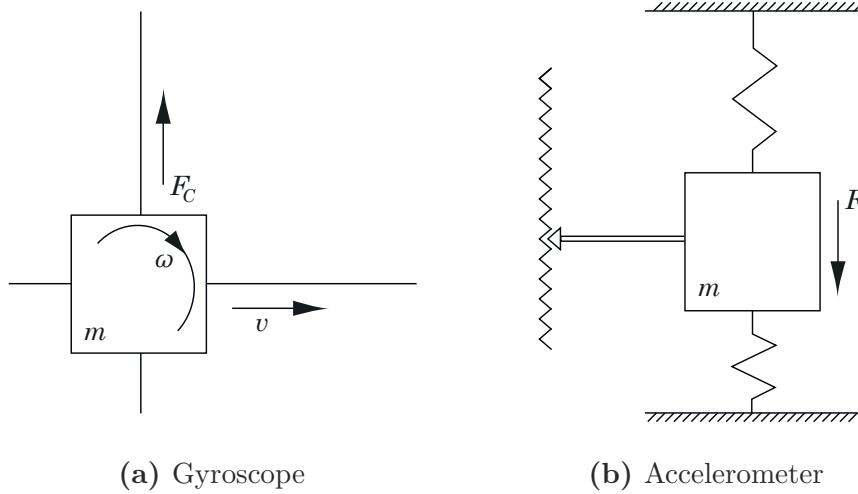


**Figure 2.7:** Working principles of gyroscopes and accelerometers; adapted from [Woodman 07].

### 2.2.4 Inertial Measurement Units

Inertial measurement units (IMUs) are composed of each three pairwise orthogonal gyroscopes, accelerometers and sometimes additional magnetometers (then also referred to as MIMUs), which measure angular velocity, linear acceleration and local magnetic field in a local sensor frame, respectively. This information is integrated in a complementary way, thereby, ideally minimizing the uncertainties inherent in each basic sensor type, such that an overall (change of) position and orientation is known in a global reference frame. Compact versions, that can be mounted rigidly on moving bodies (inertial strapdown systems), are implemented in micro-electro-mechanical systems (MEMS) as a tradeoff between precision, size and cost. Below, working principles and error characteristics of the basic MEMS sensor types as well as complementary error compensation methods are described. The terms inertial sensor and (M)IMU will be used interchangeably and referred to the entire integrated sensor unit instead of the basic sensors.

#### Gyroscopes

MEMS gyroscopes are mostly realized as vibrating mass gyroscopes and take advantage of the Coriolis effect. Accordingly, a mass  $m$  moving with velocity  $v$  within a reference frame, that rotates at an angular velocity  $\omega$ , is exposed to the Coriolis force  $F_C = 2m(\omega \times v)$ . Figure 2.7a sketches the working principle of a vibrating mass gyroscope. Technically, a small mass (resonator) is vibrated along a drive axis using e.g. a piezoelectric actuator. As the sensor is rotated, a secondary vibration along the sense axis orthogonal to the drive axis is induced due to the Coriolis force, which can be measured and used to deduce the angular velocity [Woodman 07].

The sensor's angular change can then be formulated using quaternion differentiation [Dantam 14]. With  $q_{R,t}^{GI}$ , an initially known relative rotation between the IMU frame  $I$ , and the global frame  $G$  at time  $t$  and the angular velocity  $\omega_t$ , expressed as a quaternion, the angular change is (c.f [Roetenberg 09]):

$$\dot{q}_{R,t}^{GI} = \frac{1}{2} q_{R,t}^{GI} \odot (0, \omega_{t,x}, \omega_{t,y}, \omega_{t,z}) \quad (2.7)$$

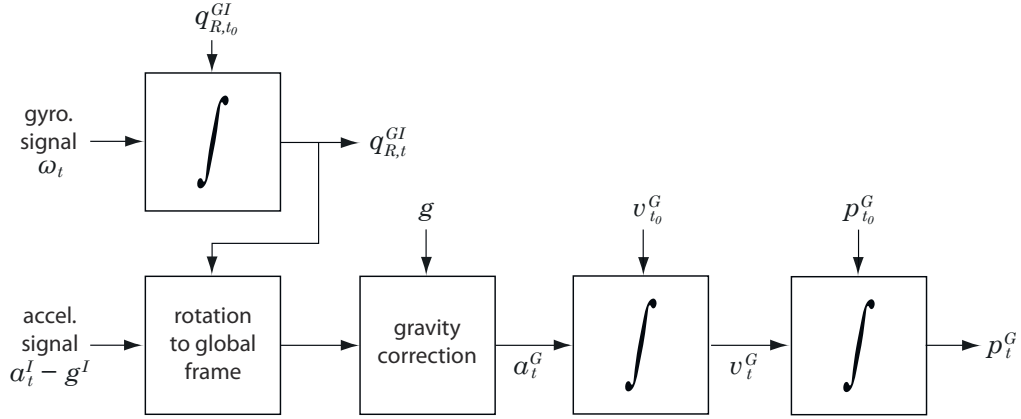


**Figure 2.8:** Inertial strapdown integration; adapted from [Woodman 07].

### Accelerometers

Mechanical accelerometers rely on a proof mass suspended on (micro) springs that is subject to the force of inertia  $F = m a$ . At the same time, the force is also proportional to the deflection of the mass-spring system, according to Hooke's law:  $F = k d$ . Thus, with  $a = \frac{k d}{m}$ , the acceleration can be determined through this momentary displacement as illustrated in figure 2.7b. MEMS versions are often implemented as capacitive accelerometers, where the mass is part of a (differential) capacitor, whose capacity  $C = \epsilon \frac{A}{d}$  is dependent on either the effective enclosed area  $A$  or the displacement  $d$  of the plates. The change in capacity can be then measured and the acceleration deduced. Various different methods of measurement are possible, which are briefly summarized in [Woodman 07].

Note that the accelerations measured this way include the gravitational component  $g$ . With the global sensor orientation  $q_{R,t}^{GI}$  known from the gyroscope, the acceleration measured in the sensor frame  $I$  can be rotated to the global frame  $G$  (c.f [Roetenberg 09]):

$$a_t^G - g^G = q_{R,t}^{GI} \odot (a_t^I - g^I) \odot (q_{R,t}^{GI})^* \quad (2.8)$$

After removing the gravitational component, double integration yields the sensor's position  $p$  in the global frame:

$$\ddot{p}_t^G = a_t^G \quad (2.9)$$

The process of incrementally determining global orientations and positions from combining gyroscope and accelerometer data is known as inertial strapdown integration and depicted in figure 2.8.

### Error Characteristics

The precision of MEMS sensors is subject to various sources of errors due to e.g. manufacturing inaccuracies, calibration errors, temperature effects, thermo-mechanical and electronic noises. As the output signals of both gyroscopes and accelerometers must be (successively) integrated, the influences of suchlike errors increase over time and lead to significant deviations in positioning.

The average output of a sensor, when not being subject to any translational or rotational displacement, is called constant bias  $\epsilon$ . It grows either linearly with time or quadratically

according to  $\epsilon \frac{t^2}{2}$  due to single or double integration, respectively.  $\epsilon$  can be recorded and averaged over a reasonably long time and compensated by a subtraction from the sensor's operating output. Thermo-mechanical noises with frequencies considerably higher than the sensor sampling rate add a white noise to the sensor outputs and are assumed to be zero-mean random walks, where the standard deviation increases over time. Likewise, flicker noises in the electronics, causing the sensor's bias to fluctuate, are usually modeled as random walks. Additionally, under changing environmental conditions or due to self heating during the operating time, temperature changes induce nonlinear bias changes. Some systems, however, are equipped with internal temperature sensors and are able to compensate for such influences. Finally, a class of internal calibration errors referring to scale factors, alignments and output linearities manifest themselves only under operating conditions, but can be measured in principal and are mostly compensated similarly to constant biases. Detailed error models and effects specific to gyroscopes and accelerometers have been investigated in [Woodman 07].

### 2.2.5 Sensor Fusion

As each sensor is subject to inherent types of errors, measurements will be likewise distorted according to respective error characteristics. If several, noisy measurements contribute (redundantly) to an overall system state, sensor fusion aims to factor in the different sources of information in such a way, that individual distortions are mutually compensated. Knowledge about erroneous sensor signal characteristics and the system itself in form of quantitative process models, enable sensor fusion algorithms to come up with an (approximately) optimal estimate of the system's state in existence of particular measurement errors. Widespread techniques in this context are recursive filters, such as variants of particle and Kalman filters [Rigatos 10].

#### Complementary Inertial Fusion

In an inevitable presence of remaining bias errors along with noises, the gyroscope output integration leads to substantial drifts over time, that would moreover propagate through the entire strapdown integration if not compensated (cf. figure 2.8). Accelerometers, inherently providing a drift free acceleration measurement if bias-compensated, contain an inclination information. Assuming that linear accelerations in the horizontal plane are reasonably small compared to gravitation, the predominant gravitational component can be detected and used to estimate the vertical axis. This information in turn allows for readjustment of drifted gyroscopes, thus providing stability of the horizontal plane over time. However, this is no remedy for heading drifts around the vertical axis and hence often magnetometers complement the basic sensor types, albeit they are not necessary for positioning in principle [Roetenberg 06, Woodman 07].

#### Fusion with Magnetometers

Magnetometers measure the strength and direction of the local magnetic field, supposed to coincide with the earth's magnetic field. In this case, the direction of the magnetic north can be determined and the gyroscopes' heading drift corrected. Taken together, both techniques provide stability with respect to a global (earth) reference frame and are well-known as attitude and heading reference system (AHRS). The latter assumption is, however,

rarely valid in practice due to magnetic disturbances, which are omnipresent particularly in indoor scenarios. Ferromagnetic materials or electromagnetic interference disturb the local magnetic field and cause notable estimation errors of the heading direction in the vicinity of the magnetometer. Although being prone to errors themselves, magnetometers provide an additional, independent source of information and are conceptually well-suited to compensate for weaknesses of the two basic inertial sensors. After modeling the error characteristics, the weighting of measurements should then be left to the sensor fusion algorithm [Roetenberg 06].

## Kalman Filter

The Kalman filter (KF) is an established choice for sensor fusion as it enables a considerably efficient online processing, inherently uses a state-space formulation and provides an optimal state estimation in case of both linear measurement and system models that are subject to Gaussian noise. The latter is a limitation in practice; however, variants, such as the extended Kalman filter (EKF), allow for any differentiable state transition and measurement models by applying linearizations about the operating points. Although their estimation in this case is a suboptimal approximation, EKFs are often considered to constitute the golden standard in inertial positioning systems [Wan 06].

Since a comprehensive explanation of the Kalman Filter is beyond the scope of this thesis, the kind reader may be referred to the concise introduction of [Welch 95] for probabilistic backgrounds. Subsequently, the linear Kalman filter equations are introduced and briefly annotated, following the notation in [Elmenreich 02], and later extended to the EKF [Bleser 12].

A general discrete linear Gaussian state-space model is denoted:

$$x_{t+T} = F x_t + B u_t + e_t^{\hat{X}} \quad (2.10)$$

$$y_{t+T} = H x_t + e_t^X, \quad (2.11)$$

where  $x_t$  is the internal state vector (true system state) at time  $t$ ,  $T$  the sampling time,  $F$  the system matrix,  $B$  the control matrix, relating the control input vector  $u_t$  to the system state,  $H$  the measurement (observation) matrix relating the measurement vector  $y_t$  to the system state and  $e_t^{\hat{X}} \sim \mathcal{N}(0, \Sigma^{\hat{X}})$ ,  $e_t^X \sim \mathcal{N}(0, \Sigma^X)$  are process and measurement noises drawn from a zero mean multivariate normal distribution with covariance matrices  $\Sigma^{\hat{X}}$ ,  $\Sigma^X$ , respectively. In this context,  $F$  and  $H$  are also referred to as the state transition model and the measurement (observation) model, according to their described mappings. Note, that  $F$  equal to the identity matrix and  $B$  equal to the zero matrix describe a standard sensor fusion case, where the system state is solely comprised of successive, noisy measurements.

In a first phase, known as predict or time update, the Kalman filter projects the current system state and error covariance estimates forward in time, in order to obtain a priori (predicted) estimates of the state  $\hat{x}_{t+T|t}$  and the error covariance  $P_{t+T|t}$  of the successive time step:

$$\hat{x}_{t+T|t} = F x_{t|t} + B u_t \quad (2.12)$$

$$P_{t+T|t} = F P_{t+T|t} F^T + \Sigma^{\hat{X}} \quad (2.13)$$

In a second correction or measurement update phase, the current a priori estimate is adjusted by current measurements, resulting in an a posteriori (refined) estimate, incorporating the measurements as feedback. The a posteriori state estimate  $\hat{x}_{t+T|t+T}$  might be seen as the best possible guesses at time  $t + T$ , given all the measurements up to and including the current time step  $t + T$  and the a posteriori error covariance  $P_{t+T|t+T}$  as a measure of the estimated precision of the current state estimate.  $\hat{x}_{t+T|t+T}$  and  $P_{t+T|t+T}$  constitute the filter state. In order to formulate the update equations, define the measurement or innovation residual  $\tilde{y}_{t+T}$  as the difference of the predicted and actual measurement and, moreover, an innovation or residual covariance  $S_{t+T}$ :

$$\tilde{y}_{t+T} = y_{t+T} - H_{t+T} \hat{x}_{t+T|t} \quad (2.14)$$

$$S_{t+T} = H_{t+T} P_{t+T|t} H_{t+T}^T + \Sigma^X \quad (2.15)$$

The optimal Kalman gain matrix  $K_{t+T}$  is computed, such that it minimizes the a posteriori error covariance, thus being a multivariate weight factor that determines the respective ratios as to the filter relies on state measurements versus state predictions:

$$K_{t+T} = P_{t+T|t} H_{t+T}^T S_{t+T}^{-1} \quad (2.16)$$

The filter state, i.e. the a posteriori system state and error covariance, is then updated as follows:

$$\hat{x}_{t+T|t+T} = \hat{x}_{t+T|t} + K_{t+T} \tilde{y}_{t+T} \quad (2.17)$$

$$P_{t+T|t+T} = (I - K_{t+T} H_{t+T}) P_{t+T|t} , \quad (2.18)$$

where  $I$  is the identity matrix.

Both prediction and update phases usually progress alternatingly as long as measurements arrive. The filter may, however, run (temporarily) in an open-loop mode, predicting without newly acquired measurements, which then certainly causes the error covariance to grow.

### Extended Kalman Filter

The extended Kalman filter relaxes the restrictions of the linear version in such a way that the state transition and measurement models may be differentiable functions of the state and the control vector:

$$x_{t+T} = f(x_t, u_t) + e_t^{\hat{x}} \quad (2.19)$$

$$y_{t+T} = h(x_t) + e_t^X , \quad (2.20)$$

where  $f$  and  $h$  describe the predicted state, dependent on the previous state, and the predicted measurement, dependent on the predicted state, respectively. The equations of the linear Kalman version including  $\hat{x}$  and  $u$  change analogously.

In order to apply these functions to the covariance matrix, the state transition and measurement matrices are chosen as their Jacobian matrices, linearizing the models

through a first order Taylor expansion at the operating points of the previously predicted state, the previous control input and the currently predicted state, respectively:

$$F_t = \left. \frac{\partial f}{\partial x} \right|_{\hat{x}_t|t, u_t} \quad (2.21)$$

$$H_{t+T} = \left. \frac{\partial h}{\partial x} \right|_{\hat{x}_{t+T}|t} \quad (2.22)$$

Note, that the estimations of the EKF might be notably affected by these linearization errors as the underlying filter used is still the linear KF, expecting linear Gaussian models. With that said, it is now possible to define a sensor fusion algorithm in the narrower sense, i.e. a Kalman fusion of the basic sensor types of each inertial sensor. The EKF allows to incorporate non-linear measurement models as is, for instance, the case with a magnetometer model for heading correction relying on the atan2 function of the magnetometer measurements in the horizontal plane.

### Multi Sensor Fusion

If several sensors are available that are in a known relative spatial relation to one another, as is the case with skeletal tracking, where IMUs are attached to skeletal bones, all their information may be combined. Utilizing these implicit anatomical constraints might allow to further reduce the measurement uncertainties of individual IMUs. A very general concept of incorporating biomechanical constraints within a multi sensor fusion method has been presented in [Roetenberg 09]. The proposed approach relies on a cascaded implementation, where an inner filter fuses accelerometer, gyroscope and magnetometer measurements IMU-wise in a classical, inertial sensor fusion manner. Within an outer cascade, IMU and body segment positions and orientations are predicted based on a kinematic body model and corrected using joint constraints, external contacts, such as foot ground contacts, and any optional external measurements. While being versatile and flexible, this decoupled approach poses a challenge in back-propagating the error covariances of the kinematic estimates to the inner cascade in order to influence the inertial sensor fusion. A coupled approach, that integrates both sensor measurement and biomechanical constraint models into a single EKF, has been evaluated in [Miezial 16]. The conceptualized IMU-driven musculoskeletal analysis pipeline and the experiments conducted within the scope of this thesis make an extensive use of the latter method. Capable of solving the inverse kinematics for inertial motion capture trajectories with respect to skeletal constraints. This approach will be discussed in more detail in the subsequent kinematics section.

## 2.3 Inverse Kinematics

Within the biomechanical scope, inverse kinematics takes motion trajectories captured via any suitable motion capture method as an input and computes kinematic trajectories subject to an anatomically constrained skeleton model. Note, that motion capture and kinematic processing are technically closely related and often jointly handled in practice (cf. section 2.2.5). An optimal kinematic solution might involve adapting uncertain parameters associated with the capturing process, such as marker positions. Sometimes

this also implies to alter the skeleton model itself, i.e. its anthropometric parametrization or anatomical joint constraints during the model scaling process.

The kinematic results may be of any representation suitable to represent each segment's orientation and position in space-time. Usually these are either technical or anatomical joint angles or complete 6-DoF free segment trajectories. While the former is traditionally the representation of choice for further biomechanical investigations, a process fed with inertial motion capture data might preferably operate on free segment kinematics in real coordinate space since segment-attached IMUs provide appropriate information, and sensor fusion algorithms should exploit this inherent over-determinacy.

In the following, firstly the perspective from a classical marker-based approach is outlined for comparison. Afterwards, the previously mentioned multi sensor fusion method for inertial skeleton tracking will be discussed in more detail.

### 2.3.1 Marker-Driven Kinematics

As one relies solely on a predefined marker protocol to define the skeleton model, a kinematic chain model is obtained from anthropometric measurements and the marker trajectories jointly determining the subject-specific joint centers, joint-to-joint distances and axes. The kinematic analysis simplifies in that case to a computation of Euler angles between the segments measured in anatomical frames. The segments' locations in space are directly determined through the associated marker positions in each time step. This approach, also referred to as direct kinematics, assumes marker trajectories to be ground truth and is thus fully subject to marker placement errors and soft tissue artifacts. However, it is still a widespread technique used in clinical gait analysis [Lohnert 10]. The Vicon system, using the Plug-in Gait (PiG) marker protocol, is a well-established representative of this paradigm [Kadaba 89, Davis 91].

#### Static Motion Optimization

The assumptions of direct kinematics are questionable from an analytical perspective and hence discarded in most musculoskeletal analysis frameworks. Instead, inverse kinematics is often formulated as an optimization problem, minimizing the differences between the measured, expected marker trajectories  $r_m^{exp}(t)$  and target trajectory functions that are dependent on the model's generalized coordinates  $r(q(t))$ . In this way, the anatomical restrictions are considered as soft constraints, allowing for deviations from the both expected trajectories and anatomical constraints in favor of a minimal weighted least-square error summed up over all marker trajectories  $m \in M$  per time step [OpenSim Doc. 17]. The respective optimal generalized coordinates at time  $t$  are thus:

$$\hat{q}(t) = \arg \min_{q(t)} \left[ \sum_{m \in M} w_m \|r_m^{exp}(t) - r_m(q(t))\|^2 \right] \quad (2.23)$$

#### Full Motion and Parameter Optimization

More generally, the inverse kinematics problem of any holonomic system may be formulated via its constraint matrix  $\Gamma$ :

$$\Gamma(q(t)) = 0, \quad (2.24)$$



where  $\Gamma$  incorporates all motion constraints, prescribed through the expected marker trajectories as well as the anatomical model constraints. Both constraint formulations are moreover dependent on the underlying kinematic model, i.e. joint-to-joint distances and joint axes, for instance. All suchlike parameters may be explicitly included into these constraint equations via a parameter set  $P$ .  $\Gamma$  can be farther split into the respective constraint sets:

$$\Gamma(q(t)) = \begin{bmatrix} \Psi(q(t), P) \\ \Phi(q(t), P) \end{bmatrix}, \quad (2.25)$$

with  $\Psi$  the motion constraints and  $\Phi$  the anatomical constraints, dependent on the generalized coordinates and the kinematic model parameters.

They may now be treated separately such that the motion constraints are considered as soft constraints, while the anatomical constraints need to be strictly fulfilled. In this way, a possible kinematic over-determinacy can be handled while still ensuring the anatomical correctness of the solution. With any suitable motion objective function  $H(\Psi)$ , e.g. a weighted least-square formulation as shown above, again a motion optimization problem for each instance of time  $t$  is formulated:

$$\begin{aligned} \hat{q}(t) &= \arg \min_{q(t)} [H(\Psi(q(t), P))] \\ \text{s.t. } &\Phi(q(t), P) = 0 \end{aligned} \quad (2.26)$$

Within an overall optimization routine, the optimal kinematic model parameters  $\hat{P}$  are determined such that the sum of the motion objective function  $H$  evaluated at a fixed parameter set for all time steps  $t \in T$  is minimized, while the kinematic constraints, instantiated with the respective parameters, are always strictly fulfilled. With an additional set of constraints  $\Pi(P)$  imposed on the model parameters, e.g. limits of segment lengths, the complete parameter and motion optimization is denoted:

$$\begin{aligned} (\{\hat{q}(t)|t \in T\}, \hat{P}) &= \arg \min_{\{q(t)|t \in T\}, P} \left[ \sum_{t \in T} H(\Psi(q(t), P)) \right] \\ \text{s.t. } &\Phi(q(t), P) = 0 \quad \forall t \in T, \\ &\Pi(P) = 0 \end{aligned} \quad (2.27)$$

This formulation allows the implementation of an overall optimization routine of motion trajectories as well as of the kinematic model itself, while taking anthropometric measurements into account, thus combining the domains of motion capture, inverse kinematics and model scaling. The approach is discussed in greater detail in [Andersen 10] and conceptually motivated in [Skals 16].

### 2.3.2 IMU-Driven Kinematics: Quattracker

The IMU-driven approach presented in [Miezial 16] is based on an EKF, where in particular kinematic model constraints are incorporated via virtual measurements. Also an additional IMU-driven method, applying a weighted least-squares optimization, has proposed there, which has been evaluated with a better estimation performance in terms of kinematic errors. However, the optimization approach is also computationally more expensive. Henceforth, only the EKF implementation will be considered and is referred to as quattracker. The notation will closely follow the mentioned paper. To start with, the basic sensor measurement models are defined below.



### Sensor Measurement Models

Let  $I_i \in \mathbb{I}$  denote an IMU and  $y_{i,t}^\omega, y_{i,t}^a, y_{i,t}^m$  the associated gyroscope, accelerometer and magnetometer data at time  $t$ . The gyroscope measurement model with the angular velocity  $\dot{q}_{R,t}^{GI_i}$  and noise  $e_{i,t}^\omega$ , and is then in accordance with equation 2.7:

$$y_{i,t}^\omega = \dot{q}_{R,t}^{GI_i} + e_{i,t}^\omega \quad (2.28)$$

Note, that  $\dot{q}_{R,t}^{GI_i}$  is a quaternion, whose scalar part is zero and is thus compatible with  $e_{i,t}^\omega$ . Likewise, the acceleration model is denoted analogously to equation 2.8:

$$y_{i,t}^a = (q_{R,t}^{GI_i})^* \odot (\ddot{I}_i^G - g^G) \odot q_{R,t}^{GI_i} + e_{i,t}^a \quad (2.29)$$

At this place, the gyroscope and accelerometer bias models are omitted, but can be easily included; cf. [Bleser 09, Kok 14].

The magnetometer model is chosen to only contribute to the heading correction, omitting the inclination angle information as a method to reduce influences of magnetic disturbances [Ligorio 16]. The model considers the angular deviation from the global x-axis using the normalized magnetometer measurement  $\bar{y}_{i,t}^m$ , which is transformed in the global frame and projected onto the horizontal plane:

$$\text{atan2} \left[ \frac{q_{R,t}^{GI_i} \odot [\bar{y}_{i,t}^m]_y \odot (q_{R,t}^{GI_i})^*}{q_{R,t}^{GI_i} \odot [\bar{y}_{i,t}^m]_x \odot (q_{R,t}^{GI_i})^*} \right] = 0 \quad (2.30)$$

### Anatomical Constraint Models

Anatomical restrictions, which are first and foremost the displacement constraints, ensuring that the model's segments stay connected, are incorporated as virtual measurements into the EKF. For each pair of joint endpoints  $P^{J_{i,j}} = p_m^{S_i}, p_n^{S_j}$  the following segment connection constraint must hold:

$$S_{i,t}^G + R_t^{GS_i} p_m^{S_i} - (R_t^{GS_j} p_n^{S_j}) + e_t^{P^{J_{i,j}}} = 0 \quad (2.31)$$

Note, that the expression with the second joint endpoint might also be exchanged by any point  $p^G$  in global space, thus ensuring that endpoint  $p_m^{S_i}$  stays always close to  $p^G$  and fixes the segment's global position (e.g. the root segment position).

Furthermore, in order to find an anatomically correct kinematic solution, joints constraints expressed in real coordinate space can now be easily added in the same manner.

### State Space

As the Quattracker uses a constant angular velocity and a constant acceleration model (cf. [Bleser 09]), the angular velocity and the linear acceleration are required in the state space. Assuming a known, time-invariant sensor-to-segment calibration, a segment pose can be reconstructed by means of the respective IMU positions and orientations. The following state vector describes the system sufficiently:

$$x_t = \left( \{I_{i,t}^G, \dot{I}_{i,t}^G, \ddot{I}_{i,t}^G, q_{R,t}^{GI_i}, \dot{q}_{R,t}^{GI_i} \mid I_i \in \mathbb{I}\} \right)^T \quad (2.32)$$

### State Transition Model

The state transition or dynamic model of the system is denoted:

$$x_{t+T} = \begin{bmatrix} I_{i,t+T}^G \\ \dot{I}_{i,t+T}^G \\ \ddot{I}_{i,t+T}^G \\ q_{R,t+T}^{GI_i} \\ \dot{q}_{R,t+T}^{GI_i} \\ \vdots \end{bmatrix} = \begin{bmatrix} I_{i,t}^G + T \dot{I}_{i,t}^G + \frac{T^2}{2} \ddot{I}_{i,t}^G \\ \dot{I}_{i,t}^G + T \ddot{I}_{i,t}^G \\ \ddot{I}_{i,t}^G + T e_t^{\hat{P}_{i,j}^{j,j}} \\ q_{R,t}^{GI_i} \odot \exp\left(\frac{T}{2} \dot{q}_{R,t}^{GI_i}\right) \\ \dot{q}_{R,t}^{GI_i} + T e_{i,t}^{\hat{\omega}} \\ \vdots \end{bmatrix}, \quad (2.33)$$

where  $\exp$  is the quaternion exponential function with the angular velocity quaternion  $\dot{q}_{R,t}^{GI_i}$  with a zero scalar part as the argument. For a detailed explanation, why the expression can be used as a consistent approximation for the discrete-time model  $q_{R,t+T}^{GI_i}$ , please refer to [Miežal 16] (appendix B).

### Quattracker Execution

With the initial set of measurements and the TRIAD algorithm described in [Black 64], the initial IMU orientations  $q_{R,0}^{GI_i}$  are determined. In a second step, the validity of the anatomical constraints is ensured, and the initial angular and linear velocities and accelerations are set to zero. As the quattracker operates with all variables of the state space, denoted in the IMU frames, an EKF pass over all time steps directly yields the estimated IMU orientation and position trajectories, which can then be easily applied to their mapped segments, using the known sensor-to-segment calibration. The resulting free segment kinematic trajectories are a proper inverse kinematics solution with respect to the fused IMU measurements and the underlying skeleton model.

## 2.4 Inverse Dynamics

With a known inverse kinematics solution, solved using any technique discussed in the previous section, the inverse dynamics problem is now technically independent of the specific motion capture approach, and the equations of motions of the dynamically parametrized body model can be formulated as follows.

### 2.4.1 Equations of Motion

For each segment  $S_i \in \mathbb{S}$  the Newton-Euler equations are denoted in respect of a frame centered at the segment's CoM:

$$\begin{bmatrix} m_i I_3 & 0 \\ 0 & \Theta_i \end{bmatrix} \begin{bmatrix} \dot{v}_i \\ \dot{\omega}_i \end{bmatrix} + \begin{bmatrix} 0 \\ \omega_i \times \Theta_i \omega_i \end{bmatrix} = \begin{bmatrix} f_i \\ \tau_i \end{bmatrix}, \quad (2.34)$$

with  $m_i$  the segment mass,  $I_3$  the identity matrix,  $\Theta_i$  the segment's inertia tensor,  $v_i$  and  $\omega_i$  the linear and angular velocity, respectively, and  $\dot{\omega}_i$  the derivative of the latter and the appropriate force  $f_i$  and moment  $\tau_i$ . A suchlike dynamic system can be solved through e.g. the iterative Newton-Euler algorithm.

However, a change of the configuration space towards the minimal representation with generalized coordinates might be advantageous for kinetic formalizations as it leads to an efficiently manageable set of Lagrangian equations of the second kind for each DoF.

## Lagrangian Dynamics

The relation between the Newton-Euler equations in real coordinate space and the Lagrangian perspective in generalized coordinate space will be briefly outlined following the notations in [Liu 12]. Let  $T_i$  be the kinetic energy of segment  $S_i$  and  $r_i = r_i(q_j(t))$  a particle, representing the segment's CoM in global space and dependent on a subset of generalized coordinates  $q_j$ , i.e. the DoFs of joints incident to the segment. The constraint according to the Lagrange formulation is then:

$$\frac{d}{dt} \left( \frac{\partial T_i}{\partial \dot{q}_j} \right) - \frac{\partial T_i}{\partial q_j} = \tau_{q_j} , \quad (2.35)$$

where  $\tau_{q_j}$  is the generalized force according to the principle of virtual work done by a force  $f_i$  exerting on  $r_i$ :

$$\delta W = f_i \delta r_i = f_i \sum_j \frac{\partial r_i}{\partial q_j} \delta q_j = \sum_j \tau_{q_j} \delta q_j , \quad (2.36)$$

with  $\tau_{q_j} = \left( \frac{\partial r_i}{\partial q_j} \right)^T$ .

Furthermore,  $v_i$  and  $\omega_i$  are transformed to the generalized coordinate space via their Jacobians:

$$J_i \dot{q}_j = \begin{bmatrix} J_{v_i} \\ J_{\omega_i} \end{bmatrix} \dot{q}_j = \begin{bmatrix} v_i \\ \omega_i \end{bmatrix} \quad (2.37)$$

The linear and angular velocity in the Newton-Euler equation can now be substituted, which yields:

$$\underbrace{\begin{bmatrix} m_i I_3 & 0 \\ 0 & \Theta_i \end{bmatrix}}_{=: M^{(S_i)}} J_i \ddot{q}_j + \begin{bmatrix} m_i I_3 & 0 \\ 0 & \Theta_i \end{bmatrix} J_i \dot{q}_j + \underbrace{\begin{bmatrix} 0 & 0 \\ 0 & J_{\omega_i} \dot{q}_j \end{bmatrix}}_{=: [\omega_i]} \begin{bmatrix} m_i I_3 & 0 \\ 0 & \Theta_i \end{bmatrix} J_i \dot{q}_j = \begin{bmatrix} f_i \\ \tau_i \end{bmatrix} \quad (2.38)$$

In order to convert the forces and moments in real coordinate space to generalized forces, the above equation is left-multiplied by the transposed Jacobian  $J_i^T$ :

$$\underbrace{(J_i^T M^{(S_i)} J_i)}_{=: M_i(q_j)} \ddot{q}_j + \underbrace{(J_i^T M^{(S_i)} \dot{J}_i + J_i^T [\omega_i] M^{(S_i)} J_i)}_{=: C_i(q_j, \dot{q}_j)} \dot{q}_j = \underbrace{J_i^T \begin{bmatrix} f_i \\ \tau_i \end{bmatrix}}_{=: \tau_{q_j}} \quad (2.39)$$

Finally, the entire system dynamics can be formulated likewise using the overall mass matrix  $M(q)$  and the Coriolis term  $C(q, \dot{q})$ :

$$M(q) \ddot{q} + C(q, \dot{q}) = \tau_q , \quad (2.40)$$

which is the matrix vector form of the set of all Lagrangian equations for each generalized coordinate, and can be easily solved. Note, that  $\tau_q$  is comprised of inertial, muscle and any externally applied forces. For a detailed introduction to Lagrangian mechanics and the concepts of virtual work and generalized forces, please refer to [Williams 96].

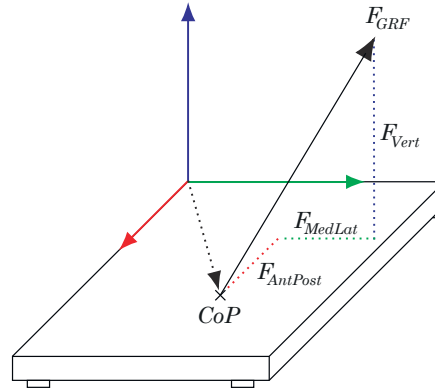


**Figure 2.9:** Force plate and decomposed ground reaction force vector.

### 2.4.2 Ground Reaction Forces

The goal of inverse dynamics as a part of the musculoskeletal analysis process is the determination of joint reaction forces and moments, which might then be further resolved to actual muscle forces. The right hand side of equation 2.40, however, is a superposition of all the external and internal forces acting on the total body. In order to divide them, the externally applied forces should be known and are conventionally measured along with motion trajectories during motion capture. In most biomechanical application scenarios and gait analysis in particular, the model without any additional loads is assumed to be only subject to ground reaction forces (GRFs).

#### Force plates

Ground reaction forces are measured with the help of force plates, which are analog devices composed of several force transducers that output signals proportional to the applied forces as a consequence of the mechanical deflection, leading to a change in electrical conductivity. A force plate provides a three-dimensional ground reaction force vector and the location of the center of pressure in a local coordinate system. From a biomechanical point of view, the GRF is often decomposed into its components in respect to the subject's direction of movement. These are the vertical force perpendicular to the ground plane and two shear forces, i.e. an antero-posterior force in the direction of movement and a medio-lateral component as shown in figure 2.9. Sometimes also the ground reaction moments subject to the force plate reference frame are provided. In order to incorporate these measured forces into the body dynamics, they must be transformed into a consistent global frame [Winter 09].

#### Drawbacks of GRF Measurements

Possibly several force plates are required in order to cover the ground plane area, where ground contacts of the subject are expected for a certain movement. Ideally, force plates are flush-mounted into the ground so as to not interfere with the subject's motion. Those are rather restrictive requirements, that are usually only fulfilled in dedicated gait laboratory environments and a major hindrance for a simple and flexible motion capture process even if a IMU-driven approach is used. Furthermore, force plates require a careful calibration process and must be time-synchronized with the motion capture devices.

Force plate measurements are subject to considerable errors, arising from e.g. a too low detection sensitivity for small forces, non-linearities, crosstalk and environmental variations. Even under adequate calibration and working conditions, force measurements are known to be affected by relative maximum errors of several percentage points. Likewise, the determination of the CoP is associated with an uncertainty area of a few square centimeters that typically increases at the peripheral plate area [Bartlett 07, Bobbert 90].

Finally, incorporating measured external forces into the equations of motions generally implies a dynamic over-determinacy at the foot segments of the model. This might lead to an inconsistency if the real force measurements do not exactly match the interaction of segment accelerations, obtained from captured kinematic trajectories and the modeled body masses and inertia. Commonly, this violation of the equations of motion is handled by introducing compensatory residual forces and moments at the model's root segment. A large magnitude of suchlike residuals, however, indicates the incorrectness of a dynamic solution. Several residual elimination or residual reduction methods exist that aim to minimize this inconsistency by adapting the dynamical body segment parameters and/or the kinematic trajectories [Kuo 95, Thelen 06, Delp 07]. These kinematic adjustments can lead to deviations of several degrees from the measured angular trajectories and might be considered questionable [OpenSim Doc. 17, Fluit 14].

## 2.5 Static Optimization

The ambitious goal of the static optimization process step is to finally distribute the internal net joint reactions, found through inverse dynamics, to individual muscle contributions for each time step of a motion sequence. As the musculoskeletal system is comprised of many more muscles than would be minimally required in order to actuate each skeletal DoF, for each posture, there are any number of possible muscle activation patterns that can lead to static equilibrium. From a mechanical point of view, the musculoskeletal system is highly redundant or indeterminate, which requires an additional set of constraint equations in order to obtain one specific of all conceivable solutions. Subsequently, this muscular redundancy problem and reasonable criteria for constraining the solution space are discussed.

### 2.5.1 Muscular Redundancy Problem

Technically, only one agonistic and another antagonistic contracting muscle per skeletal DoF would be required in order to actuate the musculoskeletal system. Even in this most simple case, their force contribution would be actually ambiguous due to the principle of co-contraction, which provides stability through an increased tension from the simultaneous activation of antagonistic muscles. This is especially useful for fine-motor tasks or during high dynamic loading situations. However, with actually many more muscles per joint or the same muscles spanning several joints, the muscular redundancy is vastly greater.

Naturally, the muscle recruitment is performed by the central nervous system, which is assumed to decompose a certain targeted motion into basic motion patterns, associated with the allocation of a particular set of muscles. Albeit the detailed mechanisms of muscle recruitment, especially on the deeper neurological level, are not yet fully understood, it is reasonable to postulate an invariant, underlying principle of optimality. It is assumed that

muscles are allocated in an energy efficient and stress minimizing manner, thus reducing the overall necessary muscle forces. Within static optimization methods, this assumption is formulated as an optimization problem, minimizing a target function dependent on the muscle activations of interest at each individual instance of time.

Note, that this approach, while basically relying on a reasonable hypothesis, might yield inappropriate solutions in certain situations as the effects of co-contraction, compensations for muscle fatigue, different activation patterns for highly accelerated movements or even subject-specific pathological deviations are partly or entirely omitted, depending on the modeled recruitment criterion. The computed activation results of a suchlike optimization procedure are a rather qualitatively estimation of true muscle forces and should be carefully interpreted, while also consulting well-studied activation patterns of comparable movements. Static optimization is therefore certainly the most speculative component within the musculoskeletal pipeline, albeit it is an established, computationally efficient method for muscle activation estimation. Whereas the outcomes of all previous stages are quite well quantifiable within the limits of numerical and propagated measurement errors, muscle activation estimations are mainly indicative results [Ojeda 11].

## 2.5.2 Muscle Recruitment Optimization

Following the principle of virtual work, the work done by muscles is formulated as the product of their force and their virtual length. If the geometry of a muscle  $M_i \in \mathbb{M}$  is modeled as a polyline that wraps around joints and tissues, the momentary muscle length between its two insertion points, whose position is dependent on the generalized coordinates, can be obtained by a function  $l_{M_i}(q)$  that measures the Euclidean distances between each pair of neighbored wrapping points. The muscle force  $f_{M_i}$  is actually a function of length and its derivative, i.e. the characteristic force-length and force-velocity relationship, so that  $f_{M_i} = f(l_{M_i}(q), \dot{l}_{M_i}(q))$ . The virtual work done by all muscles is then:

$$\delta W = \sum_{M_i \in \mathbb{M}} \delta l_{M_i}(q) f_{M_i} \quad (2.41)$$

With  $\tau_q^{(\mathbb{M})}$ , the component of virtual muscle forces extracted from the generalized forces vector  $\tau_q$  in equation 2.40, the same virtual work can also be formulated as the scalar product of  $\tau_q^{(\mathbb{M})}$  and the virtual displacements of generalized coordinates  $q$ :

$$\delta W = \delta q^T \tau_q^{(\mathbb{M})} \quad (2.42)$$

This can now be reformulated as follows:

$$C^{(\mathbb{M})} f^{(\mathbb{M})} = \tau_q^{(\mathbb{M})} , \quad (2.43)$$

where  $f^{(\mathbb{M})}$  is a vector of all unknown muscle forces  $f_{M_i}$  and  $C^{(\mathbb{M})}$  is a Jacobian matrix of derivatives of characteristic muscle length functions for the generalized coordinates  $q$ . More generally,  $C^{(\mathbb{M})}$  might be seen as a submatrix of  $C$  in the expression  $C f = \tau_q$ , where  $f$  is composed of a subvector of all unknown muscle forces  $f^{(\mathbb{M})}$  and additional reaction forces, and  $\tau_q$  is a vector of the generalized internal model forces, which are isolated by subtracting inertial forces from known ground reaction (or any externally applied) forces. As a consequence of the muscular redundancy problem, there are many more unknown forces than there are equilibrium constraints.

The muscle recruitment is then handled within the inverse dynamics analysis, whereas the system's indeterminacy is resolved using an optimization criterion in the following way:

$$\begin{aligned} \hat{f}^{(\mathbb{M})} &= \arg \min_{f^{(\mathbb{M})}} \left[ G \left( f^{(\mathbb{M})} \right) \right] \\ \text{s.t. } C f &= \tau_q, \end{aligned} \quad (2.44)$$

with  $G$  any appropriate target function [Skals 16]. Technically, static optimization inherently requires inverse dynamics and is hence implemented jointly.

### Optimization Criteria

The target function  $G$  is mostly chosen to be a polynomial of the normalized muscle forces [AnyBody Doc. 17, OpenSim Doc. 17], i.e.:

$$G \left( f^{(\mathbb{M})} \right) = \sum_{M \in \mathbb{M}} \left( \frac{f_{M_i}}{F_{M_i,0}} \right)^p, \quad (2.45)$$

with  $F_{M_i,0}$  the individual maximum neutral force or muscle strength. As mentioned above, the choice of  $G$  to minimize the overall sum of muscle forces is an assumption, based on the physiologically reasonable idea of an efficient muscle recruitment. The polynomial order might be varied in order to address different recruitment criteria: With  $p = 1$ , a linear recruitment will allocate more work to stronger muscles, such that a minimum number of muscles is chosen to provide equilibrium. This variant is, however, quite unlikely to model a natural recruitment strategy as it incorporates no muscle synergy effects such as load sharing of several muscles spanning the same joints. Instead, a quadratic polynomial penalizes large single forces in the sum, and is thus likely to account for suchlike effects in favor of a minimal solution. It is a well-established assumption in musculoskeletal analysis and experimentally supported by EMG measurements for certain motion scenarios. Generally, an increasing polynomial order emphasizes synergy effects such that muscles likely compensate for high load among each other especially if the force of an individual muscle reaches its implicit upper strength bound  $F_{M_i,0}$ . Higher order criteria, however, causes sudden changes in activation of muscles, leading to a volatile force distribution over time which might be physiologically impossible due to a certain maximum reaction speed of the muscle contraction process. Finally, for  $p$  to infinity,  $G$  yields a min-max criterion, balancing the external load among muscles as best as possible such that the maximum relative load of each muscle is minimized. This idea follows a minimum muscle fatigue or maximum synergism criterion [Rasmussen 01, Damsgaard 06, Skals 16].

It is assumed that different recruitment criteria are suitable in different loading scenarios and that a more physiological strategy under lower loading conditions activates only a minimum number of those muscles, which can effectively contribute a considerable amount of force with an advantageous moment arm. Under very high loadings, on the other hand, a maximum muscle synergism is favorable in order to raise the full strength of the musculoskeletal system. Hence, it might be also reasonable to combine lower and higher order terms of the above mentioned criteria in case of motion scenarios with varying loading conditions [AnyBody Doc. 17].



## 2.6 Outline: IMU-Driven Musculoskeletal Analysis

In the previous sections, a set of techniques to handle the fundamental issues of musculoskeletal analysis has been outlined and structured into respective stages of the analysis pipeline. In view of an overall long-term goal of an IMU-driven pipeline, associated sources of errors, methods to avoid them and still unresolved issues shall now be briefly assessed.

### Linkage of Motion Capture and Kinematics

Typically, there is a vaguely defined interface somewhere between motion capture, including the kinematics analysis and the remaining biomechanical part of the pipeline. This is firstly due to the technical fact that motion sequences captured with any hardware system have to be digitized and converted to a proper format, before they can be further processed and evaluated. Strictly speaking, human motion capture implies only the process of recording trajectories of a representative set of body landmarks, which is ideally sufficient in order to describe and recover the actual motion. The latter can only be adequately achieved if all this information, i.e. either marker trajectories or raw inertial sensor data and the related landmarks subject to an underlying skeleton model, are available and consistent. Altogether this data provides the input for a direct or inverse kinematics analysis. For this reason, available motion capture systems commonly supply their own technical skeletal models, including bony marker landmarks [OptiTrack Doc. 17, Roetenberg 09], or employ a marker protocol that implicitly defines the skeleton as is the case with the Vicon system and PiG [Kadaba 89, Davis 91]. Thereby, a kinematics solution is either obtained directly or by an inverse kinematics optimization. Anyway, these kinematic trajectories are dependent on the underlying model.

### Comparability of Kinematics and Skeletons

Detailed biomechanical models required for biomechanical analyses originate from anatomical studies and are often considerably different from technical models used in motion capture. Suchlike disparities might be classified into the following groups: different topologies of the skeleton graphs (e.g. more detailed anatomical segments), technical vs. biomechanical coordinate frame definitions and qualitatively different joint constraints. Different frame definitions taken by themselves may be easily converted into each other; however, joint constraints might be incompatible. Initially unrestricted and a posteriori constrained joints might make the captured trajectories become invalid. Lastly, mapping trajectories to topologically different skeletons leads to inevitable residual errors. In [Kainz 16] influences of different models and computation methods on anatomical kinematics have been studied and broken down into error source categories. The results show that the overwhelming majority of differences in kinematic trajectories can be attributed to the differences in the anatomical models mentioned above. The overall conclusion is that kinematic solutions are generally only comparable subject to the same underlying skeleton model. The influences of error induced by using different skeleton models on biomechanical variables might be negligible in a specific case, but are generally unknown. From a methodical perspective, it is hence advisable to avoid these errors by using the same kinematic model in all stages of the musculoskeletal analysis pipeline. In the case of an IMU-driven pipeline, this implies a sensor fusion approach that imposes all kinematic constraints of the biomechanical model used for further analyses.



### Specific Errors of Inertial Tracking

The optical marker-based method is known for its high technical tracking precision. Required precision is, however, predetermined by the application, and one might argue that biomechanical applications can hardly benefit from a sub-millimeter measuring accuracy of optical marker-based systems in the presence of marker displacements and soft tissue artifacts. Instead of marker errors, inertial tracking suffers from translational and rotational displacements between assumed and real IMU locations that appear as a consequence of an uncertain initial sensor-to-segment calibration [Miezel 16, Taetz 16], but also dynamically during a motion comparable to marker soft tissue artifacts. As a major source of errors within the IMU-driven motion capture approach, suchlike IMU-to-segment (I2S) calibration errors will propagate through the subsequent analysis stages and thus affect biomechanical variables of interest. The manifestation of these errors in later analysis stages provides an indication of the precision of biomechanical results that can be expected from an IMU-driven approach. If the deviations compared to the optical golden standard are significant in the presence of large errors, it should be evaluated what kinds of qualitative and quantitative I2S calibration errors are tolerable. This can also provide a precision target for self-calibration approaches. However, suchlike effects associated with inertial tracking must be distinguished from non-inherent errors, only arising from practical limitations of certain technical systems. Hence, model related errors as discussed above that could induce additional trajectory deviations should be avoided.

### Inertial Tracking and GRF Prediction

In order to overcome the limitations of GRF measurements, which are the inflexibility associated with force plate devices, but also possible dynamic inconsistencies as discussed in section 2.4.2, a GRF estimation approach is desirable for an IMU-driven analysis. While the force balance is essentially provided by the equations of motions and can be in principle solved with the top-down approach of inverse dynamics, a biomechanical system becomes indeterminate during double contact phases due to the close kinematic chain, formed with the ground plane [Fluit 14, Skals 16]. Thus, there is no unique solution for GRFs in this case. Different techniques using e.g. optimization methods or artificial neural networks have been proposed to overcome this issue [Audu 03, Choi 13]. Another approach is to distribute the GRFs during double stance phases using so called smooth transition functions, interpolated from empirical measurements. According to [Ren 08] the GRFs on the trailing foot decay smoothly towards zero in gait scenarios. While capable of predicting reasonable GRFs, these approaches are not universal in the sense that they rely on extensive training data and it remains rather unclear if they provide acceptable solutions outside their set of validated movements such as, for instance, typical gait cycles. Recently, a method that employs smooth transition distribution functions and relies solely on inertial data has been proposed in [Karatsidis 16]. The method yields excellent correlations and moderate relative mean square errors between predicted and measured GRFs during gait. However, it is dependent on a previously obtained set of conventional measurements for similar movements.



## 3. Conception and Implementation

After the foundations of musculoskeletal analysis, the generic analysis pipeline with its process stages has been presented in the previous chapter, a specific pipeline shall now be instantiated in respect of the goals of this thesis. These are firstly revisited and complemented with requirements for an appropriate implementation. Afterwards, the major unresolved issues required to accomplish the defined tasks will be discussed in detail from a methodical perspective. After providing an architectural overview of the design of the entire solution, implementation details will be specified in the final section of this chapter.

### 3.1 Conceptual Methodology

In due consideration of the approaches discussed thus far, pending specific requirements are outlined subsequently. Afterwards, appropriate solution approaches will be discussed in the same order.

#### 1. Hybrid-Driven Musculoskeletal Analysis Pipeline

A hybrid-driven musculoskeletal analysis pipeline, capable to take both inertial and optical marker-based motion capture trajectories as input, has to be taken into operation as a basic prerequisite. This is necessary in order to allow for a comparison of biomechanical results obtained from both motion capture approaches. An appropriate biomechanical framework suited for musculoskeletal analyses must be chosen and interfaces to the optical and inertial motion capture systems need to be implemented.

#### 2. Ground Reaction Force Prediction

With the long-term of a solely IMU-driven musculoskeletal analysis, the focus is on outlining a plain and flexible pipeline that is only dependent on a set of wearable IMUs as hardware equipment instead of an entire gait laboratory, but can still be optionally complemented with conventional measurements. However, this goal requires particularly an estimation of ground reaction forces, independent of any force plate measurements. A promising GRF prediction method proposed in [Fluit 14] and [Skals 16] shall hence be integrated into a conventional pipeline.

### 3. Simulation and Evaluation of IMU-to-Segment Calibration Errors

In order to accomplish a study of isolated I2S calibration errors, firstly virtual but realistic IMU trajectories, i.e. typical error prone accelerometer, gyroscope and magnetometer data, shall be simulated from optical marker-based motion trajectories and then systematically altered, according to defined I2S calibration errors in a systematic, controllable manner and tracked using the Quattracker approach. The resulting inverse kinematic trajectories provide the input for a musculoskeletal analysis which relies on the integrated GRF prediction approach. Together with the hybrid pipeline implementation as a basic prerequisite, the study of I2S calibration errors will constitute the practical part of this thesis. The effects of simulated I2S calibration errors on primarily predicted GRFs and eventually on muscle activations of the lower body shall be evaluated.

### 4. Towards an IMU-Driven Real Data Scenario

Biomechanical skeletons include detailed segments such as, for instance, distinct spinal segments, radius and ulna, foot and talus that are indistinguishable and covered by too much soft tissues or are just too small to be equipped with real surface-mounted IMUs. Technically, this results in an anatomically precise skeleton model, whose individual DoFs, however, cannot be fully and independently tracked as originally assumed in the Quattracker's formulation of biomechanical constraints. Whereas the virtual IMUs used in the simulation study are not subject to suchlike placement limitations, techniques to overcome these practical issues in real data scenarios must be conceived in order to provide a both anatomically correct and consistent skeleton model.

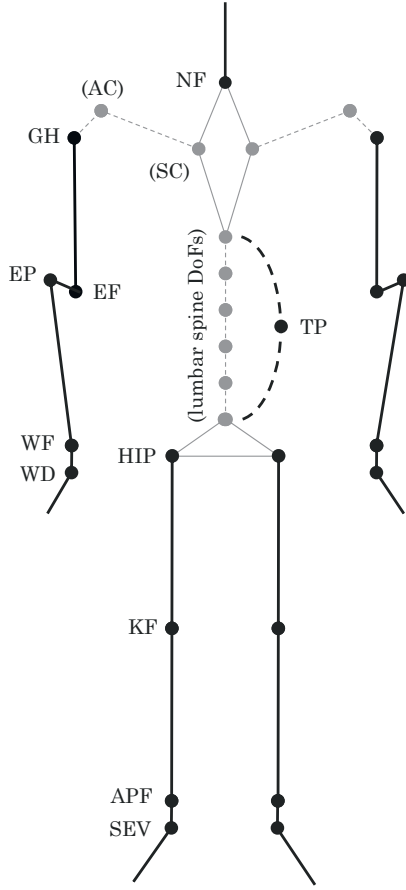
#### 3.1.1 AMS Musculoskeletal Analysis Framework

The AnyBody Modeling System<sup>1</sup> (AMS), providing comprehensive features within the scope of musculoskeletal modeling and simulation, has been chosen as the framework implementing the biomechanical part of the musculoskeletal analysis pipeline. The AMS includes all algorithms outlined in the previous chapter that are associated with conventional musculoskeletal analyses, driven on optical marker-based motion capture [AnyBody Doc. 17]. Focusing on multibody dynamics simulations of biomechanical systems, it will be used for inverse dynamics analyses including static optimizations in particular, and partly for inverse kinematics when it comes to optical marker-based tracking. The AMS framework supplies a biomechanical model repository with a full-body musculoskeletal model, suited for all process stages of the pipeline. The AMS model is based on several partial biomechanical models, which are in particular the shoulder and arm models, developed by the Delft Shoulder Group [Veeger 91, Van der Helm 92], the Twente Lower Extremity Model [Horsman 07] and a lumbar spine model, adapted from [De Zee 07]. A visualization of the full-body model is provided in appendix A.1.

#### Skeleton Model

The skeleton's torso consists of a pelvis, sacrum, a thorax and five lumbar spine segments, the shoulders and arms are modeled as a seven-DoFs chain of the clavicle, scapula, humerus, radius, ulna, a wrist and a hand segment and the legs with six DoFs are

<sup>1</sup>AnyBody Modelling System, AnyBody Technology A/S, Aalborg, Denmark

**Figure 3.1:** AnyBody skeleton model.

Abbrev.	DoFs	Description
NF	1×	Neck Flexion
TP	3×	Thorax Pelvis
(SCPV)	3×	Sacrum Pelvis
(L5SC)	3×	L5 Sacrum
(L4L5)	3×	L4 L5
(L3L4)	3×	L3 L4
(L2L3)	3×	L2 L3
(L1L2)	3×	L1 L2
(T12L1)	3×	T12 L1
GH	3×	Gleno Humeral
(SC)	3×	Sterno Calvicular
(AC)	3×	Acromio Clavicular
EF	1×	Elbow Flexion
EP	1×	Elbow Pronation
WF	1×	Wrist Flexion
WD	1×	Wrist Deviation
HIP	3×	Hip
KF	1×	Knee Flexion
APF	1×	Ankle Plantar Flexion
SEV	1×	Subtalar Eversion

**Table 3.1:** DOFs of the AnyBody skeleton.

composed of a thigh, shank, talus and foot segments. Figure 3.1 shows the skeleton and table 3.1 describes the anatomical DoFs, actuating the skeleton. The sternoclavicular and acromioclavicular DoFs may be chosen to be functions, dependent on the glenohumeral DoF, thus simulating a movement interaction, called shoulder rhythm, as described in [AnyBody Tech. 11]. Likewise, individual DoFs between lumbar spine segments (Sacrum, L1, L2, L3, L4, L5) are modeled as a function of an overall, virtual spherical thorax-pelvis joint and interact in a spine rhythm as specified in appendix A.3. All the dependent DoFs are denoted in parentheses, whereas the independent DoFs constitute the generalized coordinate set that sufficiently describes the skeleton's kinematic state.

## Muscle Model

Several muscle models are available, of which the most simple is a constant strength model with the maximum neutral force  $F_{M,0}$  as the only parameter. The second type contains a contractile muscle and series elastics tendon component and models the force as a bilinear function of the muscle length and contraction velocity. Finally, an implementation of a hill type model as introduced in section 2.1.6 is available and its parameters are summarized in table A.1 in the appendix. Note, that those parameters in the listing that were not mentioned in the basic hill type model, are basically used as a parametrization of the characteristic force-length and force-velocity functions. A complete muscle-specific parametrization is provided with the partial body models. The lower body

muscular system is comprised of 55 suchlike hill type muscles and 159 muscle paths per leg [AnyBody Doc. 17].

### AMS Pipeline

The AMS skeletal model is typically scaled within the inverse kinematics analysis of optical marker-based motion trajectories, following the approach of simultaneous motion and parameter optimization, proposed in [Andersen 10] and discussed in general in section 2.3.1. This process stage yields both inverse kinematic trajectories (typically represented as anatomical joint angle trajectories) and kinematic model parameters. However, all model parameters can be manually predefined or adapted. Before running the inverse dynamics including a static optimization, also a scaling of the dynamic body segment and muscle parameters based on the kinematic scaling parameters must be applied, which is implemented in the AMS and relies on length-mass-fat scaling techniques, outlined in section 2.1.5 and anthropometric tables [Winter 09, Lund 15]. The inverse dynamics process stage takes the anatomical joint trajectories and the kinematic model parameters as inputs and yields an extensive database of analysis results, including biomechanical variables such as joint reaction forces and muscle activations, but also kinetic measures.

#### 3.1.2 Ground Reaction Force Prediction

An optimization based approach for GRF Prediction will be used, which relies on a dynamic contact model and muscle-like actuators, defined at several contact points at the feet. The technique tackles the problem of dynamic underdeterminacy during double stance phases together with the muscle recruitment optimization, thus only requiring kinematic trajectories as an input. The method has been proposed in [Fluit 14] and validated for various activities of daily living. In [Skals 16] a slightly adapted version has been successfully evaluated for different sports-related movements and yielded strong to excellent correlations and moderate root means square differences between predicted and conventionally measured GRFs. Since this approach is not dependent on any training data or previous measurements it has been declared as a universal GRF prediction. While always satisfying the net force balance, prescribed by the equations of motion, the particular distribution among the feet is, however, subject to the chosen muscle recruitment criterion and might thus be inappropriate for e.g. pathological motion sequences.

#### Artificial Muscle-Like Actuators

Under each foot several contact points are defined and equipped with each five muscle-like actuators, of which four account for the friction forces in the ground plane and the fifth generates a normal force, aligned with the vertical GRF. The friction forces, accounting for the medio-lateral and antero-posterior GRFs, respectively, are each divided into two opposing forces in order to model them as contractile muscle actuators, which can only generate positive forces. For the normal force, this requirement is always fulfilled. Figure 3.2a illustrates the underlying Coulomb friction model and the five forces, i.e. friction forces  $F_f$  and the normal force  $F_n$ , involved for emulating a muscle-like actuation. The friction forces are restricted to  $\|F_f\| \leq \mu \|F_n\|$  with  $\mu$  the friction coefficient and are hence constrained to lie inside a circle of the ground plane, spanned by the friction cone as illustrated in figure 3.2b.

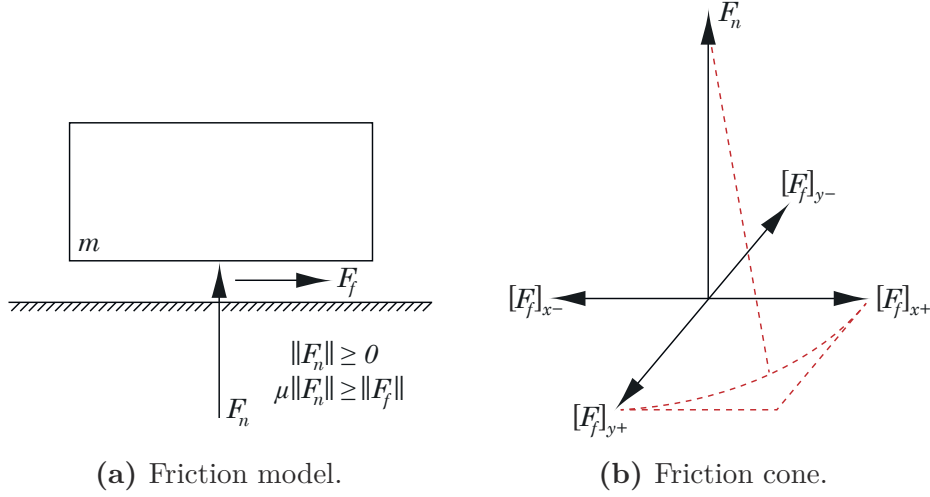


**Figure 3.2:** Coulomb friction model of friction forces and normal force.

### Contact Points and Contact Conditions

The contact points are located at several anatomical landmarks of the foot, where a ground contact can be expected such as, for instance, the heel, the base and head of the metatarsal bones as shown in figure 3.3. A vertical offset from the foot segment might be reasonable to compensate for the sole thickness of any footwear. Originally, 12 contact points were defined in [Fluit 14], later 18 were used in [Skals 16] and any higher number of carefully placed contact points will in principle contribute to a more precise estimation of the CoP.

Using a dynamic contact model, an actuator exerts force only if the contact conditions are met, which are defined via a height threshold and a maximum velocity constraint in order to assure that a certain point is close to the ground plane and nearly free of motion. To this end, for each contact point  $C_i$  a characteristic strength function  $c(C_i)$ , dependent on the point's vertical position  $[C_i]_z$  and velocity  $\dot{C}_i$  is defined:

$$c(C_i) = \begin{cases} F_{C_i, \max} & \text{if } \frac{[C_i]_z}{z_{\text{limit}}} \leq z_{\text{ratio}} \wedge \frac{\|\dot{C}_i\|}{v_{\text{limit}}} \leq v_{\text{ratio}} \\ F_{C_i, \text{smooth}} & \text{if } z_{\text{ratio}} \leq \frac{[C_i]_z}{z_{\text{limit}}} < 1 \wedge v_{\text{ratio}} \leq \frac{\|\dot{C}_i\|}{v_{\text{limit}}} < 1 \\ 0 & \text{otherwise,} \end{cases} \quad (3.1)$$

where  $z_{\text{limit}}$  and  $v_{\text{limit}}$  are absolute height and velocity thresholds, respectively, and  $z_{\text{ratio}}$  and  $v_{\text{ratio}}$  ratios that differentiate the full contact case from a smoothed transition zone.  $F_{C_i, \max}$  may be an individual maximum actuator force which was, however, chosen to be constant for all contact points and set to a fraction of the subject's body weight force. According to a sensitivity analysis conducted in [Fluit 14], the exact values of  $z_{\text{limit}}$  and  $v_{\text{limit}}$  had a minor influence on the GRF solution. The smoothing transition ratios  $z_{\text{ratio}}$ ,  $v_{\text{ratio}}$  are used to control a transition contact zone, where the force  $F_{C_i, \text{smooth}}$  is used to smooth out jumps in the activation profile, thus preventing discontinuities of the predicted GRFs:

$$F_{C_i, \text{smooth}} = F_{C_i, \max} z_{\text{smooth}}(C_i) v_{\text{smooth}}(C_i), \quad (3.2)$$



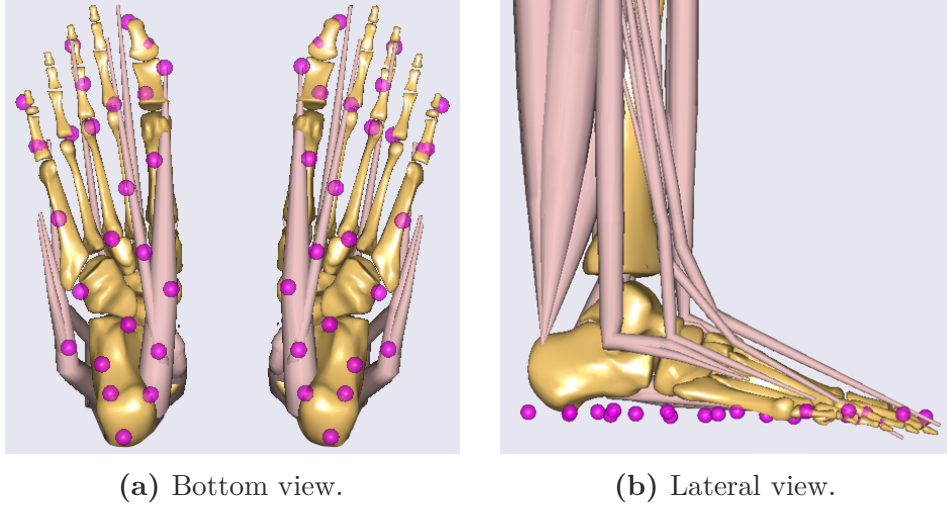


**Figure 3.3:** Foot contact point definitions visualized in the AMS.

where  $z_{smooth}$  and  $v_{smooth}$  may be any appropriate window functions, dependent on the contact point's vertical height and velocity. In [Skals 16] the following cosine profiles have been used:

$$z_{smooth}(C_i) = \frac{1}{2} \cos \left( 1 + \frac{\left( \frac{[C_i]_z}{z_{limit}} - z_{ratio} \right)}{(1 - z_{ratio})} \pi \right) \quad (3.3)$$

$$v_{smooth}(C_i) = \frac{1}{2} \cos \left( 1 + \frac{\left( \frac{\|\dot{C}_i\|}{v_{limit}} - v_{ratio} \right)}{(1 - v_{ratio})} \pi \right) \quad (3.4)$$

### Integration into the Muscle Recruitment Optimization

Each artificial actuator is now treated similarly to a muscle and incorporated into the muscle recruitment optimization (cf. equation 2.44). However, as already mentioned, the friction forces are constrained by the friction cone which implies a square root expression that is unsuited for the linear optimization formulation:

$$\|F_f\| \leq \sqrt{[F_f]_x^2 + [F_f]_y^2} \leq \mu \|F_n\| \quad (3.5)$$

It is therefore deliberately dropped, which causes the friction forces to be slightly overestimated as they are then bounded by circumscribed triangles instead of circles as illustrated in figure 3.2b. Estimations of GRFs, that are consistent with the equations of motion, can now be computed as a part of the muscle recruitment within the inverse dynamics analysis of the AMS.

#### 3.1.3 Simulation of I2S Calibration Errors

For a simulation of I2S calibration errors, kinematic reference trajectories must be systematically altered. To this end, firstly a motion sequence is captured using a conventional optical marker-based method and the inverse kinematics with respect to the AMS skeleton is obtained. The skeleton is then extracted from the AMS environment and a set of virtual



IMUs is assigned to each segment in a one-to-one mapping by means of I2S transformations, describing the respective relative positions and orientations. In the most simple case, the virtual IMU Positions coincide with the respective segment frame. However, for a realistic simulation, IMUs are assumed to be located in a lateral or anterior direction on the surface of the body segments. The entire set of suchlike transformations is the I2S calibration of the virtual IMU set with respect to the skeleton, and errors may now be added by modifying individual transformations. The relative change between the initial and the altered calibration is the I2S calibration error. Next, the AMS skeleton is driven by the inverse kinematics solution, i.e. the anatomical DoFs are actuated with the computed joint angle trajectories, and trajectories of both the original and altered global positions of the virtual IMU set are calculated. Based on that, realistic inertial trajectories with and without I2C calibration errors can be simulated by means of data differentiation and an addition of typical sensor errors [Shuster 93, Miezal 16].

### 3.1.4 IMU-Trackable Anatomical Skeleton

The IMU simulation setup mentioned above makes assumptions on both the simulated IMU trajectories, but most notably on a one-to-one I2S mapping. While deviations between simulated and real sensor data are inevitable, but can be limited by implementing realistic error models, the requirement of an anatomical skeleton, where each segment can be directly tracked by an IMU, can be hardly met in practice. The one-to-one I2S mapping is not feasible for a real inertial tracking scenario if a detailed anatomical skeleton such as the AMS model is used since smaller segments cannot be equipped with IMUs. Figure 3.4 illustrates the AMS model with a feasible subset mapping. Some anatomical DoFs are not covered as they cannot be directly tracked with individual sensors and are encircled in green and red. There are indeed two distinct cases: at the shoulder and spine the DoFs between several segments are unknown, and the corresponding inverse kinematics solution is hence truly underdetermined. In the other case, i.e. the elbow, wrist and ankle, two DoFs are distributed between two segments and are each modeled as a one-dimensional hinge joint. These two DoFs might be in principle reconstructable from an overall relative orientation between the IMUs of incident joints. The decomposition of the known overall rotation in respect of two joint axes, which are not orthogonal is, however, not trivial and will be discussed later.

#### Shoulder and Spine Rhythm

Firstly, the solution for the former, underdetermined case can be borrowed from the AMS inverse kinematic where the intermediate, dependent DoFs at the shoulder and spine are simply interpolated as a function of independent DoFs. For the shoulder rhythm, the acromioclavicular and sternoclavicular DoFs are functions of the three glenohumeral DoFs. The spine rhythm, on the other hand, distributes the relative rotation measured at a virtual thorax-pelvis joint linearly over the intermediate lumbar spine segments. The implementation of both shoulder and spine rhythm, as defined in the AMS, are provided in appendix A.3. Note, that these functions must be implemented as constraints into the Quattracker method, in order to obtain a consistent inverse kinematics, in the sense of an EKF-based solution. For the spine rhythm, also the method proposed in [Miezal 14] is suitable.

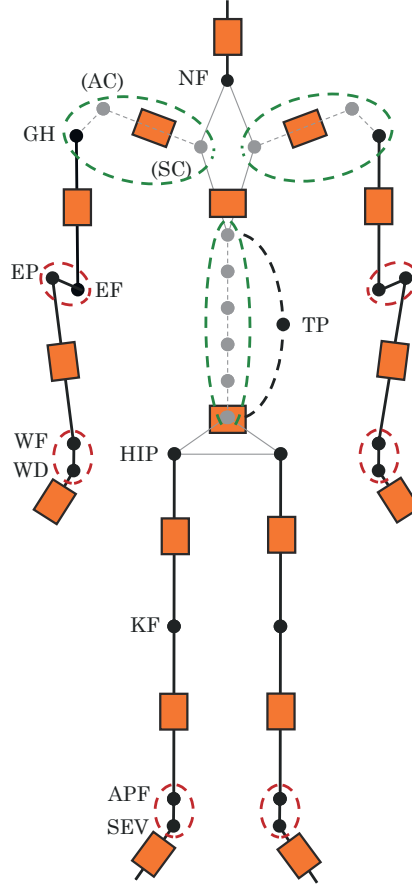


**Figure 3.4:** AMS skeleton equipped with IMUs at all trackable segments.

### Arbitrary Two-Axes Joint Constraints

Next, a rotation decomposition is required in order to distribute the known relative rotations at elbow, wrist and ankle over the respective two joint axis. For convenience, the small intermediate segments, i.e. the (partial) ulna, wrist and talus segments, will be omitted and their incident, larger segments are fused with biaxial joints, instead of the former two-segment hinge chain. Note, that this simplification is equivalent from a rotational point of view. Small translational errors, however, must be expected due to the small but nonzero length of the omitted segments. In case of orthogonal joint axes, a rotation can then be easily decomposed using its Euler angle representation and may be implemented as a joint constraint by penalizing the residual component. While the DoFs at the wrist and elbow are approximately orthogonal, this assumption is invalid for the ankle, where the ankle plantar flexion axis and the subtalar eversion axis form an angle of nearly  $60^\circ$  [Horsman 07]. Note, that in this case also the swing-twist decomposition introduced in section 2.1.3 provides no remedy.

A generalization of an Euler angle decomposition about three arbitrary rotation axes has been proposed in [Piovan 12], where also the case of a pure two-axis rotation can be derived. Let  $a_1, a_2 \in \mathbb{R}^3$  with  $a_1 \neq \pm a_2$  be unit-length vectors, describing two rotation axes and  $R$  be a rotation matrix in  $SO(3)$ .  $R$  can be uniquely decomposed into two

rotations about  $a_1$  and  $a_2$  if and only if:

$$a_1^T a_2 = a_1^T R a_2 , \quad (3.6)$$

where the respective angles are given by:

$$\theta_1 = \text{atan2} \left[ \frac{(R a_2)^T a_1 \times a_2}{a_2^T (R a_2) - (a_2^T a_1)((R a_2)^T a_1)} \right] \quad (3.7)$$

$$\theta_2 = \text{atan2} \left[ \frac{(R a_1)^T a_2 \times a_1}{a_1^T (R a_1) - (a_1^T a_2)((R a_1)^T a_2)} \right] . \quad (3.8)$$

In order to penalize a rotational component around an axis, different from  $a_1$  and  $a_2$ , i.e. if  $R$  is not exactly decomposable around the two axes, equation 3.6 can be reformulated as follows:

$$e_{2axes} = \|a_1^T a_2 - a_1^T R a_2\| , \quad (3.9)$$

where  $e_{2axes} \in [0, 1]$  is a measure of the remaining non-decomposability.

In this way, biaxial non-orthogonal joints can be easily constrained and implemented in the Quattracker. Moreover, the general approach introduced in [Piovan 12] provides a plain and concise method to handle any multiaxial joints, which might be preferable to the inconvenient swing-twist decomposition.

### 3.1.5 Design Overview

An overall system design should cover the three usage scenarios, i.e.: a conventional optical marker-based analysis, a simulation and alteration of IMU trajectories, based on optical tracking and eventually a real data IMU-driven process. Figure 3.5 shows the pipeline instantiated with the AMS as the biomechanical component, the Quattracker and the I2S trajectory simulation component for simulating and tracking inertial data. The design allows for three possible process flows that reflect the mentioned usage scenarios. Technical details as well as the implementation of interfaces are documented in the subsequent section.

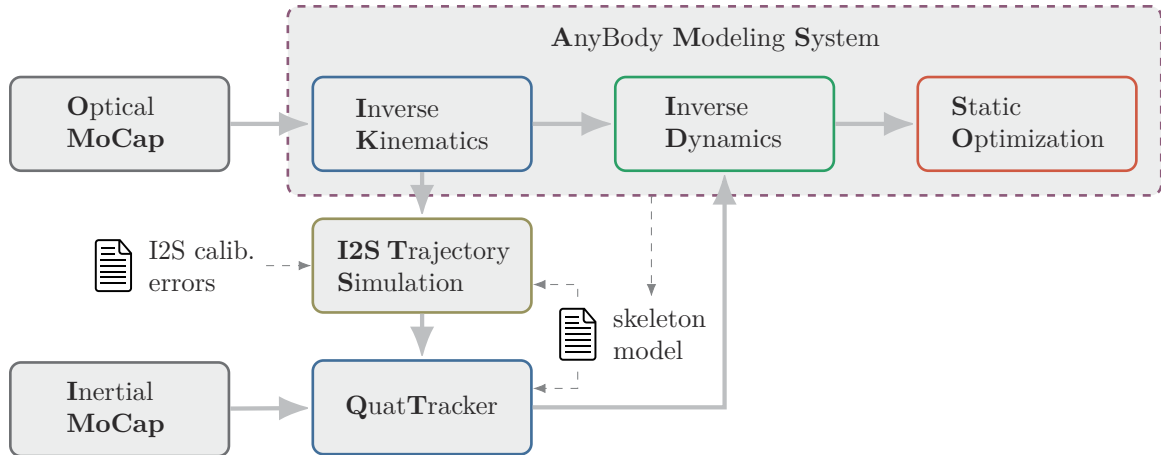


**Figure 3.5:** Design of the hybrid-driven musculoskeletal analysis pipeline.

## 3.2 Implementation Details

Subsequently some technical details of the discussed methods will be stated as well as remarks regarding the implementation of the overall system, in which several technical subsystems are involved.

### 3.2.1 Subsystems and Interfaces

**OptiTrack:** For optical marker-based motion capture the OptiTrack<sup>2</sup> system comprised of 12 infrared cameras and passive reflective markers is used. Albeit the provided software (Motive) is capable to solve the inverse kinematics in respect to a predefined, technical skeleton, only the raw marker trajectories are considered. Due to the simplified skeleton, which differs substantially from the AMS model, the output kinematics cannot be converted to biomechanical coordinate frames and turned out to deviate significantly from expected anatomical trajectories. For this reason, the inverse kinematics is solved by the AMS, which takes marker trajectories in the common binary C3D<sup>3</sup> format as an input.

**Xsens:** For inertial motion capture the wireless sensor systems of Xsens<sup>4</sup> are used. Although, the studies conducted within this thesis involve only simulated inertial data, for the sake of completeness and for future investigations, it should be mentioned that Xsens provides a real-time skeleton tracking solution (MVN framework). However, the skeleton is again incompatible with detailed biomechanical models and contains only the larger, trackable segments, connected with unconstrained spherical joints. For any further musculoskeletal analyses based on real data, the raw inertial sensor data, provided as XML data, should be used, and the inverse kinematics should be computed through a sensor fusion approach, considering biomechanical constraints.

**Mars:** Mars is a C++ framework developed at the wearHEALTH group that includes implementations of inertial sensor data interfaces and simulations, kinematics, a skeleton visualization and filtering and tracking algorithms. Both, the inertial trajectory simulation and the Quattracker, are implemented as components within Mars.

**AMS:** The AMS has several technical interfaces, which include the mentioned C3D import along with several additional marker trajectory formats and an output of all biomechanical analysis results together with the predefined analysis and AMS model parameters in the binary HDF<sup>5</sup> format. The biomechanical model and any specific analyses within the AMS are implemented in a C++-like interpreted script language, called AnyScript<sup>6</sup>, which allows an own development or modification of existing models and studies. The routines of the proprietary AMS core framework are invoked from script code and a CSV import and export of all data associated with models, study parameters and results is supported. In this way, the AMS model, or more precisely its kinematic parameters, can be made externally available to the I2S trajectory simulation and Quattracker algorithms. Moreover, the AMS includes a console interface, which can be controlled from external applications.

<sup>2</sup>OptiTrack Motion Capture Systems, NaturalPoint, Inc., Corvallis, U.S.A

<sup>3</sup><http://www.c3d.org>

<sup>4</sup>Xsens Technologies B.V., Enschede, The Netherlands

<sup>5</sup><http://www.hdfgroup.org>

<sup>6</sup><http://forum.anyscript.org>

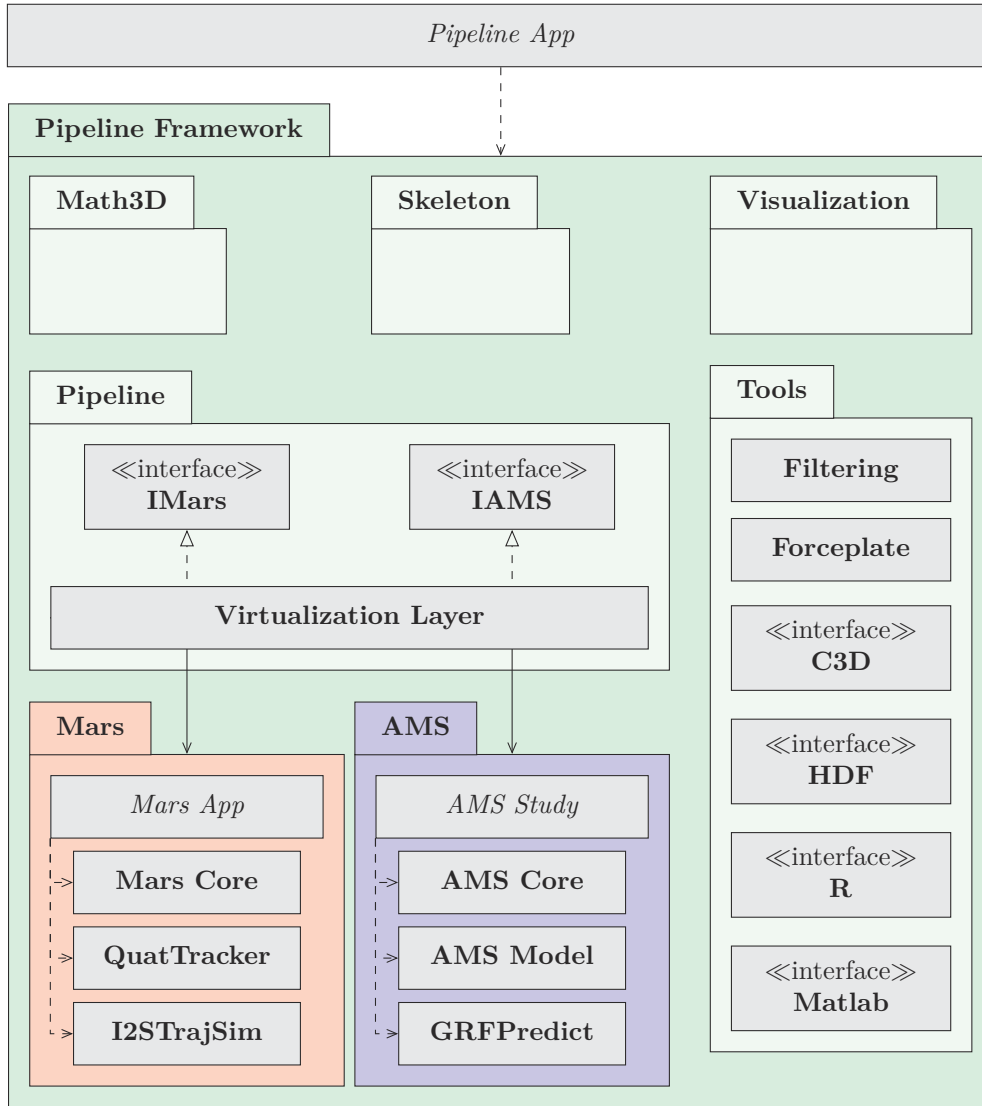


**Figure 3.6:** Architectural overview and components of the pipeline framework.

### 3.2.2 Pipeline Framework

In order to conduct studies that make use of the above mentioned subsystems, a pipeline framework has been implemented as a unified solution within the scope of this thesis. The pipeline framework comprises the implementation of all required interfaces between interacting subsystems, and provides a higher level abstraction layer, which allows to control Mars and the AMS. In this way, studies that involve several subsystems can be consistently implemented as self-contained applications, and the analysis results can be either processed using internally coded evaluation routines or passed to external software via interfaces to R and Matlab. The pipeline framework has been implemented in C#, and an architectural overview is illustrated in figure 3.6.

Most notably, a visualization layer is inserted that allows to run the AMS and Mars frameworks on virtual machines and control them through SSH. This accounts for the different operating system requirements of both systems and also allows an easy deployment on different physical machines. However, the Mars core framework has also been ported

to Windows, allowing for a native execution of the overall system on the same physical machine. A pipeline application may connect to the two interfaces that abstract from the underlying instantiation and execution method and thus facilitate a data-driven communication with Mars and the AMS.

A concise spatial math library as well as a generic skeleton model, abstracting from the specific modeling implementations of the subsystems, as well as a visualization component for skeleton rendering have been implemented. The tools package contains I/O data interfaces (C3D incl. force plate data, HDF, R and Matlab), together with a collection of signal processing filters.

### 3.2.3 AMS GRF Prediction Integration

The GRF prediction method was integrated into the AMS pipeline following the basic template provided in [AnyBody Tech. 16]. To this end, the force plate models were excluded from the standard model and virtual, conditional contact plates, implementing the ground contact conditions as discussed in section 3.1.2, had to be added instead.

The following code snippet shows the different setting of the conditional contact class, where obligatory properties are marked with `<...>` and optional values with `[...]`.

---

```
FootPlateConditionalContact <ObjName> (
  NORMAL_DIRECTION = [ "X"|"Y"|"Z" ],
  NUMBER_OF_NODES = [ 1 ... 200 ],
  NODES_BASE_FOLDER = <NodeFolder>,
  PLATE_BASE_FRAME = <RefFrame>,
  SHOW_TRIGGER_VOLUME = [0|1] ) =
{
  Settings =
  {
    [ LimitDistLow = -0.10; ]
    [ LimitDistHigh = 0.03; ]
    [ LimitVelHigh = 0.5; ]
    [ Radius = 10; ]
    [ Strength = 200; ]
    [ FrictionCoefficient = 0.5; ]
    [ ForceVectorDrawScaleFactor = 0.0005; ]
  };
};
```

---

**Listing 3.1:** Conditional contact plate template [AnyBody Tech. 16].

The class properties and optional values are described below:

PLATE\_BASE\_FRAME: Reference frame where, ground planes will be attached.

NORMAL\_DIRECTION: Normal direction of the ground plane.

NODES\_BASE\_FOLDER: Folder, where all contact nodes will be located.

NUMBER\_OF\_NODES: Desired number of total contact nodes per foot.

SHOW\_TRIGGER\_VOLUME: Option to visualize the contract trigger volume.

**LimitDistLow:** Lower height contact threshold  $z_{limit-}$  [m].  
**LimitDistHigh:** Upper height contact threshold  $z_{limit+}$  [m].  
**LimitVelHigh:** Maximum velocity threshold  $v_{limit}$  [m s<sup>-1</sup>].  
**Radius:** Radius of the contact points [mm].  
**Strength:** Maximum force of the muscle-like actuators [N].  
**FrictionCoefficient:** Static friction coefficient [1].  
**ForceVectorDrawScaleFactor:** Scale factor for force visualization [1].

Some predefined function profiles for smoothing the transition zones between partial and full contact phases are available, which are linear, cosine and B-spline functions and can be parametrized via control ratios similar to  $z_{ratio}$  and  $v_{ratio}$ . In addition to the method used in [Skals 16], the profile function may also be dependent on the triggered contact radius property.

### 3.2.4 Ground and Foot Marker Plane Correction

The dynamic contact model of the GRF prediction method assumes a plain ground plane or alternatively an accurate modeling of uneven grounds through position dependent ground contact conditions. However, even optical marker-based data, captured in a gait laboratory, might be distorted by either a truly uneven ground or a biased calibration of the camera system, therefore containing marginal slopes in the vertical trajectory components, which can lead to height difference of a few centimeters for a gait path of several meters. This might result in a foot touchdown outside of the globally defined contact zone, which cannot be detected or, otherwise, in slightly biased CoP estimation. In order to rule out this possibility apriori, ground plane correction methods for raw marker trajectories have been implemented.

#### Ground Plane Correction

For the detection of uneven grounds, trajectories of foot markers, i.e. the first and fifth metatarsal head and heel points, are analyzed. During ground contact phases of the feet, the position-dependent ground height can be reconstructed through their vertical components, where only local minima are possible contact point candidates. A zero-velocity threshold applied to the time-differentiated candidate zones is used as an additional filter. The remaining points are assumed to be part of the true, local ground plane. In order to estimate a corrected global ground, a regression plane of all such points is computed in least-squares sense, using a singular value decomposition. To this end, the centroid of all  $n$  ground candidate vectors is computed and subtracted from them. A  $3 \times n$  matrix  $M$  is formed from the column vectors of the mean corrected points and the SVD  $M = U\Sigma V^T$  is computed. The best fitting plane is then described by the left singular vector in  $U$ , corresponding to the least singular value in  $\Sigma$ , as the normal vector and the previously computed centroid as the support vector (cf. [Gander 08]). All trajectories are then updated with respect to the corrected ground plane by rotating the entire point sampling volume by the rotation between the new ground normal and the former vertical unit vector. A shortest arc rotation quaternion  $q_R$  between two vectors  $v_1, v_2$  is found in an axis-angle representation, according to Rodrigues' formula (cf. [Piovan 12]) as follows:

$$q_R = \left( \sqrt{\|v_1\|^2 \|v_2\|^2 + v_1^T v_2}, (v_1 \times v_2) \right)^T, \quad (3.10)$$



where  $v_1 \times v_2$  is the cross product of the two vectors.

Similar to a global ground plane correction, individual fitting planes can be found for each foot touchdown zone and used to estimate the ground along the gait path. For all areas between contact zones, the true ground surface is unknown and may be interpolated from the normals of the neighbored fitting planes. The method might also be helpful to model discontinuous ground such as stairways, and can then be used to automatically define the contact conditions of the GRF prediction rather than correcting the marker trajectories.

### Foot Marker Plane Correction

Although the AMS inverse kinematics routine can optimize marker positions relative to the segments, some of them must be certainly fixed in order to provide valid initial conditions. The foot markers are quite critical for predicting valid GRFs and an exact positioning and a proper fixation are challenging, especially if they cannot be directly attached to the skin. Due to this uncertainty, one might want to ideally optimize all the three transitional components, which is, however, not possible. Since the GRF contact conditions are particularly dependent on the height component of foot markers, the following trade-off is made: After applying the above mentioned global ground plane correction, for each foot the three markers are orthogonally projected onto the ground, during a trusted, known double contact phase such as a standing position. For the entire motion sequence, these constant transformations are applied to the foot markers such that they span a new foot marker plane, which will coincide with the ground plane in case of plain and even touchdowns. Consequently, the height component of the expected foot marker points in the AMS model can be fixed to the ground level for the marker trajectory optimization, while the others remain free for adaptations.



## 4. Study Design and Evaluation

### 4.1 Setup

Within the scope of this thesis, five substudies were conducted. For the sake of clarity, they are firstly defined in detail, before the utilized materials and methods are discussed.

#### 4.1.1 Substudies

##### 1. Functional Tests and GRF Prediction Validation

First of all, the pipeline framework and the functionality of the AMS with the integrated GRF prediction was tested. At the same time, the usefulness of the foot and ground plane correction methods and reasonable parametrizations for the initialization of the AMS motion and parameter optimization were evaluated. As a starting point for all further analyses, the effectiveness of the GRF prediction method was examined and the findings in [Fluit 14] and [Skals 16] should be validated. For the exemplary standard gait data provided with the AMS, the correlations and root mean square errors between predicted and measured GRFs were expected to be in consensus with the results of the mentioned papers. Furthermore, performance measurements of the AMS analyses as well as the EKF-based tracking were gathered for estimating the computational effort for a single data set, in order to schedule test samples for the subsequent studies.

##### 2. Foot Posture Sensitivity

Before conducting any I2S calibration error simulations, the influences of solely altered anatomical foot kinematics on the GRF prediction method were investigated. This accounted for a suspected sensitivity of predicted forces and moments for variations of the foot posture during touchdown. To this end, only the two modeled anatomical ankle DoFs, i.e. the ankle plantar flexion (APF) and subtalar eversion (SEV), of the captured marker-based trajectories were systematically changed by adding disturbances in the range of  $\pm 15^\circ$  in a sampling step of  $2.5^\circ$  to each DoF individually. An isolated study of these effects was targeted, because I2S calibration errors induce angular errors, which might be not preventable through anatomical constraints in case of approximately collinear

axes of disturbance rotations and joints, and thus also affect the foot posture. It was hypothesized that the zero-velocity and contact zone conditions at the feet contact points could negotiate moderate variations, so that reaction forces would slightly deviate from forces predicted through undisturbed kinematics. However, reaction moments could likely differ to a greater extent due to biased CoP estimations.

### 3. I2S Calibration Errors

For the simulation of I2S calibration errors, only the lower body was considered, and errors were successively induced at the IMUs of the pelvis, thigh, shank and foot segments of the right lower limb. Based on a fixed, initial I2S attachment, the placement of IMUs was systematically altered around the segment axis and the lateral axis. An angular error range of  $\pm 12^\circ$  per axis with a sampling step of  $2^\circ$  was chosen, corresponding to a typical interval of soft tissue artifacts. Figure 4.1 shows the lower body IMUs and their placement relative to the segment frame, which coincides with the disturbance rotation axes  $\theta_{seg}$  and  $\theta_{lat}$ . Due to the dimensioning of a real sensor's casing, angular errors around the remaining, third axis were considered unlikely and omitted. In order to simulate a realistic placement on the surface of the body segments, IMUs were offset along the lateral axis from the origin of the segment frame. The following bone-to-surface radii were used for the individual segments: 2 cm at the pelvis, measured from the posterior superior iliac spine, 7 cm at the thigh, 5 cm at the shank and 3 cm at the foot, measured from the bone segment axis, respectively. Corresponding to the usual placement options of real sensors, two initial attachment configurations were considered: an anterior configuration, where IMUs were assumed to be placed on the anterior side of the segments and a second lateral configuration. In each case, the IMU at the pelvis, however, was assumed to be attached posterior, on the spinal side.

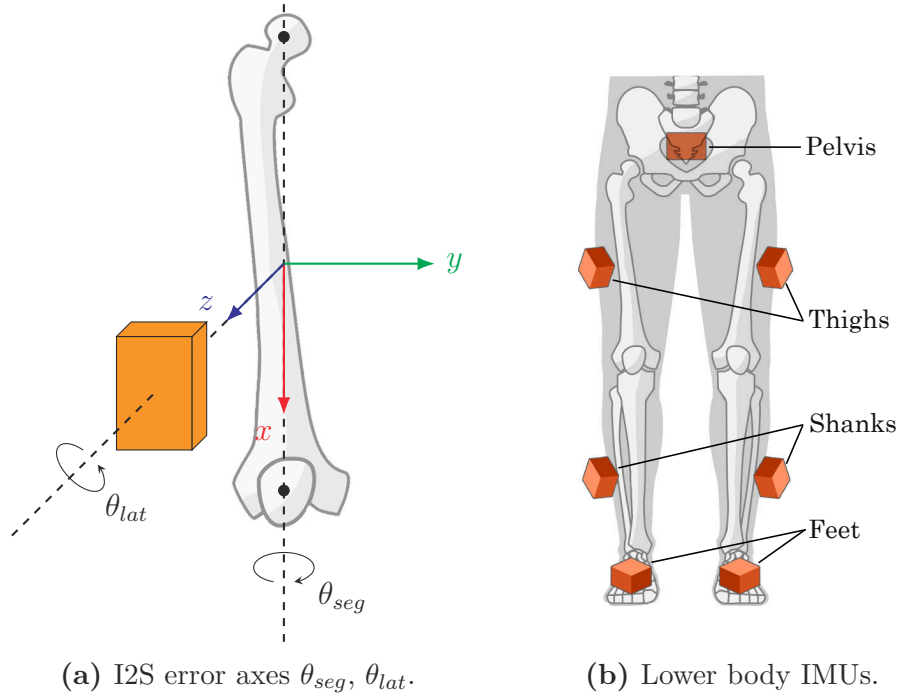


**Figure 4.1:** Simulated I2S errors around the segment and lateral axes of lower body segments.

#### 4. Typical I2S Calibration Error Scenario

In a real IMU-tracking scenario, I2S calibration errors are likely distributed differently with varying magnitudes over all the tracked segments. In order to evaluate their effects in combination, errors at all lower body segments were simulated using a Monte Carlo method. For this purpose, initially an anterior or lateral IMU configuration was chosen randomly per sample and then altered with different I2S calibration errors, randomly drawn with a uniform probability from the entire error sampling range. In contrast to the systematic, isolated error simulation, this substudy was designed to investigate the overall effects of typical calibration errors, thus representing a more realistic average scenario. A sample size of  $N = 100$  was chosen as a tradeoff between computational effort and significance. Also the individual and weighted, total muscle activations  $a$  in the form of normalized muscle forces were evaluated in this scenario and compared against the undisturbed reference data.

#### 5. Skeleton Trackability

In order to overcome the limitations of the one-to-one I2S mapping in view of an eventual real data scenario, the two methods for real skeleton trackability, discussed in section 3.1.4, i.e. the shoulder and spine rhythm and particularly the arbitrary two-axes joint constraint were briefly tested. To this end, a two version of the AMS skeleton were build: a lower body trackable version, where the talus segments were omitted and the ankle and subtalar joints were fused using the two-axes constraints, and a full-body trackable version, where additionally the spine segments and the shoulder segments (clavicle, scapula) were replaced by single, bridging segments. The former version was expected to induce no significant kinematic errors, compared to kinematic trajectories tracked with the original skeleton. The latter, full-body version, however, was assumed to alter the kinematics to some extent, especially in terms of the upper body DoFs. Note, that the two-axis joint constraint was implemented in the Quattracker and should be rotationally equivalent to the original two single-axis constraints. In contrast, the shoulder and spine rhythm were not implemented as constraints and only applied after the tracking in order to reconstruct a full-body kinematic solution for the AMS. The influences of kinematic disturbances on predicted GRFs and GRMs were tested in both cases.

#### 4.1.2 Methods and Materials

For the basic functional tests of the AMS pipeline as well as a test and validation of the GRF prediction, gait data supplied with the AMS was used. The data comprised three straight-line walking scenarios at a normal speed, performed by a male subject with a body height of 1.73 m and a mass of 62 kg. Full-body marker trajectories were captured with a sampling frequency of 100 Hz using the standard PiG marker set. All C3D files included analog force plate measurements sampled with 1000 Hz, which were used for a comparison with the predicted GRFs. Additional functional tests to evaluate the features of the AMS were conducted with the help of motion capture data from the Whole-Body Human Motion Database<sup>1</sup> [Mandery 15] of the KIT, Karlsruhe.

For the remaining studies, several motions of a 26 year old, healthy male subject with a body height of 1.72 m and a mass of 70 kg were recorded at the laboratory of the

<sup>1</sup><http://motion-database.humanoids.kit.edu>

wearHEALTH group. However, due to the high computational effort of analyzing an entire sampling set, only a normal gait scenario of 5 footsteps with a total length of 400 frames sampled at 120 Hz was chosen, which is comparable to the above mentioned gait sequences. With the aid of an OptiTrack system, consisting of 12 infrared cameras, full-body trajectories were captured according to a PiG marker set. No force plate devices were available, and the inverse dynamics analyses were therefore solely based on predicted GRFs.

### General Procedure

Raw marker trajectories were adapted using the global ground plane correction and the foot marker plane correction. In order to obtain a scaled model along with the optical marker-based reference kinematics, the standard motion and parameter optimization routines of the AMS as described in section 2.3.1 were run. The weighting of the foot marker points was increased threefold to enforce a precise tracking of the feet. The kinematic model was scaled based on measured joint-to-joint segment lengths, the body height and mass of the subject. The segment masses were distributed according to [Winter 09] and a length-mass-fat scaling law, as proposed in [Rasmussen 05], was applied. The shoulder and spine rhythm methods were used in order to compute the trajectories of respective upper body DoFs and, apart from that, the unchanged AMS full-body model was used.

The optical marker-based kinematics obtained in this way, as well as the GRFs predicted based on that, were generally considered as ground truth data; however, for the I2S calibration error study, also the unaltered, error free IMU trajectories, simulated from the optical data and tracked with the Quattracker, were considered as veridical target. A biomechanical fusion formula in the Quattracker's EKF implementation ensured that the skeleton's feet always touched the ground plane during contact phases, even for major kinematic deviations from the original trajectories due to the presence of calibration errors. This was achieved by defining three contact points per foot at the first and fifth metatarsal heads and the heel constrained with zero-velocity and height thresholds similar to those of the GRF prediction approach. The tracked trajectories were finally converted to anatomical joint angles and filtered with a 2nd order zero-phase Butterworth low-pass filter at 5 Hz. These smoothed trajectories provided the input for the AMS inverse dynamics routine.

The GRF prediction parametrization followed closely the method described in section 3.1.2. In contrast to the approach proposed in [Skals 16], 25 contact points under each foot were used, and a ground contact zone was defined through a lower and an upper height threshold of  $z_{limit-} = -0.10$  m and  $z_{limit+} = 0.03$  m. The zero-velocity threshold  $v_{limit}$  was decreased to  $0.5 \text{ ms}^{-1}$ . For the muscle activation estimation, the unchanged muscular system with parametrizations provided in the AMS partial body models and a cubic polynomial muscle recruitment optimization criterion were used. Although only major lower body muscles were of interest, the entire body was actuated with muscles. Note, that activations computed by the static optimization are technically muscle forces normalized by the muscles' particular maximum forces. Additionally to individual activations, a total activation over all modeled lower body muscles was computed by weighting the individual activations, according to their relative maximum muscle strength, i.e. the proportion of a muscle's maximum strength to the total maximum strength of all lower body muscles,

thus giving more weight to stronger muscles. All muscle activations were smoothed using a 2nd order zero-phase Butterworth low-pass filter at 5 Hz.

### Measures and Notations

GRFs are usually measured in a force plate reference frame and thus ground reaction moments, particularly dependent on the CoP, are not directly comparable among different motion sequences. For this reason, ground reaction forces and moments were compared in a reference frame that originates in the subject's ankle joint center, projected onto the ground plane with the x-axis pointing the direction of the movement and the z-axis pointing upwards, perpendicular to the ground. Hence,  $F_x$  is the antero-posterior,  $F_y$  the medio-lateral and  $F_z$  the vertical GRF, whereas  $M_x$  is the frontal,  $M_y$  the sagittal and  $M_z$  the transverse GRM. In order to make GRFs generally comparable and independent of subjects, they were furthermore normalized in respect to the body weight force, and moments were normalized in respect to the body weight and height, accordingly.

The following notations for statistical measures of a sample  $x$  were used:  $\bar{x}$  for the mean,  $\tilde{x}$  for the median,  $\check{x}$  and  $\hat{x}$  for the minimum and maximum values, respectively, and  $s_x$  for the standard deviation.

In order to compare (trajectories of) two variables  $x, y$ , the Pearson correlation coefficient  $r(x, y)$  and the relative root mean square error  $e_R(x, y)$  were used, defined as usual by:

$$r(x, y) = \frac{\sum_i^n (x_i - \bar{x})(y_i - \bar{y})}{\sqrt{\sum_i^n (x_i - \bar{x})^2} \sqrt{\sum_i^n (y_i - \bar{y})^2}} \quad (4.1)$$

$$MSE(x, y) = \frac{1}{n} \sum_i^n (x_i - y_i)^2 \quad (4.2)$$

$$RMSE(x, y) = \sqrt{MSE(x, y)} \quad (4.3)$$

$$e_R(x, y) = \frac{RMSE(x, y)}{\max y - \min y} \quad (4.4)$$

The term  $f(*, \cdot)$  was used to denote that the first argument of any function  $f$  was some reference value ( $*$ ), e.g. a GRF component, predicted from unaltered, measured or tracked kinematic trajectories, related to a second, disturbed prediction ( $\cdot$ ). For the sake of simplification, the symbolic arguments  $\rightarrow$  and  $\downarrow$  were used within tables to indicate that the column and row entries, respectively, were used as arguments.

### Hardware and Computation

The pipeline framework core was run on a laptop computer, which then launched and controlled the Quattracker routines and the AMS console applications on a server machine with a 4 GHz processor with 6 cores and 32 GB of RAM. A maximum number of 15 AMS single-threaded console instances, each running independent studies, were started in parallel in order to fully utilize the hardware capacity. In the case of the Quattracker, where the majority of computation time arises from the EKF matrix operations, different tracking tasks were executed sequentially and the parallelization was left to the **Eigen** library.

## 4.2 Results

The results of all substudies are presented in the same order as they are defined above.

### 4.2.1 Functional Tests and GRF Prediction Validation

The pipeline framework was successfully taken into operation, and all core features of the AMS analyses have been tested. Some GUI visualizations of the pipeline framework and the AMS are provided in appendix A.1.

In the exemplary motion data, a ground plane skewness of up to  $2.5^\circ$  was detected and compensated with the global ground correction method. The method had no significant influence on predicted GRFs and GRMs with differences of both  $\delta\bar{r}$  and  $\delta\bar{e}_R \ll 0.01$  for trajectories with and without a correction. The subsequently applied foot marker plane correction, however, considerably simplified and sped up the process of finding suitable initial conditions for the parameter and motion optimization.

For the three exemplary motion sequences, the following mean correlations  $\bar{r}$  and mean relative root squared mean errors  $\bar{e}_R$  between measured (\*) and predicted ground reaction forces and moments were found:

$N = 3$	$F_x$ (ant-pos)	$F_y$ (med-lat)	$F_z$ (ver)	$M_x$ (fro)	$M_y$ (sag)	$M_z$ (tra)
$\bar{r}(*, \rightarrow)$	0.95	0.74	0.99	0.73	0.97	0.78
$\bar{e}_R(*, \rightarrow)$	0.07	0.27	0.05	0.22	0.06	0.18

**Table 4.1:** Validation results of the GRF prediction method.

The vertical and antero-posterior GRFs and the sagittal GRM were predicted very well; however, the vertical component was consistently underestimated. The remaining GRFs and GRMs achieved poorer prediction accuracy, which is likely due to their relatively small magnitudes. In case of the transverse GRM, the weaker correlation might also be a consequence of the hinge joint modeling at the knee. All these results are in close accord with the findings in [Fluit 14] and [Skals 16]. A visual comparison of measured and predicted GRFs and GRMs is shown in figures A.6 and A.7 in the appendix.

The computation time of the AMS inverse kinematics analysis is largely dependent on initial conditions of the motion and parameter optimization, i.e. the initial guesses for kinematic parameters such as segment lengths. Due to the imposed biomechanical hard constraints, the chance of convergence depends also on chosen error tolerances and maximum allowed iterations per step. Generally, it is an semi-autonomous process, requiring some manual adaptations of anthropometric and marker parameters. Therefore, a performance measure is not meaningful in this case. The AMS inverse dynamics analysis including static optimization, instead, can be assumed to converge for anatomically realistic kinematics. On average, an evaluation of 100 frames took 227 seconds on the above mentioned hardware for the AMS full-body model, i.e.  $0.44 \frac{\text{frames}}{\text{s}}$ . The Quattracker yielded a performance of  $14.71 \frac{\text{frames}}{\text{s}}$  on average, when tracking a full-body model extracted from the AMS, composed of 32 segments, each equipped with a virtual IMU.



### 4.2.2 Foot Posture Sensitivity

The resulting statistics of the foot posture sensitivity analysis are summarized in table 4.2 and also visualized with boxplots in figure 4.2. The effects on the GRFs resulting from induced errors of the APF and SEV DoFs were negligible as expected. The correlations with the GRFs predicted from the unaltered reference trajectories were consistently excellent, and the relative root mean square errors were marginal. This implies that the ground contact conditions could effectively handle those disturbances. It was hypothesized that this came at the price of biased CoP estimates, which would find their expression in disturbed GRMs. Although this effect could be observed in the results, the impact on the predicted GRMs was small for moderate APF and SEV errors. For boundary values of the sampled angular space, the resulting disturbances of especially the frontal moment and the transverse moment were obviously marked, whereas the sagittal moment was very robust even against combinations of highest errors.

In order to relate the influence of APF and SEV disturbances on the estimated CoPs, both error magnitudes  $||\theta_{APF}||$  and  $||\theta_{SEV}||$  were each correlated with the mean deviations between CoPs, predicted through disturbed versus undisturbed trajectories. The CoP deviations were divided into the antero-posterior and medio-lateral directions and the results are shown in table 4.4. As to be expected, the influence of the  $||\theta_{APF}||$  on the antero-posterior component and that of  $||\theta_{SEV}||$  on the medio-lateral component were significant, which is due to the approximately perpendicular alignment of these joint axes with the x and y-axis, respectively. Similarly, the influences of  $||\theta_{APF}||$  and  $||\theta_{SEV}||$  on the previously computed correlations  $r$  and the relative root mean square errors  $e_R$  for the GRFs and GRMs themselves were tested by correlation and are shown in table 4.3

In summary, it was concluded that only kinematic errors at the DoFs of the feet, which disturbed the foot posture during touchdown, did not significantly influence the predicted ground reaction forces and moments. Note, that the observed higher disturbances of the frontal and transverse moments are of minor importance overall, when considering their relatively small magnitudes compared to the sagittal moment, which was also the reason, why they yielded poorer predictions compared to measurements in the first place. For this reason, the further I2S calibration error analysis results were expected to be only marginally affected by suchlike ground contact posture effects.

	$F_x$ (ant-pos)	$F_y$ (med-lat)	$F_z$ (ver)	$M_x$ (fro)	$M_y$ (sag)	$M_z$ (tra)
$\bar{r}(*, \rightarrow)$	0.99	0.99	0.99	0.86	0.99	0.98
$\tilde{r}(*, \rightarrow)$	0.99	0.99	0.99	0.92	0.99	0.99
$\check{r}(*, \rightarrow)$	0.98	0.97	0.99	0.18	0.98	0.78
$s_r(*, \rightarrow)$	0.0018	0.0054	0.0002	0.166	0.0032	0.0334
$\bar{e}_R(*, \rightarrow)$	0.0066	0.0352	0.0054	0.1343	0.0179	0.0653
$\tilde{e}_R(*, \rightarrow)$	0.0051	0.0341	0.0050	0.1383	0.0159	0.0543
$\hat{e}_R(*, \rightarrow)$	0.0432	0.1036	0.0215	0.2435	0.0794	0.2456
$s_{e_R}(*, \rightarrow)$	0.0059	0.0203	0.0031	0.0616	0.0134	0.0488

**Table 4.2:** Statistics of the correlations and relative root mean squared errors for the foot posture sensitivity analysis results.

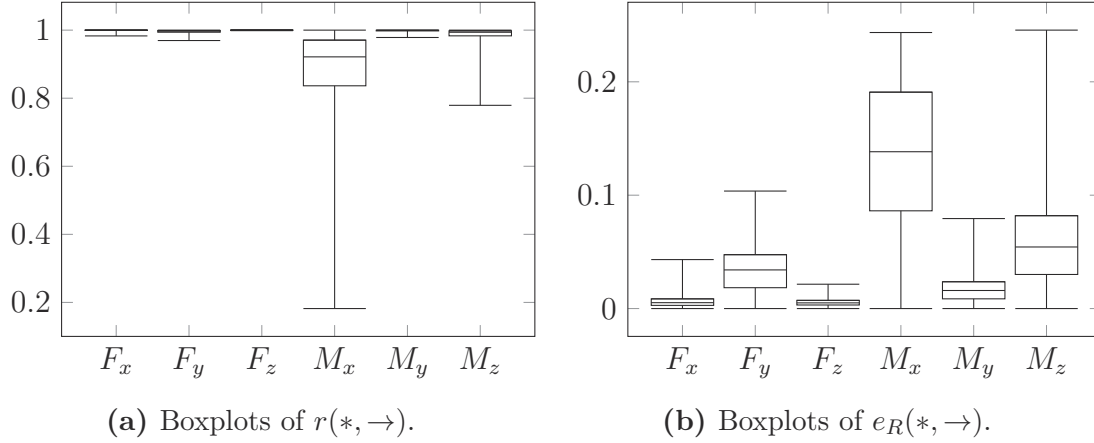


**Figure 4.2:** Boxplots of the correlations and relative root mean squared errors for the foot posture sensitivity analysis results.

	$F_x$ (ant-pos)	$F_y$ (med-lat)	$F_z$ (ver)	$M_x$ (fro)	$M_y$ (sag)	$M_z$ (tra)
$r(  \theta_{APF}  , r^{\rightarrow})$	-0.42	-0.28	-0.65	-0.12	-0.53	-0.21
$r(  \theta_{APF}  , e_R^{\rightarrow})$	0.69	0.17	0.82	0.13	0.61	0.14
$r(  \theta_{SEV}  , r^{\rightarrow})$	-0.18	-0.59	-0.24	-0.54	-0.20	-0.39
$r(  \theta_{SEV}  , e_R^{\rightarrow})$	0.22	0.77	0.30	0.70	0.36	0.59

**Table 4.3:** Correlations of disturbance magnitudes  $||\theta_{APF}||$  and  $||\theta_{SEV}||$  with  $r$  and  $e_R$  for all GRFs and GRMs.

$r(\downarrow, \rightarrow)$	$\delta[\text{CoP}]_{\bar{x}}$ (ant-pos)	$\delta[\text{CoP}]_{\bar{y}}$ (med-lat)
$  \theta_{APF}  $	0.82	0.27
$  \theta_{SEV}  $	0.23	0.69

**Table 4.4:** Correlations of disturbance magnitudes  $||\theta_{APF}||$  and  $||\theta_{SEV}||$  with CoP mean deviations.

### 4.2.3 I2S Calibration Errors

No significant differences between the GRFs and GRMs predicted with optical marker-based trajectories and tracked trajectories using the Quattracker were observed ( $\delta r \ll 0.01$  and  $\delta e_R \ll 0.01$ ). For this reason, the results obtained from the tracked kinematics were used as the reference data (\*).

The statistics of I2S calibration error results for the anterior initial configuration are summarized in table 4.5 and shown in the boxplots in figure 4.3. The predictions GRF and GRM predictions based on disturbed trajectories within the entire angular error range were consistently very close to the undisturbed reference data. The thigh constituted an exception, where the minimum correlation for the medio-lateral GRF was only  $-0.03$ . Also the stability of the frontal and transverse moments against I2S calibration errors was weak for this segment, which might, however, be acceptable due to their relatively small magnitudes. Furthermore, the results of the lateral configuration are summarized in



table 4.6 and shown in the boxplots in figure 4.4. In this configuration, the predictions were again close to the reference data, whereas the shank and foot segments showed distinctly weaker minimum correlations of 0.59 and 0.55, respectively, compared to the other segments, especially in the medio-lateral GRF component, but as well in the frontal and transverse GRMs.

Whereas the thigh in the anterior configuration was quite sensitive against I2S calibration errors, it was considerably more stable in the lateral configuration. A possible explanation could be that in the anterior configuration higher errors on the lateral axis induced wrong adductions and abductions at the hip joint, whereas the same errors in a lateral configuration caused wrong flexions and extensions, which were probably better handled by the GRF prediction. Note, that errors at the thigh segment are generally critical since the spherical hip joint is unconstrained, and angular errors induced at this place might propagate to lower segments, where they cause considerable translational disturbances at the end of the chain. In contrast, the shank and foot were markedly more sensitive to errors in the lateral configuration. This effect might be simply explained by the fact that in this case, the lateral error axis is approximately collinear with the knee and ankle joint axes, so that any lateral errors could not be compensated by joint constraints and were directly passed to the kinematics.

Essentially, the influences of errors on the lateral axis  $\theta_{lat}$  were in each case considerably higher than those on the segment axis  $\theta_{seg}$ , which can be clearly seen in tables 4.7 and 4.8, where the magnitudes of the axes errors have been individually correlated with both  $r$  and  $e_R$  for each segment and each GRF and GRM component. The effect can also be observed in the qualitative error distribution plots in appendix A.4. The reason for that might be that segment axis errors on any segment, except for the foot, primarily disturb the internal and external rotation of the leg during ground contact. In case of the foot, segment axis errors cause basically disturbances in the subtalar eversion, which is to some extent relevant for the GRF prediction. Errors on the lateral axis, however, cause deviations of the kinematics of the leg in either the frontal plane, the sagittal plane or both, depending on the amount of the error and the initial IMU configuration. This is likely more critical in view of the ground contact conditions of the GRF prediction method. Finally, the results for the pelvis were almost identical for both initial configurations, which was expected because they were actually the same for this segment. Marginal deviations, however, appeared from the different overall tracking behavior of the remaining segments for the two configurations.

**Statistics of I2S Calibration Errors with Anterior Initial IMU Configuration**

<b>Pelvis</b>	$F_x$ (ant-pos)	$F_y$ (med-lat)	$F_z$ (ver)	$M_x$ (fro)	$M_y$ (sag)	$M_z$ (tra)
$\bar{r}(*, \rightarrow)$	0.92	0.92	0.97	0.83	0.91	0.90
$\tilde{r}(*, \rightarrow)$	0.98	0.93	0.98	0.87	0.96	0.92
$\check{r}(*, \rightarrow)$	0.76	0.78	0.90	0.41	0.77	0.72
$s_r(*, \rightarrow)$	0.0869	0.0689	0.0309	0.1449	0.0806	0.0935
$\bar{e}_R(*, \rightarrow)$	0.0721	0.0714	0.0715	0.1205	0.1157	0.0841
$\tilde{e}_R(*, \rightarrow)$	0.0422	0.0781	0.0713	0.1274	0.0915	0.0879
$\hat{e}_R(*, \rightarrow)$	0.1804	0.1284	0.1713	0.2146	0.2461	0.1546
$s_{e_R}(*, \rightarrow)$	0.0614	0.0371	0.0527	0.0522	0.0749	0.0412
<b>Thigh</b>						
$\bar{r}(*, \rightarrow)$	0.98	0.74	0.98	0.39	0.93	0.61
$\tilde{r}(*, \rightarrow)$	0.99	0.85	0.99	0.39	0.93	0.69
$\check{r}(*, \rightarrow)$	0.95	-0.03	0.93	-0.12	0.78	-0.07
$s_r(*, \rightarrow)$	0.0123	0.2905	0.0200	0.2662	0.0542	0.2944
$\bar{e}_R(*, \rightarrow)$	0.0446	0.2108	0.0723	0.3314	0.1099	0.1670
$\tilde{e}_R(*, \rightarrow)$	0.0392	0.2189	0.0626	0.3282	0.1157	0.1665
$\hat{e}_R(*, \rightarrow)$	0.1137	0.4643	0.1511	0.5319	0.2558	0.3010
$s_{e_R}(*, \rightarrow)$	0.0278	0.1146	0.0414	0.1211	0.0602	0.0617
<b>Shank</b>						
$\bar{r}(*, \rightarrow)$	0.99	0.97	0.99	0.94	0.98	0.97
$\tilde{r}(*, \rightarrow)$	0.99	0.98	0.99	0.95	0.99	0.98
$\check{r}(*, \rightarrow)$	0.98	0.86	0.99	0.78	0.93	0.81
$s_r(*, \rightarrow)$	0.0065	0.0289	0.0022	0.0514	0.0168	0.0374
$\bar{e}_R(*, \rightarrow)$	0.0239	0.0436	0.0176	0.0675	0.0489	0.0480
$\tilde{e}_R(*, \rightarrow)$	0.0232	0.0436	0.0131	0.0672	0.0475	0.0464
$\hat{e}_R(*, \rightarrow)$	0.0529	0.0985	0.0584	0.1465	0.1142	0.1128
$s_{e_R}(*, \rightarrow)$	0.0136	0.0251	0.0137	0.0354	0.0259	0.0265
<b>Foot</b>						
$\bar{r}(*, \rightarrow)$	0.99	0.98	0.99	0.90	0.99	0.97
$\tilde{r}(*, \rightarrow)$	0.99	0.99	0.99	0.92	0.99	0.98
$\check{r}(*, \rightarrow)$	0.98	0.93	0.99	0.66	0.96	0.81
$s_r(*, \rightarrow)$	0.0052	0.0175	0.0008	0.0790	0.0083	0.0317
$\bar{e}_R(*, \rightarrow)$	0.0193	0.0402	0.0136	0.0950	0.0316	0.0557
$\tilde{e}_R(*, \rightarrow)$	0.0178	0.0361	0.0135	0.0909	0.0299	0.0506
$\hat{e}_R(*, \rightarrow)$	0.0380	0.0932	0.0373	0.1916	0.0840	0.1697
$s_{e_R}(*, \rightarrow)$	0.0109	0.0209	0.0079	0.0419	0.0180	0.0308

**Table 4.5:** Statistics of the I2S calibration errors with an anterior initial IMU configuration.

## Statistics of I2S Calibration Errors with Lateral Initial IMU Configuration

<b>Pelvis</b>	$F_x$ (ant-pos)	$F_y$ (med-lat)	$F_z$ (ver)	$M_x$ (fro)	$M_y$ (sag)	$M_z$ (tra)
$\bar{r}(*, \rightarrow)$	0.92	0.92	0.97	0.83	0.91	0.89
$\tilde{r}(*, \rightarrow)$	0.98	0.93	0.98	0.86	0.95	0.91
$\check{r}(*, \rightarrow)$	0.75	0.77	0.90	0.43	0.77	0.70
$s_r(*, \rightarrow)$	0.0900	0.0721	0.0312	0.1445	0.0823	0.1001
$\bar{e}_R(*, \rightarrow)$	0.0731	0.0731	0.0722	0.1200	0.1179	0.0859
$\tilde{e}_R(*, \rightarrow)$	0.0435	0.0794	0.0703	0.1255	0.0943	0.0900
$\hat{e}_R(*, \rightarrow)$	0.1812	0.1302	0.1701	0.2134	0.2551	0.1641
$s_{e_R}(*, \rightarrow)$	0.0626	0.0389	0.0534	0.0516	0.0762	0.0442
<b>Thigh</b>						
$\bar{r}(*, \rightarrow)$	0.97	0.94	0.98	0.64	0.93	0.82
$\tilde{r}(*, \rightarrow)$	0.99	0.95	0.99	0.68	0.96	0.85
$\check{r}(*, \rightarrow)$	0.85	0.77	0.90	0.09	0.76	0.44
$s_r(*, \rightarrow)$	0.0404	0.0580	0.0264	0.2129	0.0671	0.1326
$\bar{e}_R(*, \rightarrow)$	0.0351	0.0708	0.0523	0.2140	0.1073	0.1341
$\tilde{e}_R(*, \rightarrow)$	0.0248	0.0697	0.0382	0.2111	0.0957	0.1332
$\hat{e}_R(*, \rightarrow)$	0.1036	0.1391	0.1716	0.4230	0.2497	0.2940
$s_{e_R}(*, \rightarrow)$	0.0267	0.0315	0.0440	0.0854	0.0624	0.0557
<b>Shank</b>						
$\bar{r}(*, \rightarrow)$	0.94	0.87	0.99	0.74	0.87	0.82
$\tilde{r}(*, \rightarrow)$	0.98	0.91	0.99	0.77	0.90	0.83
$\check{r}(*, \rightarrow)$	0.77	0.59	0.94	0.20	0.43	0.59
$s_r(*, \rightarrow)$	0.0741	0.1220	0.0204	0.2109	0.1413	0.1275
$\bar{e}_R(*, \rightarrow)$	0.0579	0.0946	0.0485	0.1305	0.1804	0.1123
$\tilde{e}_R(*, \rightarrow)$	0.0417	0.0840	0.0332	0.1285	0.1547	0.1197
$\hat{e}_R(*, \rightarrow)$	0.1488	0.1986	0.1291	0.2622	0.5573	0.2441
$s_{e_R}(*, \rightarrow)$	0.0482	0.0549	0.0403	0.0625	0.1382	0.0557
<b>Foot</b>						
$\bar{r}(*, \rightarrow)$	0.96	0.90	0.99	0.82	0.96	0.92
$\tilde{r}(*, \rightarrow)$	0.97	0.98	0.99	0.90	0.98	0.95
$\check{r}(*, \rightarrow)$	0.82	0.55	0.97	0.42	0.83	0.68
$s_r(*, \rightarrow)$	0.0470	0.1311	0.0092	0.1638	0.0424	0.0699
$\bar{e}_R(*, \rightarrow)$	0.0623	0.0733	0.0424	0.1041	0.0835	0.0696
$\tilde{e}_R(*, \rightarrow)$	0.0492	0.0448	0.0355	0.1001	0.0642	0.0656
$\hat{e}_R(*, \rightarrow)$	0.1534	0.1965	0.0992	0.2198	0.2471	0.1313
$s_{e_R}(*, \rightarrow)$	0.0403	0.0538	0.0264	0.0469	0.0591	0.0253

**Table 4.6:** Statistics of the I2S calibration errors with a lateral initial IMU configuration.

### Boxplots of I2S Calibration Errors with Anterior Initial IMU Configuration

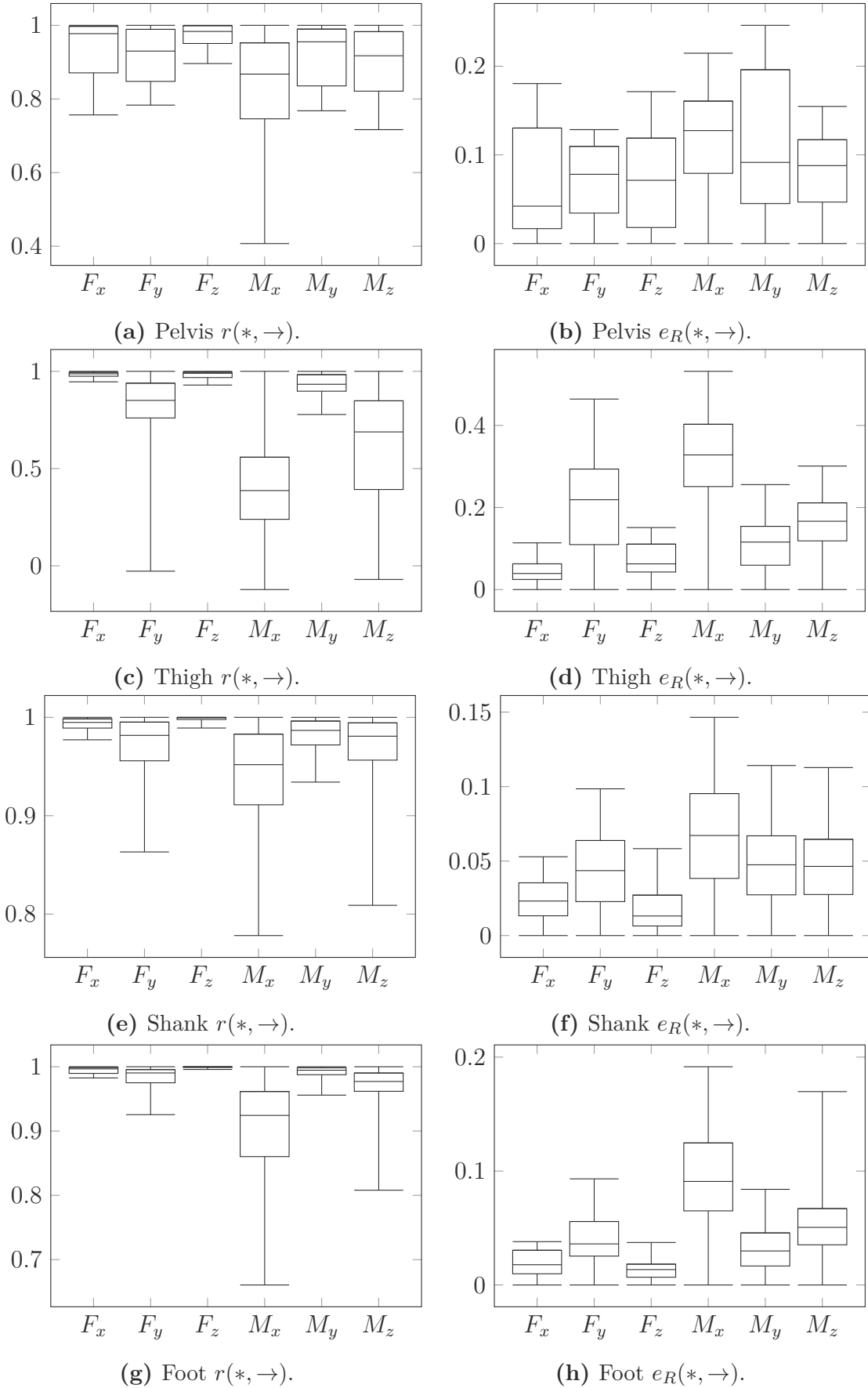


**Figure 4.3:** I2S calibration error boxplots with an anterior initial IMU configuration.

### Boxplots of I2S Calibration Errors with Lateral Initial IMU Configuration

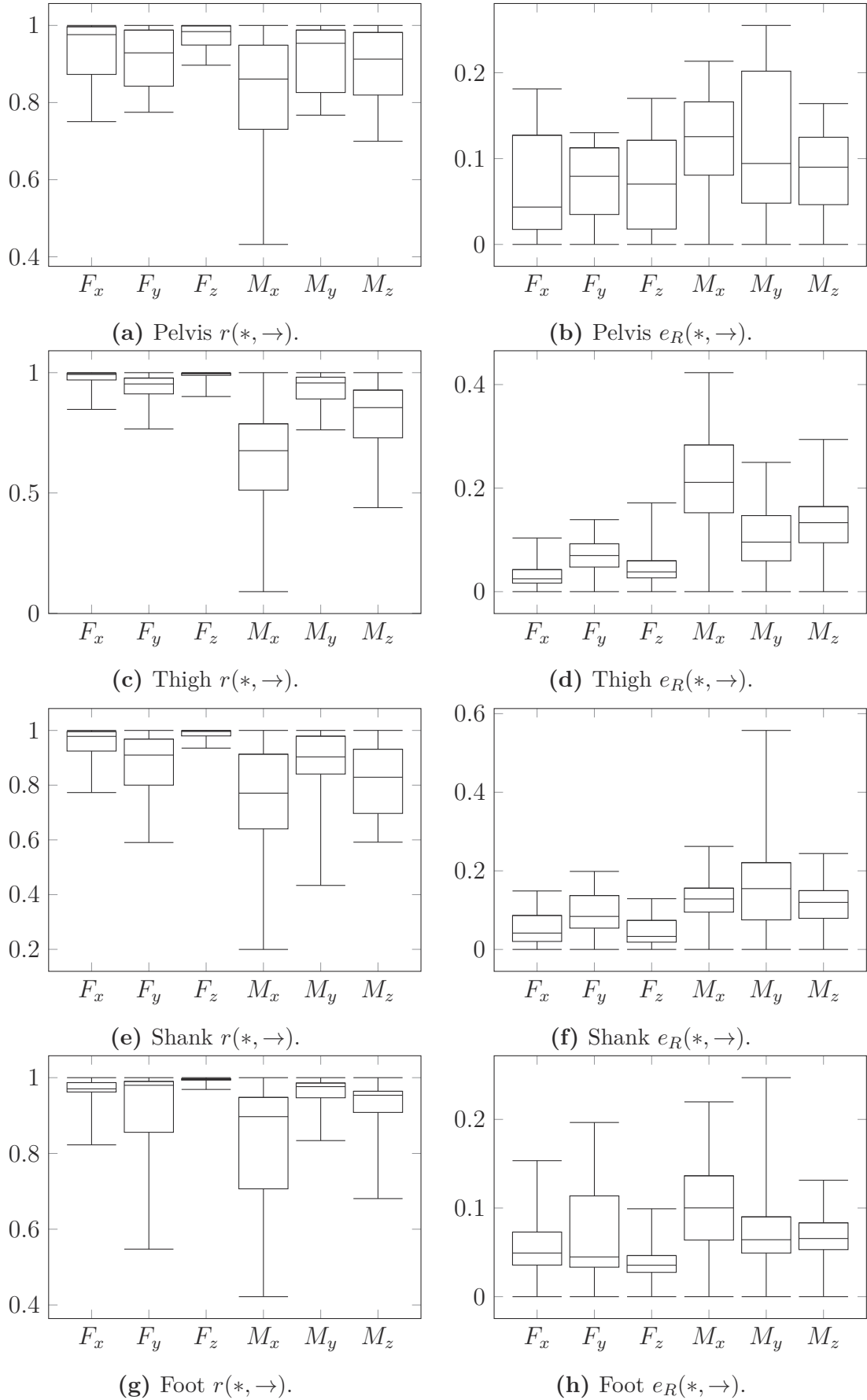


**Figure 4.4:** I2S calibration error boxplots with a lateral initial IMU configuration.

## Influences of the Segmental and Lateral Axes Disturbance Magnitudes

<b>Pelvis</b>	$F_x$ (ant-pos)	$F_y$ (med-lat)	$F_z$ (ver)	$M_x$ (fro)	$M_y$ (sag)	$M_z$ (tra)
$r(  \theta_{seg}  , r^{\rightarrow})$	-0.01	-0.02	-0.01	-0.03	-0.03	-0.03
$r(  \theta_{seg}  , e_R^{\rightarrow})$	0.01	0.06	0.01	0.07	0.06	0.08
$r(  \theta_{lat}  , r^{\rightarrow})$	-0.76	-0.95	-0.90	-0.88	-0.79	-0.91
$r(  \theta_{lat}  , e_R^{\rightarrow})$	0.75	0.97	0.97	0.87	0.77	0.97
<b>Thigh</b>						
$r(  \theta_{seg}  , r^{\rightarrow})$	-0.10	-0.02	0.00	-0.07	-0.05	-0.07
$r(  \theta_{seg}  , e_R^{\rightarrow})$	0.07	0.06	0.02	-0.03	0.08	0.15
$r(  \theta_{lat}  , r^{\rightarrow})$	-0.93	-0.70	-0.86	-0.85	-0.88	-0.57
$r(  \theta_{lat}  , e_R^{\rightarrow})$	0.77	0.93	0.95	0.75	0.91	0.66
<b>Shank</b>						
$r(  \theta_{seg}  , r^{\rightarrow})$	-0.03	-0.05	-0.01	-0.08	-0.04	-0.06
$r(  \theta_{seg}  , e_R^{\rightarrow})$	0.02	0.00	0.03	0.03	0.09	0.06
$r(  \theta_{lat}  , r^{\rightarrow})$	-0.90	-0.80	-0.71	-0.84	-0.89	-0.72
$r(  \theta_{lat}  , e_R^{\rightarrow})$	0.97	0.91	0.88	0.91	0.93	0.89
<b>Foot</b>						
$r(  \theta_{seg}  , r^{\rightarrow})$	-0.72	-0.68	-0.67	-0.54	-0.59	-0.42
$r(  \theta_{seg}  , e_R^{\rightarrow})$	0.75	0.70	0.73	0.45	0.67	0.46
$r(  \theta_{lat}  , r^{\rightarrow})$	-0.28	-0.26	-0.37	-0.44	-0.38	-0.43
$r(  \theta_{lat}  , e_R^{\rightarrow})$	0.35	0.42	0.43	0.52	0.44	0.44

**Table 4.7:** Correlations of the segmental axis and lateral axis disturbance magnitudes  $||\theta_{seg}||$  and  $||\theta_{lat}||$  with  $r$  and  $e_R$  for all GRFs and GRMs with an anterior initial IMU configuration.

<b>Pelvis</b>	$F_x$ (ant-pos)	$F_y$ (med-lat)	$F_z$ (ver)	$M_x$ (fro)	$M_y$ (sag)	$M_z$ (tra)
$r(  \theta_{seg}  , r^{\rightarrow})$	0.00	-0.02	0.00	-0.03	-0.03	-0.03
$r(  \theta_{seg}  , e_R^{\rightarrow})$	0.01	0.06	0.01	0.08	0.07	0.09
$r(  \theta_{lat}  , r^{\rightarrow})$	-0.76	-0.94	-0.90	-0.89	-0.82	-0.90
$r(  \theta_{lat}  , e_R^{\rightarrow})$	0.75	0.96	0.97	0.89	0.78	0.96
<b>Thigh</b>						
$r(  \theta_{seg}  , r^{\rightarrow})$	-0.01	-0.13	0.00	-0.31	-0.06	-0.43
$r(  \theta_{seg}  , e_R^{\rightarrow})$	0.04	0.20	0.03	0.44	0.08	0.45
$r(  \theta_{lat}  , r^{\rightarrow})$	-0.70	-0.81	-0.62	-0.71	-0.89	-0.69
$r(  \theta_{lat}  , e_R^{\rightarrow})$	0.83	0.92	0.76	0.56	0.95	0.67
<b>Shank</b>						
$r(  \theta_{seg}  , r^{\rightarrow})$	0.01	0.01	0.01	0.00	-0.01	-0.01
$r(  \theta_{seg}  , e_R^{\rightarrow})$	-0.01	-0.01	0.00	0.01	0.02	0.03
$r(  \theta_{lat}  , r^{\rightarrow})$	-0.63	-0.78	-0.64	-0.80	-0.76	-0.98
$r(  \theta_{lat}  , e_R^{\rightarrow})$	0.72	0.81	0.76	0.87	0.82	0.93
<b>Foot</b>						
$r(  \theta_{seg}  , r^{\rightarrow})$	0.00	-0.03	0.01	-0.13	-0.02	-0.09
$r(  \theta_{seg}  , e_R^{\rightarrow})$	-0.02	0.09	0.01	0.32	0.01	0.15
$r(  \theta_{lat}  , r^{\rightarrow})$	-0.67	-0.54	-0.68	-0.50	-0.60	-0.61
$r(  \theta_{lat}  , e_R^{\rightarrow})$	0.68	0.53	0.73	0.38	0.65	0.57

**Table 4.8:** Correlations of the segmental axis and lateral axis disturbance magnitudes  $||\theta_{seg}||$  and  $||\theta_{lat}||$  with  $r$  and  $e_R$  for all GRFs and GRMs with a lateral initial IMU configuration.

#### 4.2.4 Typical I2S Calibration Error Scenario

In order to assess the effectiveness of the Quattracker's kinematic constraints, the sample of typical I2S errors was firstly tracked without any joint constraints, allowing for 3 DoFs between incident segments. However, 11 out of 100 tracked tests could not be processed by the AMS due to their unrealistic kinematic trajectories, and the dynamic solutions of the remaining ones were not further investigated. Tracked with the fully constrained skeleton instead, all resulting kinematic solutions caused the inverse dynamics routine to successfully converge. The typical error scenario showed obvious effects of accumulated I2S segment errors, which in their entirety notably lowered the GRF prediction accuracy.

The correlations and relative root mean square errors between GRFs and GRMs predicted based on disturbed versus undisturbed kinematics were averaged for the left and right leg, and the resulting statistics are shown in table 4.9 and in the boxplots in figure 4.6. Even the antero-posterior and vertical forces, which were consistently well predicted in the systematical error tests, showed very low minimum correlations. These values originated from unfavorable combinations of high lateral axis errors at several segments. In contrast, the median results were affected by only moderate to minor declines, especially for the forces and moments of higher magnitudes. The individual and total muscle activation correlations were relatively high in consideration of the GRF and GRM prediction quality with an average weighted, total activation correlation of 0.70. The detailed correlations of activations  $a$  are shown in table 4.11, where the muscles are ranked according to their relative maximum strength  $w$  in respect of the total leg strength. Activation correlations for the same muscles at left and right leg were averaged.

#### Reduced Error Range

Since the accumulation of I2S calibration errors in the entire sampling range led to results with quite high deviations to the reference data, the same test was repeated for an error range of  $\pm 6^\circ$  and yielded considerably better results with very good mean and median predictions of the three GRFs and the sagittal GRM. The minimum values were obviously more preferable to those of the previous scenario, and all standard deviations were markedly smaller. Table 4.10 and figure 4.5 show the statistics and boxplots for this setup. Overall, also the muscle activations achieved notably higher correlations with a weighted, total activation correlation of 0.86. The detailed activation correlations per muscle are shown in table 4.12.

$N = 100$	$F_x$ (ant-pos)	$F_y$ (med-lat)	$F_z$ (ver)	$M_x$ (fro)	$M_y$ (sag)	$M_z$ (tra)
$\bar{r}(*, \rightarrow)$	0.90	0.71	0.96	0.35	0.84	0.57
$\tilde{r}(*, \rightarrow)$	0.94	0.78	0.96	0.35	0.85	0.63
$\check{r}(*, \rightarrow)$	0.70	-0.11	0.77	-0.16	0.52	-0.36
$s_r(*, \rightarrow)$	0.0896	0.2243	0.0406	0.2153	0.0957	0.2438
$\bar{e}_R(*, \rightarrow)$	0.0898	0.2171	0.1097	0.3233	0.1914	0.1778
$\tilde{e}_R(*, \rightarrow)$	0.0670	0.2208	0.1072	0.2931	0.1678	0.1784
$\hat{e}_R(*, \rightarrow)$	0.1950	0.4520	0.2558	0.7591	0.4767	0.3081
$s_{e_R}(*, \rightarrow)$	0.0503	0.0909	0.0457	0.1194	0.1003	0.0527

**Table 4.9:** Statistics of the typical I2S calibration error scenario with an error range of  $\pm 12^\circ$ .

$N = 100$	$F_x$ (ant-pos)	$F_y$ (med-lat)	$F_z$ (ver)	$M_x$ (fro)	$M_y$ (sag)	$M_z$ (tra)
$\bar{r}(*, \rightarrow)$	0.97	0.91	0.99	0.60	0.94	0.78
$\tilde{r}(*, \rightarrow)$	0.99	0.91	0.99	0.58	0.96	0.81
$\check{r}(*, \rightarrow)$	0.82	0.76	0.97	0.29	0.70	0.37
$s_r(*, \rightarrow)$	0.0431	0.0552	0.0071	0.1758	0.0557	0.1568
$\bar{e}_R(*, \rightarrow)$	0.0516	0.1297	0.0555	0.2558	0.1061	0.1296
$\tilde{e}_R(*, \rightarrow)$	0.0365	0.1258	0.0556	0.2608	0.0912	0.1289
$\hat{e}_R(*, \rightarrow)$	0.1544	0.2486	0.1043	0.4977	0.3501	0.2480
$s_{e_R}(*, \rightarrow)$	0.0359	0.0586	0.0206	0.1034	0.0624	0.0411

**Table 4.10:** Statistics of the typical I2S calibration error scenario with an error range of  $\pm 6^\circ$ .

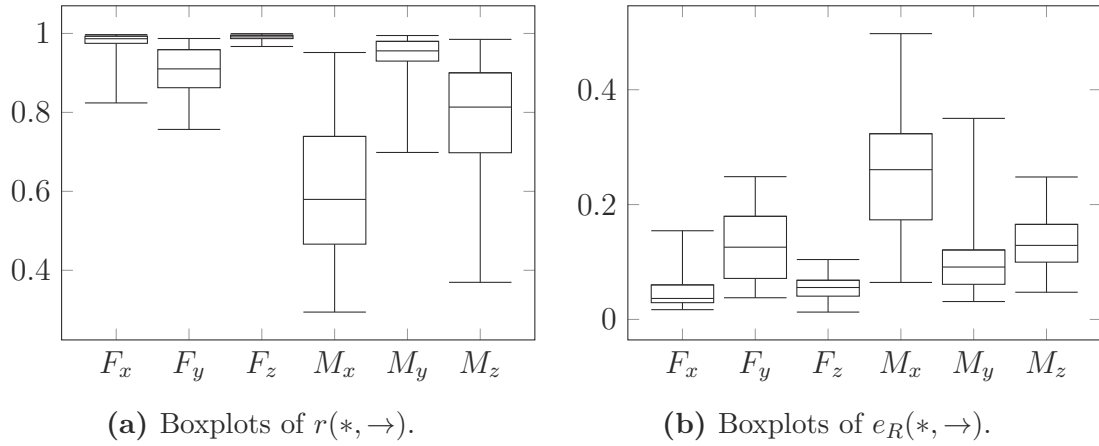


**Figure 4.5:** Boxplots of the correlations and relative root mean squared errors for the typical I2S calibration error scenario with an error range of  $\pm 6^\circ$ .

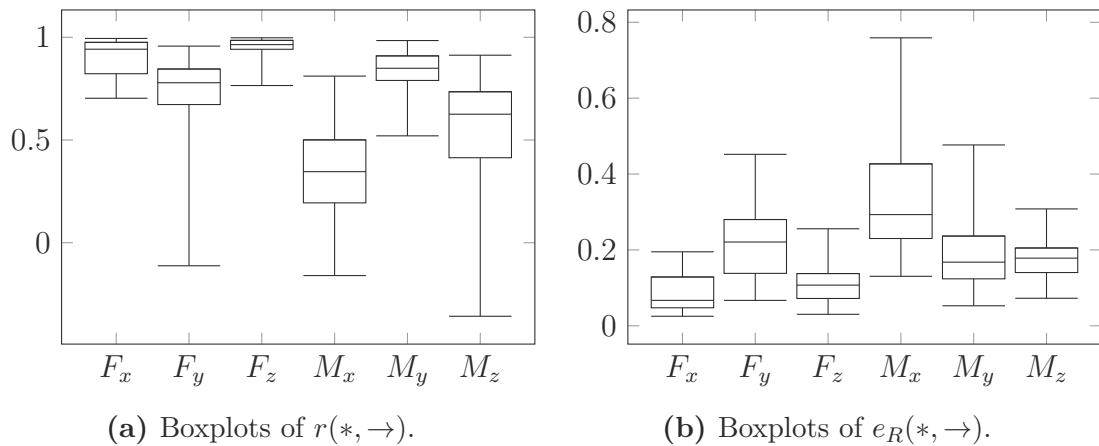


**Figure 4.6:** Boxplots of the correlations and relative root mean squared errors for the typical I2S calibration error scenario with an error range of  $\pm 12^\circ$ .



Muscle	$w(\downarrow)$	$\bar{r}(*, a^\downarrow)$	$\tilde{r}(*, a^\downarrow)$	$\check{r}(*, a^\downarrow)$	$s_r(*, a^\downarrow)$
GastrocnemiusMedialis	0.0830	0.78	0.78	0.55	0.0897
VastusLateralisSuperior	0.0618	0.78	0.78	0.49	0.1108
SoleusMedialis	0.0596	0.86	0.86	0.68	0.0661
BicepsFemorisCaputLongum	0.0570	0.81	0.82	0.41	0.0912
SoleusLateralis	0.0543	0.80	0.81	0.61	0.0802
GastrocnemiusLateralis	0.0454	0.80	0.81	0.59	0.0778
Semimembranosus	0.0358	0.68	0.69	0.26	0.1087
Semitendinosus	0.0308	0.65	0.66	0.26	0.1238
RectusFemoris	0.0302	0.78	0.81	0.45	0.1177
GluteusMediusPosterior	0.0265	0.77	0.86	0.14	0.2117
GluteusMinimusAnterior	0.0260	0.72	0.76	-0.09	0.2093
VastusMedialisMid	0.0243	0.78	0.78	0.49	0.1113
ObturatorInternus	0.0221	0.59	0.59	-0.10	0.2283
ObturatorExternusSuperior	0.0214	0.47	0.47	0.13	0.1595
GluteusMinimusMid	0.0213	0.72	0.78	-0.16	0.2430
Piriformis	0.0211	0.69	0.76	-0.10	0.2268
FlexorHallucisLongus	0.0196	0.47	0.47	0.16	0.1368
GluteusMinimusPosterior	0.0194	0.71	0.77	-0.18	0.2483
AdductorMagnusDistal	0.0185	0.48	0.47	0.18	0.1563
GluteusMaximusSuperior	0.0173	0.44	0.45	-0.02	0.1658
TibialisAnterior	0.0168	0.16	0.17	-0.24	0.1877
GluteusMediusAnterior	0.0165	0.82	0.84	0.45	0.1072
PeroneusLongus	0.0151	0.46	0.50	-0.10	0.1985
TibialisPosteriorLateralis	0.0137	0.53	0.52	0.19	0.1361
TibialisPosteriorMedialis	0.0137	0.53	0.53	0.20	0.1342
VastusIntermedius	0.0133	0.78	0.78	0.49	0.1109
SartoriusDistal	0.0124	0.66	0.67	0.43	0.1158
SartoriusProximal	0.0124	0.72	0.72	0.52	0.0954
PeroneusBrevis	0.0120	0.48	0.52	-0.09	0.1929
IliacusMid	0.0113	0.74	0.73	0.53	0.0933
GemellusInferior	0.0108	0.52	0.55	-0.09	0.2064
GemellusSuperior	0.0108	0.66	0.72	-0.13	0.2339
VastusMedialisInferior	0.0102	0.78	0.78	0.48	0.1117
Poplitues	0.0101	0.77	0.79	0.44	0.1181
QuadratusFemoris	0.0096	0.49	0.50	0.21	0.1235
VastusMedialisSuperior	0.0094	0.78	0.78	0.49	0.1110
TensorFasciaeLatae	0.0092	0.77	0.79	0.52	0.0930
BicepsFemorisCaputBreve	0.0082	0.57	0.57	0.22	0.1380
GluteusMaximusInferior	0.0079	0.76	0.80	0.19	0.1347
AdductorMagnusMid	0.0077	0.47	0.48	0.10	0.1877
ObturatorExternusInferior	0.0072	0.64	0.63	0.31	0.1318
IliacusMedialis	0.0066	0.74	0.73	0.53	0.0933
IliacusLateralis	0.0057	0.74	0.73	0.53	0.0933
AdductorLongus	0.0053	0.70	0.70	0.46	0.1085
Gracilis	0.0051	0.53	0.52	0.21	0.1608
AdductorBrevisProximal	0.0050	0.70	0.70	0.43	0.1135
AdductorBrevisMid	0.0046	0.70	0.70	0.41	0.1153
Plantaris	0.0045	0.80	0.81	0.62	0.0776
AdductorBrevisDistal	0.0042	0.70	0.70	0.37	0.1212
FlexorDigitorumLongus	0.0042	0.42	0.43	0.06	0.1534
PeroneusTertius	0.0039	0.40	0.42	-0.12	0.1856
ExtensorHallucisLongus	0.0038	0.57	0.56	0.20	0.1464
VastusLateralisInferior	0.0037	0.78	0.78	0.49	0.1113
Pectineus	0.0036	0.70	0.70	0.47	0.1065
ExtensorDigitorumLongus	0.0034	0.51	0.51	0.16	0.1256
AdductorMagnusProximal	0.0026	0.57	0.57	0.10	0.1710
Weighted Sum	$\sum w$	0.70	0.70	0.52	0.0882

**Table 4.11:** Individual and total muscle activations for the typical I2S calibration error scenario with an error range of  $\pm 12^\circ$ .

Muscle	$w(\downarrow)$	$\bar{r}(*, a^\downarrow)$	$\tilde{r}(*, a^\downarrow)$	$\check{r}(*, a^\downarrow)$	$s_r(*, a^\downarrow)$
GastrocnemiusMedialis	0.0830	0.90	0.91	0.72	0.0575
VastusLateralisSuperior	0.0618	0.93	0.94	0.79	0.0449
SoleusMedialis	0.0596	0.93	0.94	0.82	0.0422
BicepsFemorisCaputLongum	0.0570	0.93	0.93	0.81	0.0410
SoleusLateralis	0.0543	0.92	0.92	0.78	0.0440
GastrocnemiusLateralis	0.0454	0.92	0.93	0.76	0.0468
Semimembranosus	0.0358	0.85	0.85	0.64	0.0704
Semitendinosus	0.0308	0.83	0.83	0.53	0.0812
RectusFemoris	0.0302	0.91	0.91	0.62	0.0537
GluteusMediusPosterior	0.0265	0.95	0.96	0.82	0.0350
GluteusMinimusAnterior	0.0260	0.92	0.93	0.80	0.0479
VastusMedialisMid	0.0243	0.93	0.94	0.79	0.0449
ObturatorInternus	0.0221	0.84	0.87	0.54	0.1052
ObturatorExternusSuperior	0.0214	0.72	0.73	0.41	0.1352
GluteusMinimusMid	0.0213	0.92	0.93	0.66	0.0531
Piriformis	0.0211	0.91	0.93	0.66	0.0683
FlexorHallucisLongus	0.0196	0.68	0.66	0.44	0.1160
GluteusMinimusPosterior	0.0194	0.92	0.94	0.68	0.0635
AdductorMagnusDistal	0.0185	0.70	0.72	0.34	0.1122
GluteusMaximusSuperior	0.0173	0.70	0.70	0.31	0.1088
TibialisAnterior	0.0168	0.44	0.45	-0.03	0.1937
GluteusMediusAnterior	0.0165	0.94	0.95	0.86	0.0277
PeroneusLongus	0.0151	0.68	0.69	0.30	0.1356
TibialisPosteriorLateralis	0.0137	0.74	0.74	0.50	0.1044
TibialisPosteriorMedialis	0.0137	0.74	0.73	0.50	0.1040
VastusIntermedius	0.0133	0.93	0.94	0.79	0.0449
SartoriusDistal	0.0124	0.83	0.84	0.59	0.0830
SartoriusProximal	0.0124	0.86	0.86	0.67	0.0705
PeroneusBrevis	0.0120	0.70	0.70	0.33	0.1292
IliacusMid	0.0113	0.88	0.88	0.65	0.0622
GemellusInferior	0.0108	0.75	0.78	0.45	0.1200
GemellusSuperior	0.0108	0.90	0.92	0.65	0.0752
VastusMedialisInferior	0.0102	0.93	0.94	0.79	0.0450
Poplitues	0.0101	0.93	0.94	0.78	0.0448
QuadratusFemoris	0.0096	0.72	0.71	0.43	0.1109
VastusMedialisSuperior	0.0094	0.93	0.94	0.79	0.0449
TensorFasciaeLatae	0.0092	0.89	0.90	0.68	0.0543
BicepsFemorisCaputBreve	0.0082	0.80	0.80	0.54	0.0969
GluteusMaximusInferior	0.0079	0.93	0.94	0.77	0.0413
AdductorMagnusMid	0.0077	0.71	0.73	0.20	0.1345
ObturatorExternusInferior	0.0072	0.84	0.84	0.57	0.1037
IliacusMedialis	0.0066	0.88	0.88	0.65	0.0622
IliacusLateralis	0.0057	0.88	0.88	0.65	0.0623
AdductorLongus	0.0053	0.85	0.86	0.61	0.0746
Gracilis	0.0051	0.77	0.80	0.35	0.1344
AdductorBrevisProximal	0.0050	0.86	0.85	0.61	0.0770
AdductorBrevisMid	0.0046	0.86	0.86	0.65	0.0777
Plantaris	0.0045	0.92	0.93	0.77	0.0463
AdductorBrevisDistal	0.0042	0.87	0.87	0.63	0.0816
FlexorDigitorumLongus	0.0042	0.65	0.63	0.39	0.1207
PeroneusTertius	0.0039	0.64	0.65	0.23	0.1483
ExtensorHallucisLongus	0.0038	0.74	0.76	0.52	0.1096
VastusLateralisInferior	0.0037	0.93	0.94	0.79	0.0449
Pectineus	0.0036	0.85	0.86	0.60	0.0730
ExtensorDigitorumLongus	0.0034	0.67	0.66	0.45	0.1182
AdductorMagnusProximal	0.0026	0.81	0.82	0.33	0.1149
Weighted Sum	$\sum w$	0.86	0.86	0.73	0.0522

**Table 4.12:** Individual and total muscle activations for the typical I2S calibration error scenario with an error range of  $\pm 6^\circ$ .

### 4.2.5 Skeleton Trackability

The trackable lower body skeleton model, fusing the previously two joints at the ankles into one two-axes joint, did not alter the kinematic solution significantly compared to that, tracked with the original model. All angular DoF errors, including particularly the APF and SEV, were below  $0.1^\circ$ , and the resulting deviations of the predicted GRFs and GRMs from the reference data (\*) were marginal ( $\delta r$  and  $\delta e_R \ll 0.01$ ). This implied that the two-axes joint could effectively constrain the kinematics according to the two anatomical joint axes at the ankle. In general, the method might be preferable to a modeling through two incident hinge joints as it is simpler and reduces the total number of skeletal segments, thus decreasing the computational tracking effort. The same applies to the redundant segments at the elbows and wrists in the original AMS skeleton definition.

The simplified full-body version induced some minor but significant errors at the bridged segments of the shoulder and spine regions, where (rounded up) maximum angular errors of  $5^\circ$  and  $3^\circ$  were measured at the sternoclavicular (SC) and acromioclavicular (AC) joints, respectively, which accordingly disturbed the successive segments of the kinematic arm chain. Errors at the spine segments had a maximum magnitude of  $1.5^\circ$ . Note, that only a normal gait sequence has been tested, and these errors are likely higher for movements with higher ranges of motion. For this reason, and from a perspective of methodical consistency, the shoulder and spine rhythm should be directly implemented in the Quattracker or any tracking algorithm. The influences of these kinematic errors on predicted GRFs and GRMs, in this case, were, however, small as shown in table 4.13.

	$F_x$ (ant-pos)	$F_y$ (med-lat)	$F_z$ (ver)	$M_x$ (fro)	$M_y$ (sag)	$M_z$ (tra)
$r(*, \rightarrow)$	0.99	0.97	0.99	0.93	0.98	0.97
$e_R(*, \rightarrow)$	0.0211	0.0614	0.0102	0.1389	0.0857	0.0882

**Table 4.13:** Correlations and relative root mean squared errors of predicted GRFs and GRMs for the simplified full-body trackable skeleton.



## 5. Discussion and Outlook

### 5.1 Conclusion

Within the scope of this thesis, a software framework has been developed, which combines conventional marker-based as well as inertial motion capture with a musculoskeletal analysis pipeline. In contrast to most state of the art approaches for analyses based on inertial tracking, the same musculoskeletal model was used for kinematic and musculoskeletal investigations throughout the pipeline. This constitutes a consistent solution and ensures that no additional modeling errors, e.g. arising from conversion between different skeletons, can influence the biomechanical variables. Techniques to overcome the limitations of a simplified, IMU-trackable skeleton for real data tracking, have been proposed. Moreover, a universal prediction method for ground reaction forces and moments has been integrated, that facilitates the required independence of force plate measurements, inevitable for a flexible and mobile system. The chosen prediction approach presupposes no previously collected empirical data and instead requires only an adequate modeling of the ground, which may be either done in advance for complex environments or implicitly by defining robust ground contact conditions.

The practical part of the thesis consisted of several studies, mainly related to sensor-to-segment calibration errors, but also to directly induced kinematic disturbances. Whereas the former are a direct consequence of any inertial tracking method, and thus a major cause of GRF prediction errors, the latter were only of interest in order to investigate the sensitivity of the ground contact conditions in isolation. In essence, the results can be stated as follows. The tested GRF prediction method proved to be very robust against disturbances of the foot posture during ground contact. This is achieved by a combination of quite liberal height and zero-velocity thresholds, which comes at the price of slightly biased CoP estimates and thus poorer GRM predictions. However, it must be stated, that those components with relatively small magnitudes are generally associated with higher deviations from their measured reference values, whereas the more dominant forces and moments during gait, i.e. the antero-posterior and vertical GRF and the sagittal GRM, are mostly accurately predicted. Basically the same appears to apply when comparing GRFs and GRMs predicted based on disturbed versus reference trajectories. Nevertheless, in case of only foot posture disturbances, the predictions were consistently robust.

The systematically altered sensor-to-segment calibration errors on the lateral axis showed a significantly higher influence on predicted GRFs and GRMs than those on the segmental axis, which can be explained as the latter induce primary distorted leg rotations and rotational errors can be caught by knee and ankle joint constraints, depending on the initial IMU placement at the respective segment. Generally, the pelvis, as the root segment, and the incident thigh tended to cause higher effects than the lower segments of the kinematic chain of the leg. However, this was also dependent on the chosen initial configuration: for the thigh, a lateral initial setup was clearly preferable and for the shank and foot, anterior IMU placements yielded better results. This is understandable since an alignment of rotation error axes and joint axes invalidates any constraining. Overall, the effects of I2S calibration errors at single segments were small to moderate, hence manageable with appropriate initial configurations for each segment.

However, these effects accumulated in a more realistic scenario, where all segments were subject to different I2S calibration errors drawn from the entire range of  $\pm 12^\circ$ , therefore disturbing the GRF predictions markedly. This was likely a consequence of higher error magnitudes at several segments, especially on the lateral axes. The qualitative error distribution plots of the previous, systematic analysis, indicated steep error increases along this dimension. For a reduced, halved error range, instead, the results were appreciably better and tolerable. In this case, also the muscle activation correlations were surprisingly robust on average, even in respect of individual muscles. A further investigation of tolerable error ranges, also considering advantageous initial IMU placements per segment, should be undertaken. For the next steps, real sensor data should be certainly incorporated into the analyses. The implemented pipeline framework provides a convenient toolkit and evaluation environment for this purpose.

## 5.2 Future Work

Based on the work up to now, further follow-up questions emerged in several aspects. Firstly, as mentioned above, the conducted analyses based on simulations must be validated against real sensor data. At the same time, it might be useful to also acquire force plate measurements in order to further validate the GRF prediction method itself and to differentiate between disturbances of muscle activations caused by kinematic deviations versus those arising from wrong GRF predictions. As the analyses so far included only the simulation of errors at lower body segments, full-body I2S calibration errors should be considered furthermore. In this context, the additional influences of disturbed upper body kinematic trajectories on predicted GRFs would be of interest.

As motivated within the theoretical part of this thesis, a direct inertial tracking of the same detailed skeleton models as used for further musculoskeletal analyses, is clearly preferable from a conceptual point of view. However, possible advantages regarding the kinematic precision as well as the prevention of error propagation to biomechanical variables should be evaluated and quantitatively compared against methods based on mapping of different skeletons. An example for a skeleton transformation for inertial tracking, that relies on an alignment of anatomical, bony landmarks, was recently proposed in [AnyBody Tech. 17]. Besides that, the shoulder and spine rhythm should be directly incorporated into the Quattracker or the alternative optimization based tracking approach

presented in [Taetz 16], in order to exploit these biomechanical constraints as part of the kinematic tracking.

As a rather technical requirement, arising from the complexity of a detailed full-body skeleton, the performance of the Quattracker implementation should be optimized. Together with the AMS inverse dynamics analysis routine, this currently constitutes a computational bottleneck for any investigations based on simulated or real inertial data. When tracking a full-body skeleton, the computation time increases notably as the number of elements in the covariance matrices of the EKF grows quadratically with the number of segments. A prototypical hybrid CPU and GPU implementation relying on unified memory<sup>1</sup>, which utilizes matrix operations of *Eigen* and *cuBLAS*<sup>2</sup>, inspired by [Huang 11], has been tested, but yielded no significant performance improvements due to the memory transfer latencies. A fully optimized GPU implementation, however, might provide remedy.

Concerning muscle activation estimations, any detailed investigations require more attention than has been possible within the cope of these studies. Muscle activation trajectories should be ideally compared with known, expected patterns or activation profiles of similar movements. If predicted activations are as robust against I2S calibration errors as the above results suggested, they might be reliably utilized for identification and classifications of (partial) motion sequences, i.e kinematic patterns, gait events or pathological deviations. Technically, this might be implemented applying machine learning methods or simply template matching based on multi-dimensional cross-correlations of activations.

Finally, for the sake of comparability and in order to evaluate different musculoskeletal models and analysis methods, an additional interfacing with OpenSim [OpenSim Doc. 17], another established framework for biomechanical simulation, would be desirable in future.

---

<sup>1</sup><http://docs.nvidia.com/cuda/cuda-c-programming-guide/#um-introduction>

<sup>2</sup><http://docs.nvidia.com/cuda/cublas>





# Bibliography

- [Andersen 09] M. S. Andersen, M. Damsgaard, J. Rasmussen, “Kinematic analysis of over-determinate biomechanical systems”, *Computer Methods in Biomechanics and Biomedical Engineering*, vol. 12, no. 4, pp. 371–384, 2009.
- [Andersen 10] M. S. Andersen, M. Damsgaard, B. MacWilliams, J. Rasmussen, “A computationally efficient optimisation-based method for parameter identification of kinematically determinate and over-determinate biomechanical systems”, *Computer methods in biomechanics and biomedical engineering*, vol. 13, no. 2, pp. 171–183, 2010.
- [Anderson 01] F. C. Anderson, M. G. Pandy, “Dynamic optimization of human walking”, *Journal of biomechanical engineering*, vol. 123, no. 5, pp. 381–390, 2001.
- [AnyBody Doc. 17] AnyBody Doc , “AnyBody Documentation”, <https://github.com/AnyBody/support/wiki>, 2017. [Online; accessed April 29, 2017].
- [AnyBody Tech. 09] AnyBody Tech , “Spine Rhythm”, [https://github.com/AnyBody/support/blob/master/Wiki\\_Files/AnyBody\\_Body\\_Model/Spinerhythm.pdf](https://github.com/AnyBody/support/blob/master/Wiki_Files/AnyBody_Body_Model/Spinerhythm.pdf), 2009. [Online; accessed April 29, 2017].
- [AnyBody Tech. 11] AnyBody Tech , “Shoulder Rhythm Report”, [http://github.com/AnyBody/support/blob/master/Wiki\\_Files/AnyBody\\_Body\\_Model/ShoulderRhythmReport.pdf](http://github.com/AnyBody/support/blob/master/Wiki_Files/AnyBody_Body_Model/ShoulderRhythmReport.pdf), 2011. [Online; accessed April 29, 2017].
- [AnyBody Tech. 16] AnyBody Tech , “Ground Reaction Force Prediction Mocap Example”, <http://https://github.com/AnyBody/GRF-prediction>, 2016. [Online; accessed May 21, 2017].
- [AnyBody Tech. 17] AnyBody Tech , “Inertial MoCap Example”, [http://github.com/AnyBody/inertial\\_mocap\\_example](http://github.com/AnyBody/inertial_mocap_example), 2017. [Online; accessed June 04, 2017].
- [Arnold 10] E. M. Arnold, S. R. Ward, R. L. Lieber, S. L. Delp, “A model of the lower limb for analysis of human movement”, *Annals of biomedical engineering*, vol. 38, no. 2, pp. 269–279, 2010.
- [Audu 03] M. L. Audu, R. F. Kirsch, R. J. Triolo, “A computational technique for determining the ground reaction forces in human bipedal stance”, *Journal of Applied Biomechanics*, vol. 19, no. 4, pp. 361–371, 2003.
- [Baerlocher 01] P. Baerlocher, R. Boulic, “Parametrization and range of motion of the ball-and-socket joint”, in *Deformable avatars*, Springer, 2001, pp. 180–190.

- [Barrett 07] R. S. Barrett, T. F. Besier, D. G. Lloyd, “Individual muscle contributions to the swing phase of gait: An EMG-based forward dynamics modelling approach”, *Simulation Modelling Practice and Theory*, vol. 15, no. 9, pp. 1146–1155, 2007.
- [Bartlett 07] R. Bartlett, *Introduction to sports biomechanics: Analysing human movement patterns*, Routledge, 2007.
- [Black 64] H. D. Black, “A passive system for determining the attitude of a satellite”, *AIAA journal*, vol. 2, no. 7, pp. 1350–1351, 1964.
- [Bleser 09] G. Bleser, D. Stricker, “Advanced tracking through efficient image processing and visual-inertial sensor fusion”, *Computers & Graphics*, vol. 33, no. 1, pp. 59–72, 2009.
- [Bleser 12] G. Bleser, “Object and people tracking lecture slides”, [http://ags.cs.uni-kl.de/fileadmin/inf\\_ags/opt-ss12/lec10\\_opt.pdf](http://ags.cs.uni-kl.de/fileadmin/inf_ags/opt-ss12/lec10_opt.pdf), 2012. [Online; accessed May 05, 2017].
- [Bleser 15a] G. Bleser, D. Damen, A. Behera, G. Hendebby, K. Mura, M. Miezal, A. Gee, N. Petersen, G. Mações, H. Domingues et al, “Cognitive learning, monitoring and assistance of industrial workflows using egocentric sensor networks”, *PloS one*, vol. 10, no. 6, p. e0127769, 2015.
- [Bleser 15b] G. Bleser, D. Steffen, A. Reiss, M. Weber, G. Hendebby, L. Fradet, “Personalized Physical Activity Monitoring Using Wearable Sensors”, in *Smart Health - Open Problems and Future Challenges*, 2015, pp. 99–124.
- [Bobbert 90] M. F. Bobbert, H. C. Schamhardt, “Accuracy of determining the point of force application with piezoelectric force plates”, *Journal of Biomechanics*, vol. 23, no. 7, pp. 705–710, 1990.
- [Choi 13] A. Choi, J.-M. Lee, J. H. Mun, “Ground reaction forces predicted by using artificial neural network during asymmetric movements”, *International Journal of Precision Engineering and Manufacturing*, vol. 14, no. 3, pp. 475–483, 2013.
- [Christophy 12] M. Christophy, N. A. F. Senan, J. C. Lotz, O. M. O’Reilly, “A musculoskeletal model for the lumbar spine”, *Biomechanics and modeling in mechanobiology*, vol. 11, no. 1–2, pp. 19–34, 2012.
- [Clauser 69] C. E. Clauser, J. T. McConville, J. W. Young, “Weight, volume, and center of mass of segments of the human body”, DTIC Document, Tech. Rep., 1969.
- [Contini 63] R. Contini, R. J. Drillis, M. Bluestein, “Determination of Body Segment Parameters 1”, *Human Factors*, vol. 5, no. 5, pp. 493–504, 1963.
- [Crosbie 08] J. Crosbie, S. L. Kilbreath, L. Hollmann, S. York, “Scapulohumeral rhythm and associated spinal motion”, *Clinical Biomechanics*, vol. 23, no. 2, pp. 184–192, 2008.
- [Damsgaard 06] M. Damsgaard, J. Rasmussen, S. T. Christensen, E. Surma, M. De Zee, “Analysis of musculoskeletal systems in the AnyBody Modeling System”, *Simulation Modelling Practice and Theory*, vol. 14, no. 8, pp. 1100–1111, 2006.

- [Dantam 14] N. Dantam, “Quaternion Computation”, 2014.
- [Davis 91] R. B. Davis, S. Ounpuu, D. Tyburski, J. R. Gage, “A gait analysis data collection and reduction technique”, *Human movement science*, vol. 10, no. 5, pp. 575–587, 1991.
- [Davy 87] D. Davy, M. Audu, “A dynamic optimization technique for predicting muscle forces in the swing phase of gait”, *Journal of biomechanics*, vol. 20, no. 2, pp. 187–201, 1987.
- [De Groot 01] J. De Groot, R. Brand, “A three-dimensional regression model of the shoulder rhythm”, *Clinical Biomechanics*, vol. 16, no. 9, pp. 735–743, 2001.
- [De Zee 07] M. De Zee, L. Hansen, C. Wong, J. Rasmussen, E. B. Simonsen, “A generic detailed rigid-body lumbar spine model”, *Journal of biomechanics*, vol. 40, no. 6, pp. 1219–1227, 2007.
- [Della Croce 06] U. Della Croce, “Soft tissue artifacts in human movement analysis”, in *Proceedings of the IXth International Symposium on the 3D Analysis of Human Movement*. 2006.
- [Delp 07] S. L. Delp, F. C. Anderson, A. S. Arnold, P. Loan, A. Habib, C. T. John, E. Guendelman, D. G. Thelen, “OpenSim: open-source software to create and analyze dynamic simulations of movement”, *IEEE transactions on biomedical engineering*, vol. 54, no. 11, pp. 1940–1950, 2007.
- [Demircan 09] E. Demircan, O. Khatib, J. Wheeler, S. Delp, “Reconstruction and EMG-informed control, simulation and analysis of human movement for athletics: Performance improvement and injury prevention”, in *Engineering in Medicine and Biology Society, 2009. EMBC 2009. Annual International Conference of the IEEE*, IEEE. 2009, pp. 6534–6537.
- [Dobrowolski 15] P. Dobrowolski, “Swing-twist decomposition in Clifford algebra”, *arXiv preprint arXiv:1506.05481*, 2015.
- [Dorfmueller-Ulhaas 02] K. Dorfmueller-Ulhaas, “Optical Tracking - From User Motion To 3D Interaction”, Dissertation, Institute of Computer Graphics and Algorithms, Vienna University of Technology, 2002.
- [Elmenreich 02] W. Elmenreich, “An introduction to sensor fusion”, *Vienna University of Technology, Austria*, 2002.
- [Fluit 14] R. Fluit, M. S. Andersen, S. Kolk, N. Verdonschot, H. Koopman, “Prediction of ground reaction forces and moments during various activities of daily living”, *Journal of biomechanics*, vol. 47, no. 10, pp. 2321–2329, 2014.
- [Fusion3D 09] Fusion3D, “Fusion3D project research”, <http://www.utwente.nl/en/et/bw/research/projects/Fusion3D>, 2009. [Online; accessed May 30, 2017].
- [Gail 15] T. Gail, R. Hoffmann, M. Miezal, G. Bleser, S. Leyendecker, “Towards bridging the gap between motion capturing and biomechanical optimal control simulations”, in *Thematic Conference on Multibody Dynamics*. 2015.

- [Gander 08] W. Gander, “The Singular Value Decomposition”, [http://www2.math.ethz.ch/education/bachelor/lectures/hs2014/other/linalg\\_INFk/svdneu.pdf](http://www2.math.ethz.ch/education/bachelor/lectures/hs2014/other/linalg_INFk/svdneu.pdf), 2008. [Online; accessed May 23, 2017].
- [Ganley 04] K. J. Ganley, C. M. Powers, “Determination of lower extremity anthropometric parameters using dual energy X-ray absorptiometry: the influence on net joint moments during gait”, *Clinical Biomechanics*, vol. 19, no. 1, pp. 50–56, 2004.
- [Garofalo 10] P. Garofalo, “Development of motion analysis protocols based on inertial sensors”, Dissertation, PhD thesis, University of Bologna, 2010.
- [Grassia 98] F. S. Grassia, “Practical parameterization of rotations using the exponential map”, *Journal of graphics tools*, vol. 3, no. 3, pp. 29–48, 1998.
- [Greger 88] R. Greger, *Advances in comparative and environmental physiology*, Springer, 1988.
- [Hartenberg 55] R. S. Hartenberg, J. Denavit, “A kinematic notation for lower pair mechanisms based on matrices”, *Journal of applied mechanics*, vol. 77, no. 2, pp. 215–221, 1955.
- [Hill 38] A. V. Hill, “The heat of shortening and the dynamic constants of muscle”, *Proceedings of the Royal Society of London B: Biological Sciences*, vol. 126, no. 843, pp. 136–195, 1938.
- [Horsman 07] K. Horsman, M. Dirk, *The Twente lower extremity model: consistent dynamic simulation of the human locomotor apparatus*, University of Twente, 2007.
- [Huang 11] M.-Y. Huang, S.-C. Wei, B. Huang, Y.-L. Chang, “Accelerating the Kalman Filter on a GPU”, in *Parallel and Distributed Systems (ICPADS), 2011 IEEE 17th International Conference on*, IEEE. 2011, pp. 1016–1020.
- [Huxley 57] A. F. Huxley, “Muscle structure and theories of contraction”, *Prog Biophys Biophys Chem*, vol. 7, pp. 257–318, 1957.
- [Huyghe 11] B. Huyghe, “Design and implementation of a mobile sensor system for human posture tracking”, Dissertation, Ghent University, 2011.
- [Jonkers 02] I. Jonkers, A. Spaepen, G. Papaioannou, C. Stewart, “An EMG-based, muscle driven forward simulation of single support phase of gait”, *Journal of biomechanics*, vol. 35, no. 5, pp. 609–619, 2002.
- [Jovanović 15] K. Jovanović, J. Vranić, N. Miljković, “Hill’s and Huxley’s muscle models: Tools for simulations in biomechanics”, *Serbian Journal of Electrical Engineering*, vol. 12, no. 1, pp. 53–67, 2015.
- [Kadaba 89] M. Kadaba, H. Ramakrishnan, M. Wootten, J. Gainey, G. Gorton, G. Cochran, “Repeatability of kinematic, kinetic, and electromyographic data in normal adult gait”, *Journal of Orthopaedic Research*, vol. 7, no. 6, pp. 849–860, 1989.

- [Kainz 16] H. Kainz, L. Modenese, D. Lloyd, S. Maine, H. Walsh, C. Carty, “Joint kinematic calculation based on clinical direct kinematic versus inverse kinematic gait models”, *Journal of biomechanics*, vol. 49, no. 9, pp. 1658–1669, 2016.
- [Karatsidis 16] A. Karatsidis, G. Bellusci, H. M. Schepers, M. de Zee, M. S. Andersen, P. H. Veltink, “Estimation of ground reaction forces and moments during gait using only inertial motion capture”, *Sensors*, vol. 17, no. 1, p.75, 2016.
- [Kok 14] M. Kok, J. D. Hol, T. B. Schön, “An optimization-based approach to human body motion capture using inertial sensors”, *IFAC Proceedings Volumes*, vol. 47, no. 3, pp. 79–85, 2014.
- [Koning 11] B. Koning, S. van de Stadt, C. Baten, B. Koopman, “Sensitivity of musculoskeletal simulation outcomes to motion capturing method”, <http://bme2011.fyper.com/mobview/presentation/560>, 2011. [Online; accessed May 30, 2017].
- [Kuo 95] A. D. Kuo, “A least-squares estimation approach to improving the precision of inverse dynamics computations”, *Ann Arbor*, vol. 1050, p. 48109, 1995.
- [Leardini 05] A. Leardini, L. Chiari, U. Della Croce, A. Cappozzo, “Human movement analysis using stereophotogrammetry”, *Gait & posture*, vol. 21, no. 2, pp. 212–225, 2005.
- [Ligorio 16] G. Ligorio, A. M. Sabatini, “Dealing with magnetic disturbances in human motion capture: A survey of techniques”, *Micromachines*, vol. 7, no. 3, p.43, 2016.
- [Liu 12] C. K. Liu, S. Jain, “A quick tutorial on multibody dynamics”, *Online tutorial*, June, p.7, 2012.
- [Lohnert 10] K. Lohnert, “Eignung von Inertialsensorik zum Einsatz in der Instrumentellen Ganganalyse - Methodenvergleich 3D-Optik versus Inertialsensorik”, 2010.
- [Lund 15] M. E. Lund, M. S. Andersen, M. de Zee, J. Rasmussen, “Scaling of musculoskeletal models from static and dynamic trials”, *International Biomechanics*, vol. 2, no. 1, pp. 1–11, 2015.
- [Manal 04] K. T. Manal, T. S. Buchanan, “Biomechanics of human movement”, *Standard handbook of biomedical engineering & design*, p.26, 2004.
- [Mandery 15] C. Mandery, O. Terlemez, M. Do, N. Vahrenkamp, T. Asfour, “The KIT Whole-Body Human Motion Database”, in *International Conference on Advanced Robotics (ICAR)*. July 2015, pp. 329–336.
- [Miezal 12] M. Miezal, G. Bleser, D. Stricker, J. Tümler, “Towards practical inside-out head tracking for mobile seating bucks”, in *Proceedings of International Symposium on Mixed and Augmented Reality (ISMAR)*. Atlanta, USA. 2012.
- [Miezal 13] M. Miezal, G. Bleser, N. Schmitz, D. Stricker, “A generic approach to inertial tracking of arbitrary kinematic chains”, in *Proceedings of the 8th international conference on body area networks*, ICST (Institute for Computer Sciences, Social-Informatics and Telecommunications Engineering). 2013, pp. 189–192.

- [Miezal 14] M. Miezal, B. Taetz, N. Schmitz, G. Bleser, “Ambulatory inertial spinal tracking using constraints”, in *Proceedings of the 9th International Conference on Body Area Networks*, ICST (Institute for Computer Sciences, Social-Informatics and Telecommunications Engineering). 2014, pp. 131–134.
- [Miezal 16] M. Miezal, B. Taetz, G. Bleser, “On inertial body tracking in the presence of model calibration errors”, *Sensors*, vol. 16, no. 7, p. 1132, 2016.
- [Nigg 07] B. M. Nigg, W. Herzog, *Biomechanics of the musculo-skeletal system*, John Wiley & Sons, 2007.
- [Ojeda 11] J. Ojeda, J. Mayo, J. Martinez-Reina, “Cost Function in Muscle Redundancy Problems: Computational Aspects”, *Mechanics based design of structures and machines*, vol. 39, no. 2, pp. 268–284, 2011.
- [OpenSim Doc. 17] OpenSim Doc , “OpenSim Documentation”, <http://simtk-confluence.stanford.edu:8080/display/OpenSim/OpenSim+Documentation>, 2017. [Online; accessed April 29, 2017].
- [OpenStax College 13] OpenStax College, “Anatomy & Physiology, Connexions Web site”, <http://cnx.org/content/col11496/1.6/>, 2013. [Online; accessed April 27, 2017].
- [OptiTrack Doc. 17] OptiTrack Doc , “OptiTrack Documentation”, [http://wiki.optitrack.com/index.php?title=OptiTrack\\_Documentation\\_Wiki](http://wiki.optitrack.com/index.php?title=OptiTrack_Documentation_Wiki), 2017. [Online; accessed May 05, 2017].
- [Pandy 01] M. G. Pandy, “Computer modeling and simulation of human movement”, *Annual review of biomedical engineering*, vol. 3, no. 1, pp. 245–273, 2001.
- [Piovan 12] G. Piovan, F. Bullo, “On coordinate-free rotation decomposition: Euler angles about arbitrary axes”, *IEEE Transactions on Robotics*, vol. 28, no. 3, pp. 728–733, 2012.
- [Rasmussen 01] J. Rasmussen, M. Damsgaard, M. Voigt, “Muscle recruitment by the min/max criterion—a comparative numerical study”, *Journal of biomechanics*, vol. 34, no. 3, pp. 409–415, 2001.
- [Rasmussen 05] J. Rasmussen, M. d. Zee, M. Damsgaard, S. T. Christensen, C. Marek, K. Siebertz, “A general method for scaling musculo-skeletal models”, in *International symposium on computer simulation in biomechanics*. 2005.
- [Ren 08] L. Ren, R. K. Jones, D. Howard, “Whole body inverse dynamics over a complete gait cycle based only on measured kinematics”, *Journal of biomechanics*, vol. 41, no. 12, pp. 2750–2759, 2008.
- [Ribeiro 11] T. Ribeiro, “Anatomically Correct Animation of a Humanoid”, 2011.
- [Rigatos 10] G. G. Rigatos, “Extended Kalman and Particle Filtering for sensor fusion in motion control of mobile robots”, *Mathematics and computers in simulation*, vol. 81, no. 3, pp. 590–607, 2010.
- [Roetenberg 06] D. Roetenberg, *Inertial and magnetic sensing of human motion*, University of Twente, 2006.



- [Roetenberg 09] D. Roetenberg, H. Luinge, P. Slycke, “Xsens MVN: full 6DOF human motion tracking using miniature inertial sensors”, *Xsens Motion Technologies BV, Tech. Rep*, 2009.
- [Rossi 13] M. Rossi, A. Lyttle, E.-S. Amar, N. Benjanuvatra, B. Blanksby, “Body segment inertial parameters of elite swimmers using DXA and indirect methods”, *Journal of sports science & medicine*, vol. 12, no. 4, p. 761, 2013.
- [Salehi 12] S. Salehi, N. Mostofi, G. Bleser, “A practical in-field magnetometer calibration method for IMUs”, in *Proceedings of the IROS Workshop on Cognitive Assistive Systems: Closing the Action-Perception Loop*. 2012, pp. 39–44.
- [Salehi 13] S. Salehi, G. Bleser, N. Schmitz, D. Stricker, “A low-cost and light-weight motion tracking suit”, in *Ubiquitous Intelligence and Computing, 2013 IEEE 10th International Conference on and 10th International Conference on Autonomic and Trusted Computing (UIC/ATC)*, IEEE. 2013, pp. 474–479.
- [Sartori 12] M. Sartori, M. Reggiani, D. Farina, D. G. Lloyd, “EMG-driven forward-dynamic estimation of muscle force and joint moment about multiple degrees of freedom in the human lower extremity”, *PloS one*, vol. 7, no. 12, p. e52618, 2012.
- [Shuster 93] M. D. Shuster, “A survey of attitude representations”, *Navigation*, vol. 8, no. 9, pp. 439–517, 1993.
- [Skals 16] S. Skals, M. K. Jung, M. Damsgaard, M. S. Andersen, “Prediction of ground reaction forces and moments during sports-related movements”, *Multibody System Dynamics*, pp. 1–21, 2016.
- [Taetz 16] B. Taetz, G. Bleser, M. Miezal, “Towards self-calibrating inertial body motion capture”, in *Information Fusion (FUSION), 2016 19th International Conference on*, IEEE. 2016, pp. 1751–1759.
- [Thelen 03] D. G. Thelen, F. C. Anderson, S. L. Delp, “Generating dynamic simulations of movement using computed muscle control”, *Journal of biomechanics*, vol. 36, no. 3, pp. 321–328, 2003.
- [Thelen 06] D. G. Thelen, F. C. Anderson, “Using computed muscle control to generate forward dynamic simulations of human walking from experimental data”, *Journal of biomechanics*, vol. 39, no. 6, pp. 1107–1115, 2006.
- [Theobalt 02] C. Theobalt, M. A. Magnor, P. Schüller, H.-P. Seidel, “Multi-Layer Skeleton Fitting for Online Human Motion Capture.”, in *VMV*. 2002, pp. 471–478.
- [van den Bergen 16] G. van den Bergen, “Rotational Joint Limits in Quaternion Space”, *Game Engine Gems*, vol. 3, 2016.
- [Van der Helm 92] F. C. Van der Helm, H. Veeger, G. Pronk, L. Van der Woude, R. Rozendal, “Geometry parameters for musculoskeletal modelling of the shoulder system”, *Journal of biomechanics*, vol. 25, no. 2, pp. 129–144, 1992.



- [Vaughan 92] C. L. Vaughan, B. L. Davis, J. C. O’connor, *Dynamics of human gait*, Human Kinetics Publishers Champaign, Illinois, 1992, vol. 2.
- [Veeger 91] H. Veeger, F. Van Der Helm, L. Van Der Woude, G. Pronk, R. Rozendal, “Inertia and muscle contraction parameters for musculoskeletal modelling of the shoulder mechanism”, *Journal of biomechanics*, vol. 24, no. 7, pp. 615–629, 1991.
- [Vignais 13] N. Vignais, M. Miezal, G. Bleser, K. Mura, D. Gorecky, F. Marin, “Innovative system for real-time ergonomic feedback in industrial manufacturing”, *Applied ergonomics*, vol. 44, no. 4, pp. 566–574, 2013.
- [Wan 06] E. Wan, “Sigma-point filters: An overview with applications to integrated navigation and vision assisted control”, in *Nonlinear Statistical Signal Processing Workshop, 2006 IEEE*, IEEE. 2006, pp. 201–202.
- [wearHEALTH 15] wearHEALTH, “wearHEALTH group lines of research”, <http://agw.cs.uni-kl.de/en/research>, 2015. [Online; accessed May 29, 2017].
- [Welch 95] G. Welch, G. Bishop, “An introduction to the Kalman filter”, 1995.
- [Wikimedia Commons 10] Wikimedia Commons, “Main body parts: mechanical study (joints and kinematic pairs)”, [https://commons.wikimedia.org/wiki/File:Modele\\_cinematique\\_corps\\_humain.svg](https://commons.wikimedia.org/wiki/File:Modele_cinematique_corps_humain.svg), 2010. [Online; accessed April 27, 2017].
- [Williams 96] J. H. Williams, *Fundamentals of applied dynamics*, New York: John Wiley & Sons, Inc, 1996., 1996.
- [Wilson 00] D. Wilson, J. Feikes, A. Zavatsky, J. O’connor, “The components of passive knee movement are coupled to flexion angle”, *Journal of Biomechanics*, vol. 33, no. 4, pp. 465–473, 2000.
- [Winter 09] D. A. Winter, *Biomechanics and motor control of human movement*, John Wiley & Sons, 2009.
- [Woodman 07] O. J. Woodman, “An introduction to inertial navigation”, University of Cambridge, Computer Laboratory, Tech. Rep., 2007.
- [Young 10] A. D. Young, “Wireless realtime motion tracking system using localised orientation estimation”, 2010.
- [Zimmermann 17] T. Zimmermann, “Sensor-to-Segment Assignment and Pre-Alignment using Machine Learning Algorithms”, Diploma thesis, University of Kaiserslautern, 2017.

# A. Appendix

## A.1 Figures



**Figure A.1:** The AMS full-body model [AnyBody Doc. 17].

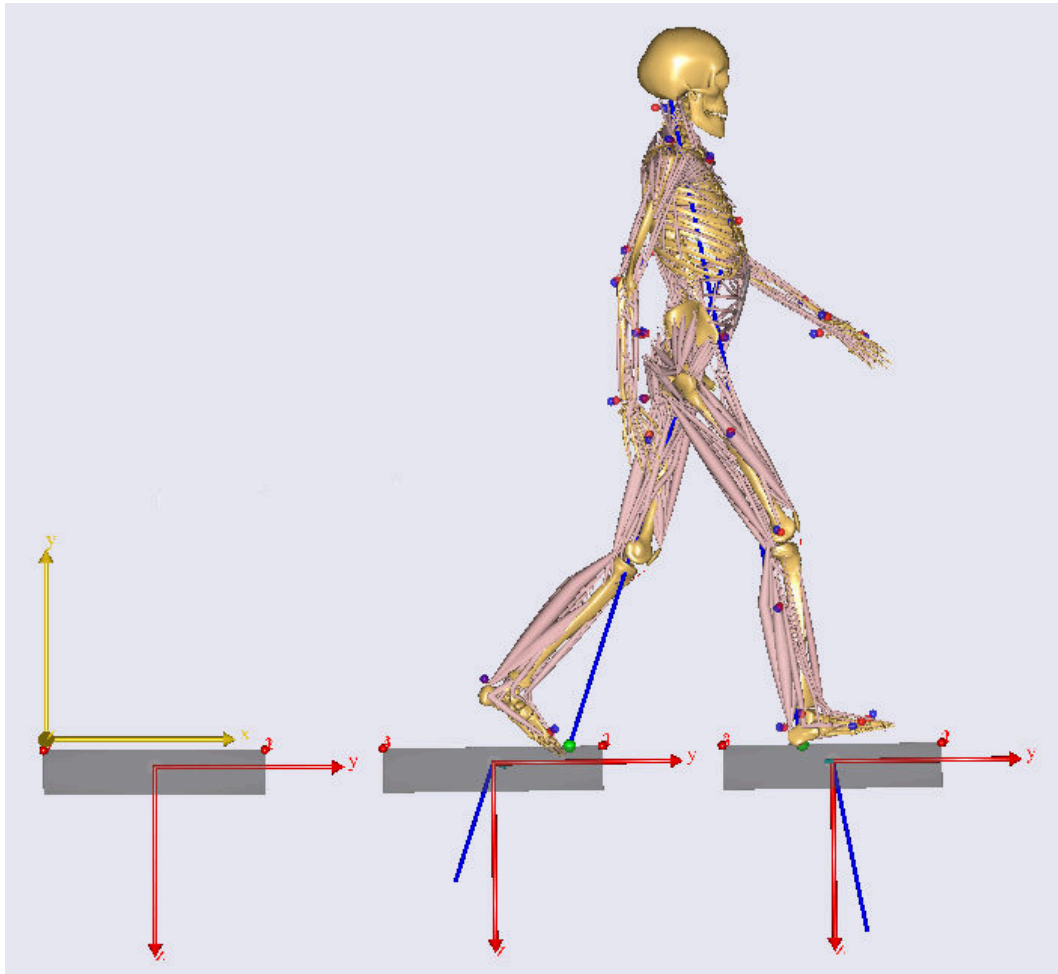


Figure A.2: Gait inverse dynamics simulation visualized in the AMS viewer.

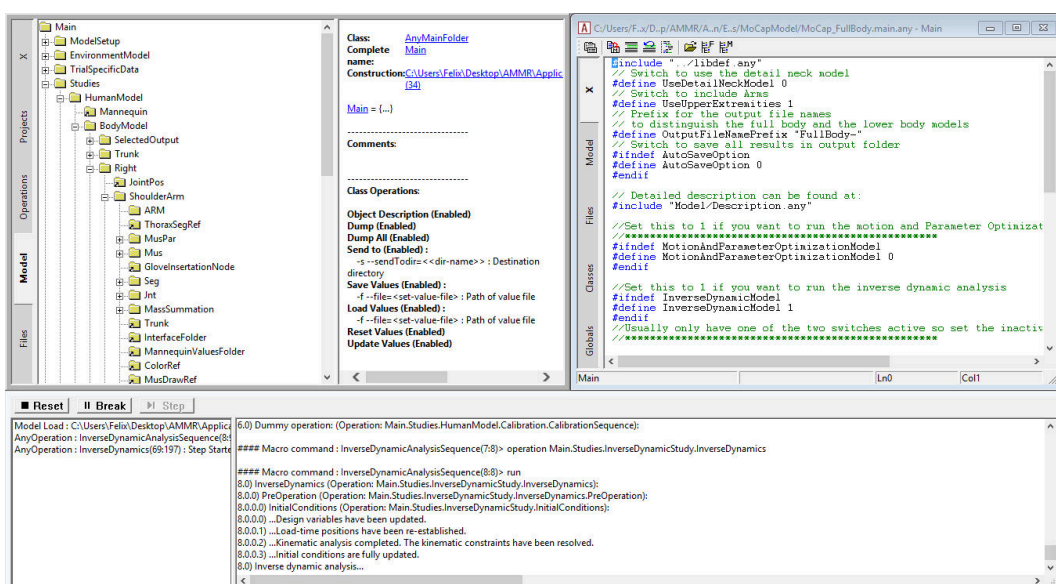


Figure A.3: The AMS workplace.

```

1 <skeleton name="MarsTransformedSkeletonFromAnyBodyBodyModel">
2   <segments>
3     <segment id="0" name="Pelvis">
4       <point id="0" name="Origin">0, 0, 0</point>
5       <point id="1" name="HipJointLeft">0.0340097726512402, 0.0775795830149407, -0.112276873469962</point>
6       <point id="2" name="HipRotLeft">0.0340097726512402, 0.0775795830149407, -0.112276873469962</point>
7       <point id="3" name="HipJointRight">0.0340097726512402, -0.0775795830149407, -0.112276873469962</point>
8       <point id="4" name="HipRotRight">0.0340097726512402, -0.0775795830149407, -0.112276873469962</point>
9       <point id="5" name="PelvisSacrumJoint">0.0263801616868458, 0, -0.029311290763162</point>
10      <point id="6" name="PelvisSacrumRot">0.0263801616868458, 0, -0.029311290763162</point>
11      <point id="7" name="IMUPelvis">0, 0, 0</point>
12    </segment>
13    <segment id="1" name="ThighLeft">
14      <point id="0" name="Origin">0, 0, 0</point>
15      <point id="1" name="HipJoint">0, 0, 0</point>
16      <point id="2" name="HipRot">0, 0, 0</point>
17      <point id="3" name="KneeJoint">0, 0.0381782325598512, -0.423838574673812</point>
18      <point id="4" name="KneeRot">0, 0.0381782325598512, -0.423838574673812</point>
19      <point id="5" name="IMUThighLeft">0, 0.0190891162799256, -0.211919287336906</point>
20    </segment>
21    <segment id="2" name="ShankLeft">
22      <point id="0" name="Origin">0, 0, 0</point>
23      <point id="1" name="KneeJoint">0, 0, 0</point>
24      <point id="2" name="KneeRot">0, 0, 0</point>
25      <point id="3" name="AnkleJoint">0, 0.0683779504719413, -0.396430575738954</point>
26      <point id="4" name="AnkleRot">0, 0.0683779504719413, -0.396430575738954</point>
27      <point id="5" name="IMUShankLeft">0, 0.0341889752359707, -0.198215287869477</point>
28    </segment>
29    <segment id="3" name="TalusLeft">
30      <imu>0, 0, 0, 1, 0, 0, 0</imu>
31      <point id="0" name="Origin">0, 0, 0</point>
32      <point id="1" name="AnkleJoint">0, 0, 0</point>
33      <point id="2" name="AnkleRot">0, 0, 0</point>
34      <point id="3" name="SubTalarJoint">0.007368778516507, 0.00597092951964201, -0.0188209582096478</point>
35      <point id="4" name="SubTalarRot">0.007368778516507, 0.00597092951964201, -0.0188209582096478</point>
36    </segment>

```

Figure A.4: XML skeleton extracted from the AMS model, used by the Quattracker.

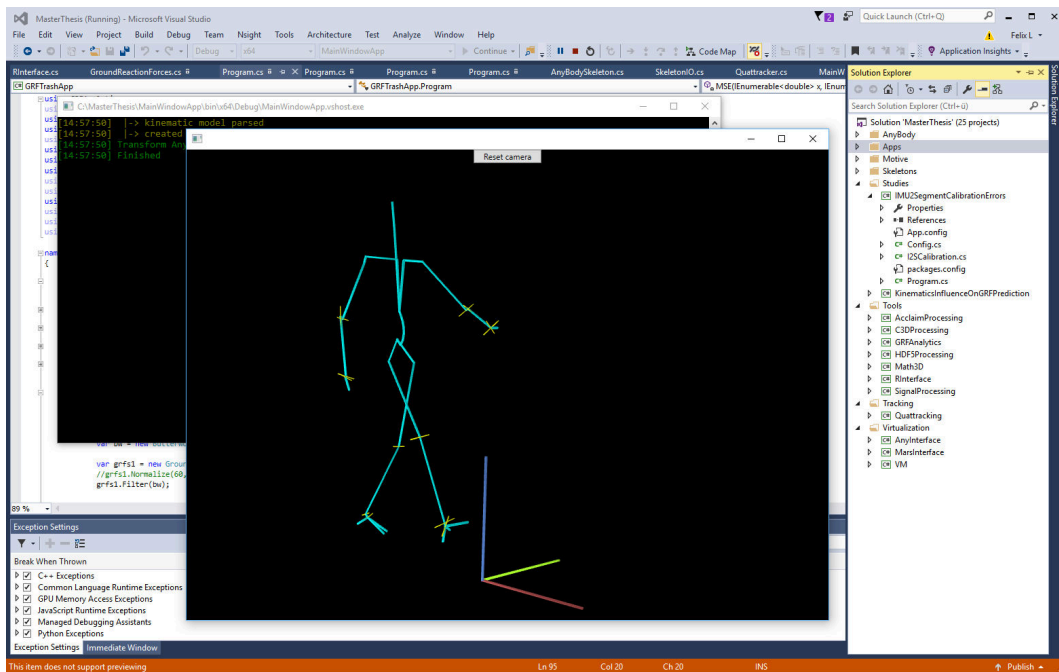


Figure A.5: The pipeline framework with skeleton simulation and rendering.

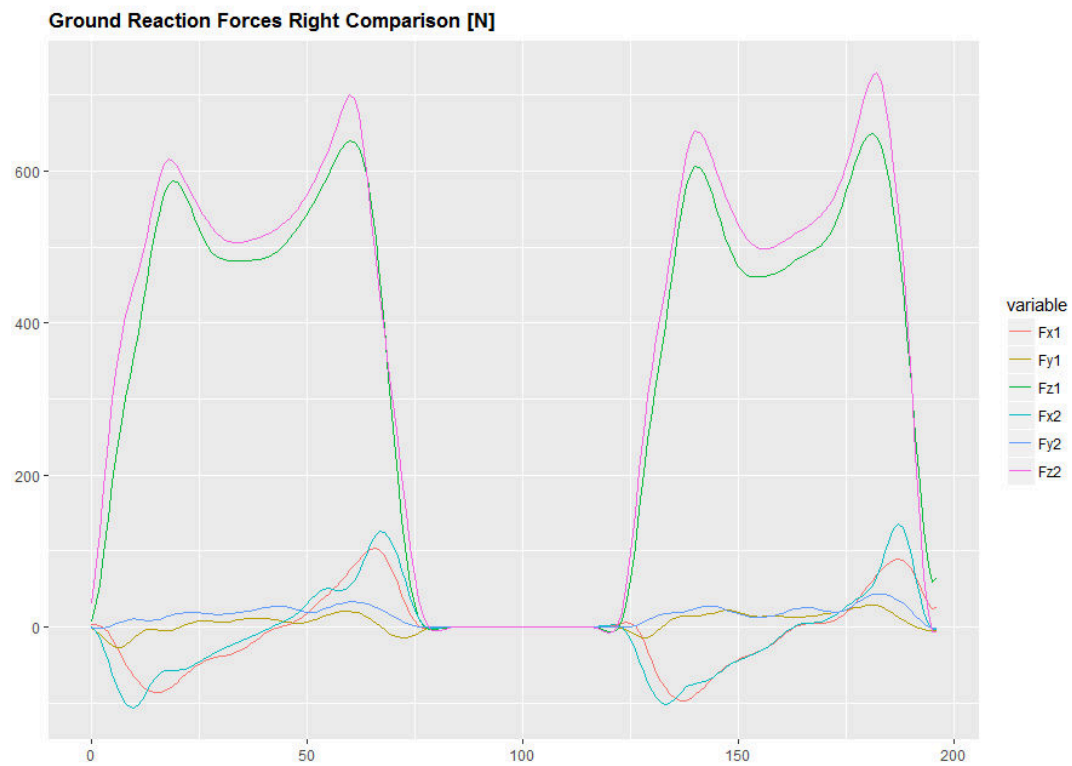


Figure A.6: Visual comparison of measured and predicted GRFs.

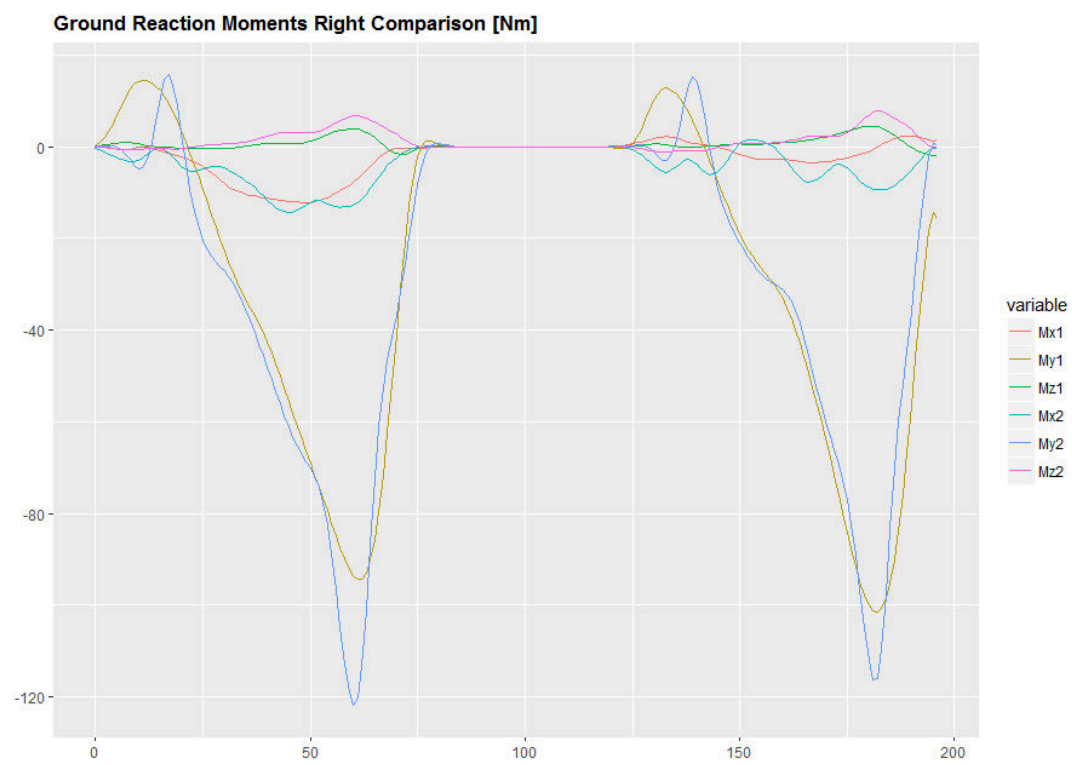


Figure A.7: Visual comparison of measured and predicted GRMs.

## A.2 AMS Hill Type Muscle Model

Summary of the parameters of the `AnyMuscleModel13E` based on the hill type model according to the specification in [AnyBody Doc. 17].

Parameter	Description
$F_{M,0}$ [N]	<i>Maximum neutral/isometric force:</i> The strength of the muscle at neutral fiber length and zero contraction velocity.
$\bar{l}_{M,f}$ [m]	<i>Neutral fiber length:</i> The length of the contractile element at which the muscle has the strength $F_{M,0}$ .
$\bar{l}_{M,t0}$ [m]	<i>Total muscle length:</i> The length of the muscle's contractile element including the slack length of the tendon, i.e. the tendon length when being taut but not subject to any force.
$\bar{\epsilon}_{M,T}$ [1]	<i>Tendon elasticity:</i> The strain of the tendon when subject to a force $F_{M,0}$ , hence implicitly relating the tendon's thickness to the muscle strength.
$\bar{\gamma}_M$ [rad]	<i>Pennation angle:</i> The angle between the muscle's direction of action and the alignment of fibers that relates the tendon and muscle force: $F_T = F_M \cos \gamma$ . As the pennation angle is dependent on the muscle length, a constant value of $\bar{\gamma}$ at neutral length is assumed instead.
$C_{M,fast}$ [1]	<i>Fast twitch fiber fraction:</i> This factor models the fraction of fast twitch versus slow twitch muscle fibers. The former provide fast action at the cost of stamina.
$J_{M,T}$ [1], $J_{M,PE}$ [1]	<i>Tendon and parallel-elastic non-linear elasticity constants:</i> Material constants modeling the non-linear elasticity of the serial-elastic (tendon) and parallel-elastic element, respectively. The shape of the characteristic force-deflection relationships of the both elastic elements is described with these two parameters.
$K_{M,1}$ [s <sup>-1</sup> ], $K_{M,2}$ [s <sup>-1</sup> ]	<i>Factors relating fiber length, composition and fast twitch:</i> $K_{M,1}$ and $K_{M,2}$ relate the muscle's maximum contraction velocity to its physiological characteristics to the effect that muscles with longer fibers and higher fast twitch fractions have a higher maximum contraction velocity.
$PE_M$ [1]	<i>Flexibility factor of the parallel-elastic element:</i> Instead of $J_{M,PE}$ , this factor controls the slope, i.e. the linear component, of the force-deflection relationship of the parallel-elastic element.

**Table A.1:** Parameters of the AnyBody hill type model; adapted from [AnyBody Doc. 17]



## A.3 Shoulder and Spine Rhythm

Implementations of the shoulder rhythm according to [AnyBody Tech. 09], [AnyBody Tech. 11] and the AMS full-body model.

### Shoulder Rhythm

```
KinematicState<EulerAngles> ShoulderRhythm(EulerAngles ghLeft, EulerAngles gHRight)
{
    ghLeft = ghLeft.ToEulerAngles("XZY");
    gHRight = gHRight.ToEulerAngles("XZY");

    // Functions from shoulder rhythm definition in file /Body/AAUHuman/Arm/JntSR.any
    var sCLeft = new EulerAngles(
        0.422 * ghLeft.X - 0.423,
        -0.242 * ghLeft.X + 0.12 * ghLeft.Z + 0.851 * -0.401 - 4.983.ToRad() + 10d.ToRad(),
        0.123 * ghLeft.X - 0.046 * ghLeft.Z + 0.493 * 0.201 + 3.917.ToRad() - 6d.ToRad()
        , "YZX");
    var sCRight = new EulerAngles(
        0.422 * ghRight.X - 0.423,
        -0.242 * ghRight.X + 0.12 * ghRight.Z + 0.851 * -0.401 - 4.983.ToRad() + 10d.ToRad(),
        0.123 * ghRight.X - 0.046 * ghRight.Z + 0.493 * 0.201 + 3.917.ToRad() - 6d.ToRad()
        , "YZX");
    var sign = -1d;
    var sTLeft = new EulerAngles(
        0d,
        sign * (-0.049 * ghLeft.X + 0.14 * ghLeft.Z - 1.203.ToRad() + 0.901 * 0.33 +
            10d.ToRad()),
        sign * (0.396 * ghLeft.X - 0.079 * ghLeft.Z + 3.095.ToRad() + 0.414 * 0.307 -
            10d.ToRad())
        , "YZX");
    sign = +1d;
    var sTRight = new EulerAngles(
        0d,
        sign * (-0.049 * gHRight.X + 0.14 * gHRight.Z - 1.203.ToRad() + 0.901 * 0.33 +
            10d.ToRad()),
        sign * (0.396 * gHRight.X - 0.079 * gHRight.Z + 3.095.ToRad() + 0.414 * 0.307 -
            10d.ToRad())
        , "YZX");

    return new KinematicState<EulerAngles>(new Dictionary<string, EulerAngles>()
    {
        { "SternoClavicularLeft", sCLeft },
        { "SternoClavicularRight", sCRight },
        { "ScapulaThoraxLeft", sTLeft },
        { "ScapulaThoraxRight", sTRight }
    });
}
```

## Spine Rhythm

```

KinematicState<EulerAngles> SpineRhythm(EulerAngles pelvisThorax)
{
    pelvisThorax = pelvisThorax.ToEulerAngles("ZYX");
    var t12L1W = Matrix<double>.Build.DenseOfArray(new[,]
    {
        // Weight matrix from spine rhythm definition in file
        // Body/AAUHuman/Trunk/SRMatrixes.any
        { 7.105616e-002, 2.276759e-001, 4.020500e-001, 5.784718e-001, 7.462112e-001,
          9.131695e-001, 1.000000000000 },
        { 0.000000000000, 1.421123e-001, 3.132395e-001, 4.908604e-001, 6.660833e-001,
          8.263391e-001, 1.000000000000 },
        { 7.105616e-002, 2.276759e-001, 4.020500e-001, 5.784718e-001, 7.462112e-001,
          9.131695e-001, 1.000000000000 }
    });
    var t12L1 = new EulerAngles(pelvisThorax.X / t12L1WMat.Row(0).Sum(),
                                pelvisThorax.Y / t12L1WMat.Row(1).Sum(),
                                pelvisThorax.Z / t12L1WMat.Row(2).Sum());

    return new KinematicState<EulerAngles>(new Dictionary<string, EulerAngles>()
    {
        { "SacrumPelvis", new EulerAngles(t12L1.X * t12L1W[0, 0], t12L1.Y * t12L1W[1, 0],
          t12L1.Z * t12L1W[2, 0]) },
        { "L5Sacrum", new EulerAngles(t12L1.X * t12L1W[0, 1], t12L1.Y * t12L1W[1, 1],
          t12L1.Z * t12L1W[2, 1]) },
        { "L4L5", new EulerAngles(t12L1.X * t12L1W[0, 2], t12L1.Y * t12L1W[1, 2],
          t12L1.Z * t12L1W[2, 2]) },
        { "L3L4", new EulerAngles(t12L1.X * t12L1W[0, 3], t12L1.Y * t12L1W[1, 3],
          t12L1.Z * t12L1W[2, 3]) },
        { "L2L3", new EulerAngles(t12L1.X * t12L1W[0, 4], t12L1.Y * t12L1W[1, 4],
          t12L1.Z * t12L1W[2, 4]) },
        { "L1L2", new EulerAngles(t12L1.X * t12L1W[0, 5], t12L1.Y * t12L1W[1, 5],
          t12L1.Z * t12L1W[2, 5]) },
        { "T12L1", t12L1 }
    });
}

```

## A.4 Qualitative I2S Error Distributions

Surface plots of the correlations and relative root mean square errors of disturbed GRFs and GRMs depending on both error axes for all segments and initial calibrations, where the segment axis error is plotted on the horizontal and the lateral axis error on the vertical axis; a darker coloring indicates higher values of  $r$  and  $e_R$ .



### Distribution of I2S Calibration Errors: Anterior Initial IMU Configuration

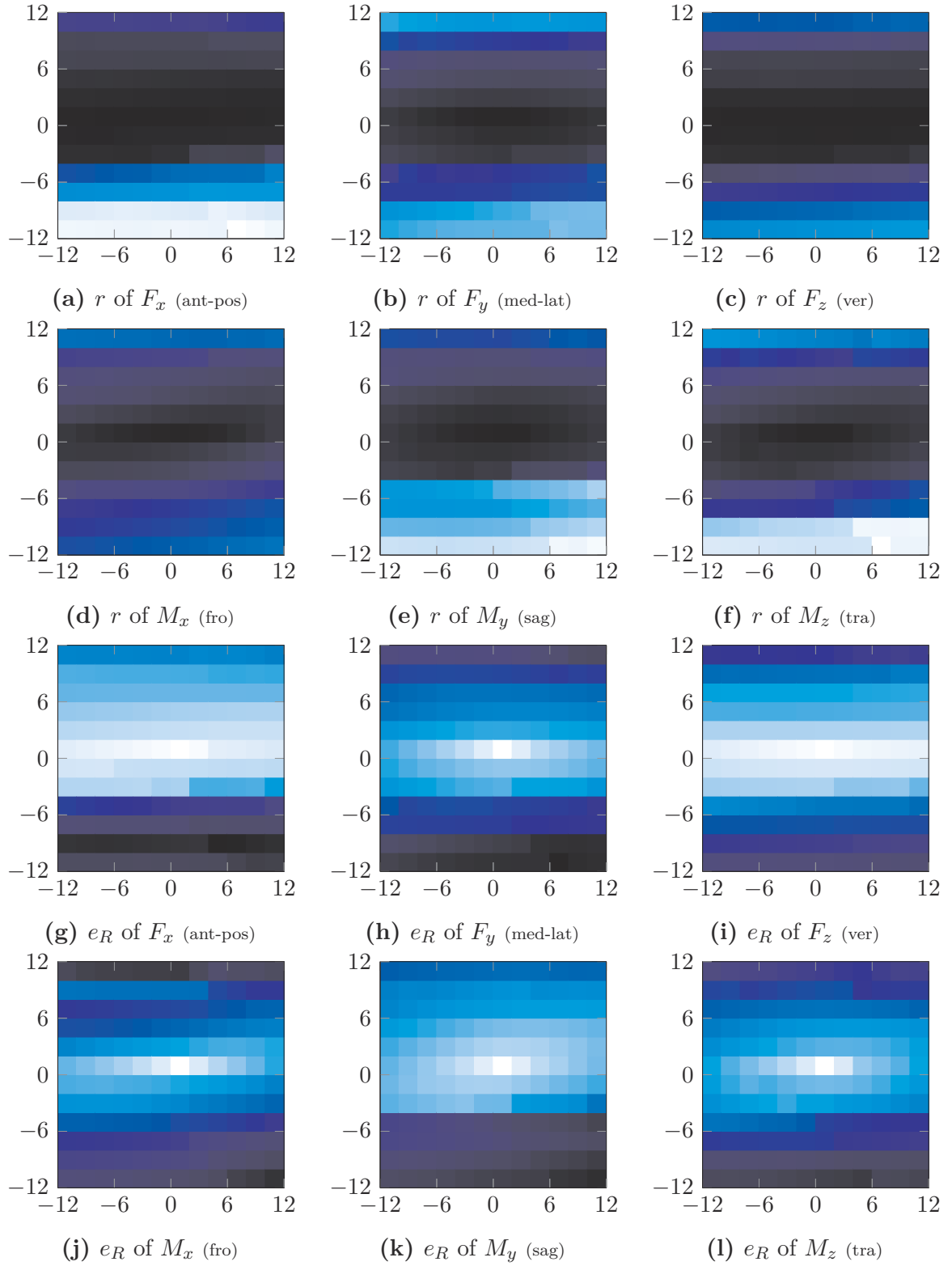


**Figure A.8:** Qualitative distributions for the pelvis I2S calibration errors with an anterior initial IMU calibration.

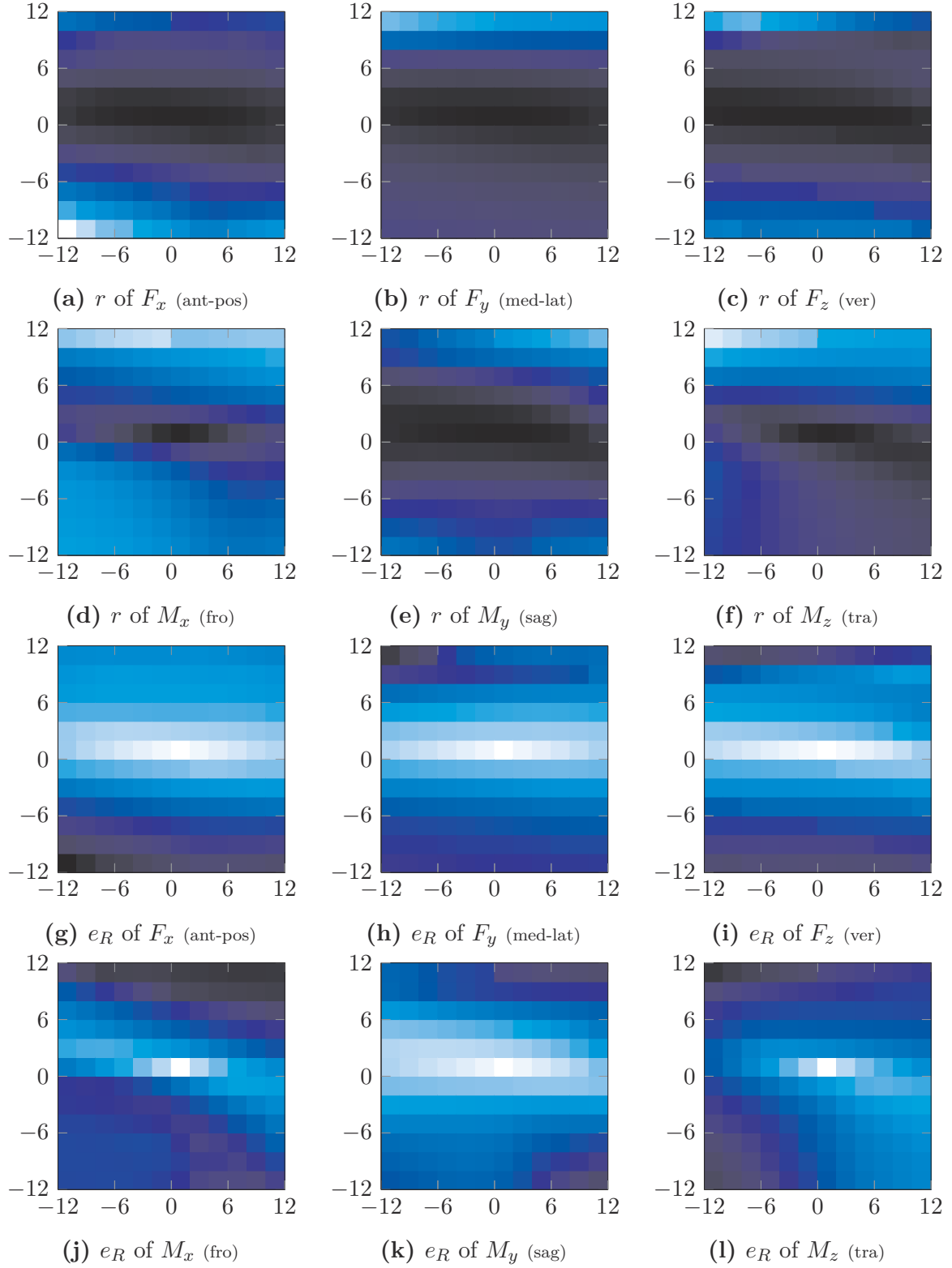


**Figure A.9:** Qualitative distributions for the thigh I2S calibration errors with an anterior initial IMU calibration.

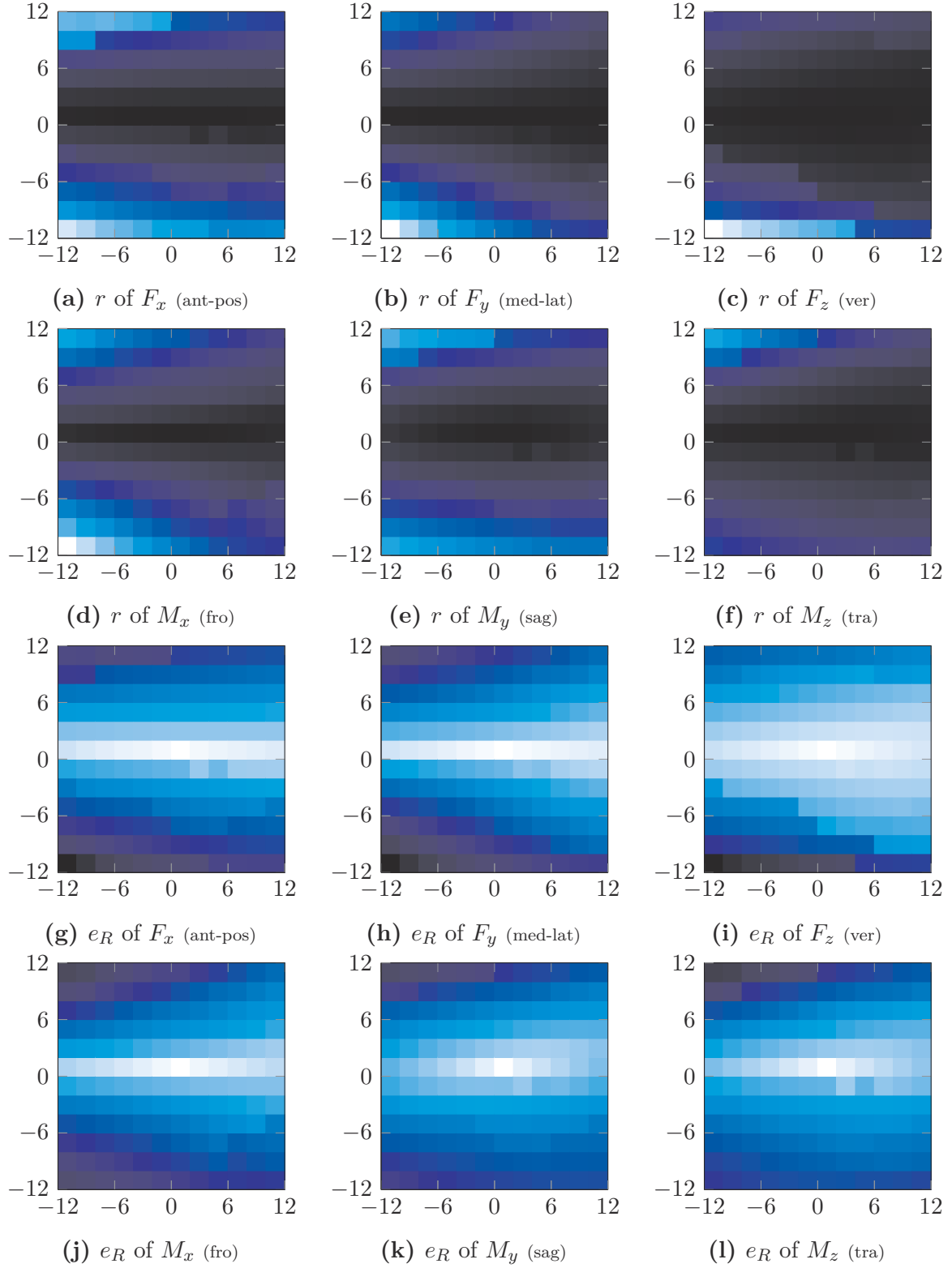


**Figure A.10:** Qualitative distributions for the shank I2S calibration errors with an anterior initial IMU calibration.

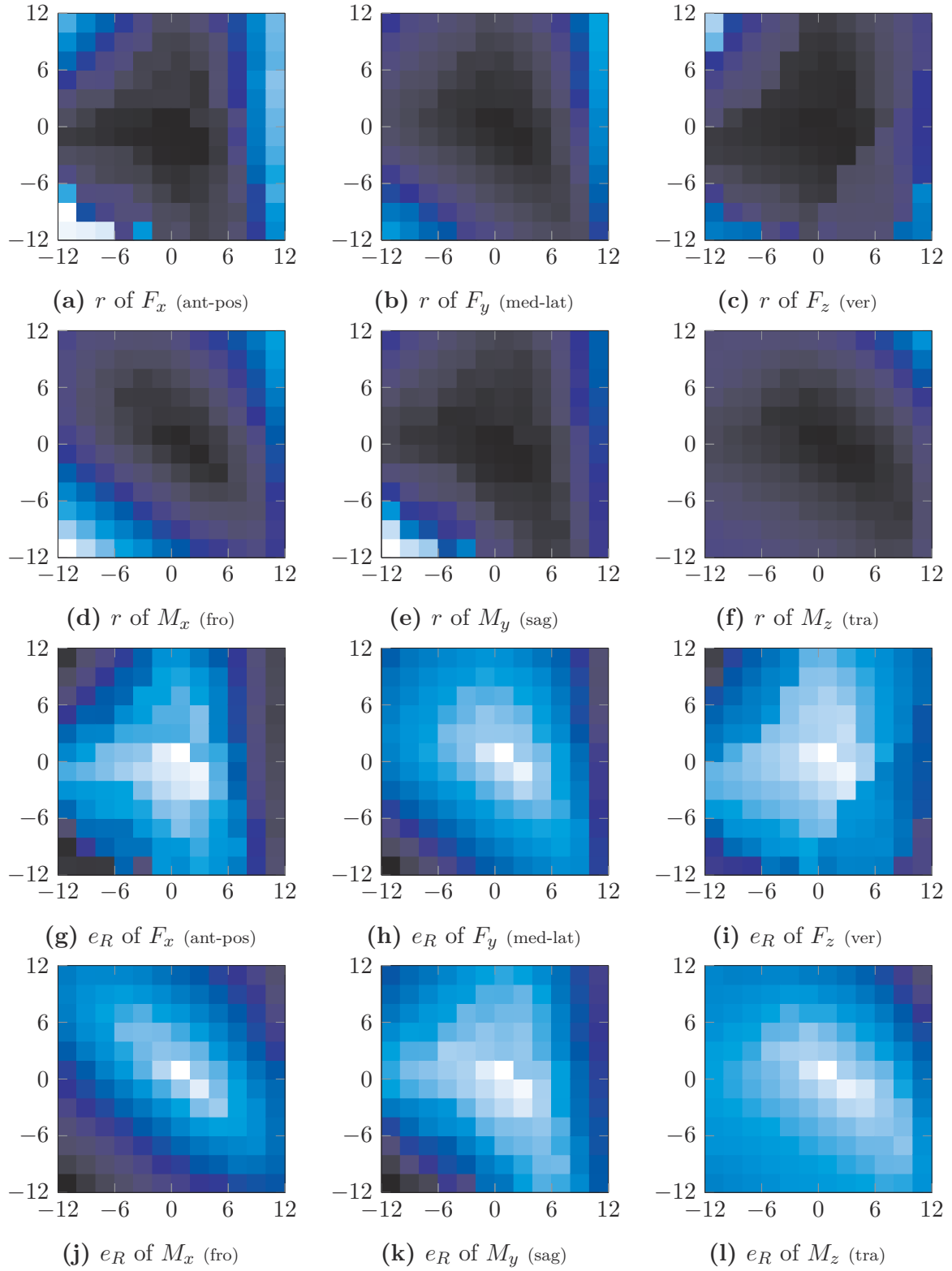


**Figure A.11:** Qualitative distributions for the foot I2S calibration errors with an anterior initial IMU calibration.

### Distribution of I2S Calibration Errors: Lateral Initial IMU Configuration

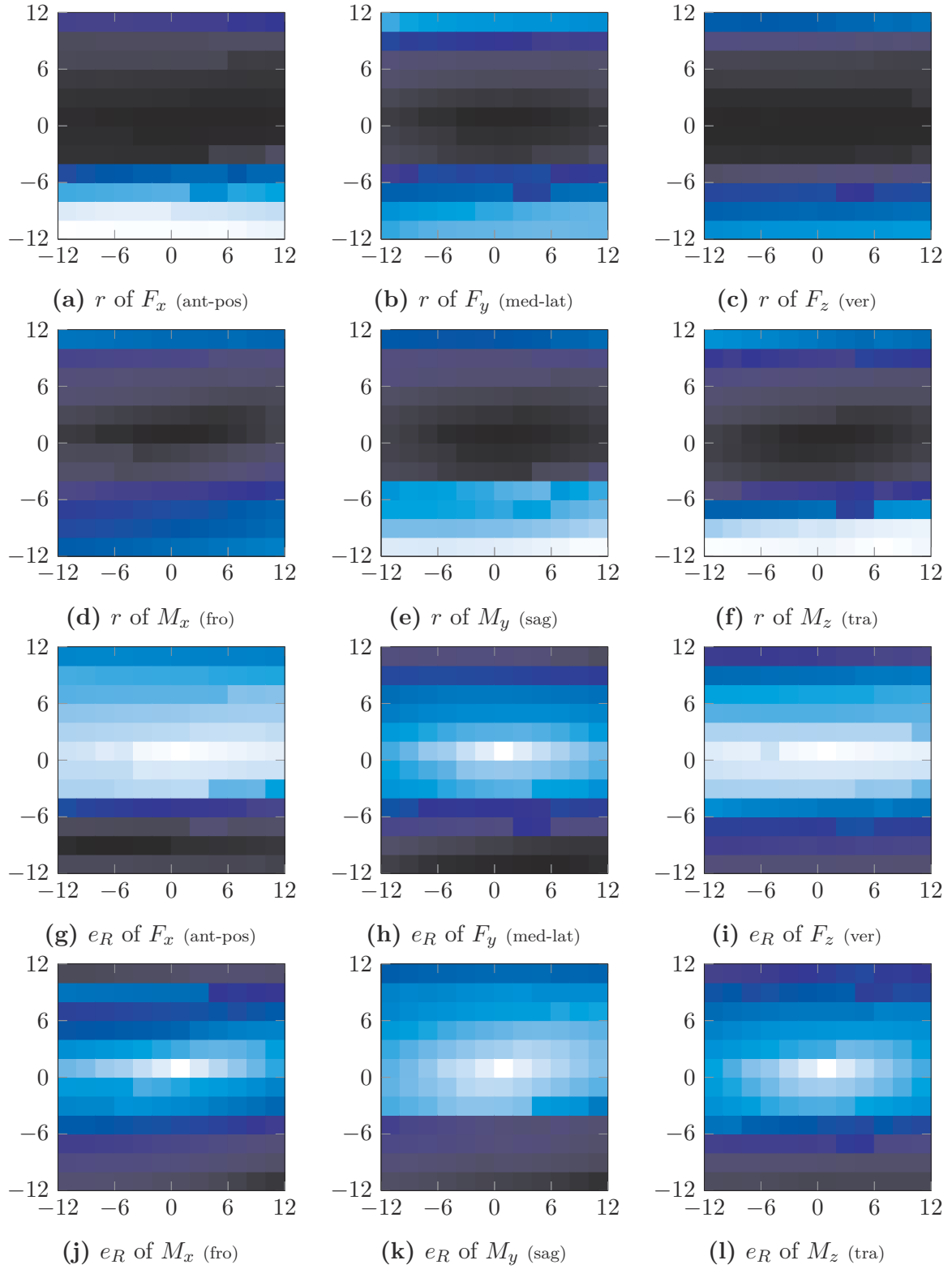


**Figure A.12:** Qualitative distributions for the pelvis I2S calibration errors with a lateral initial IMU calibration.

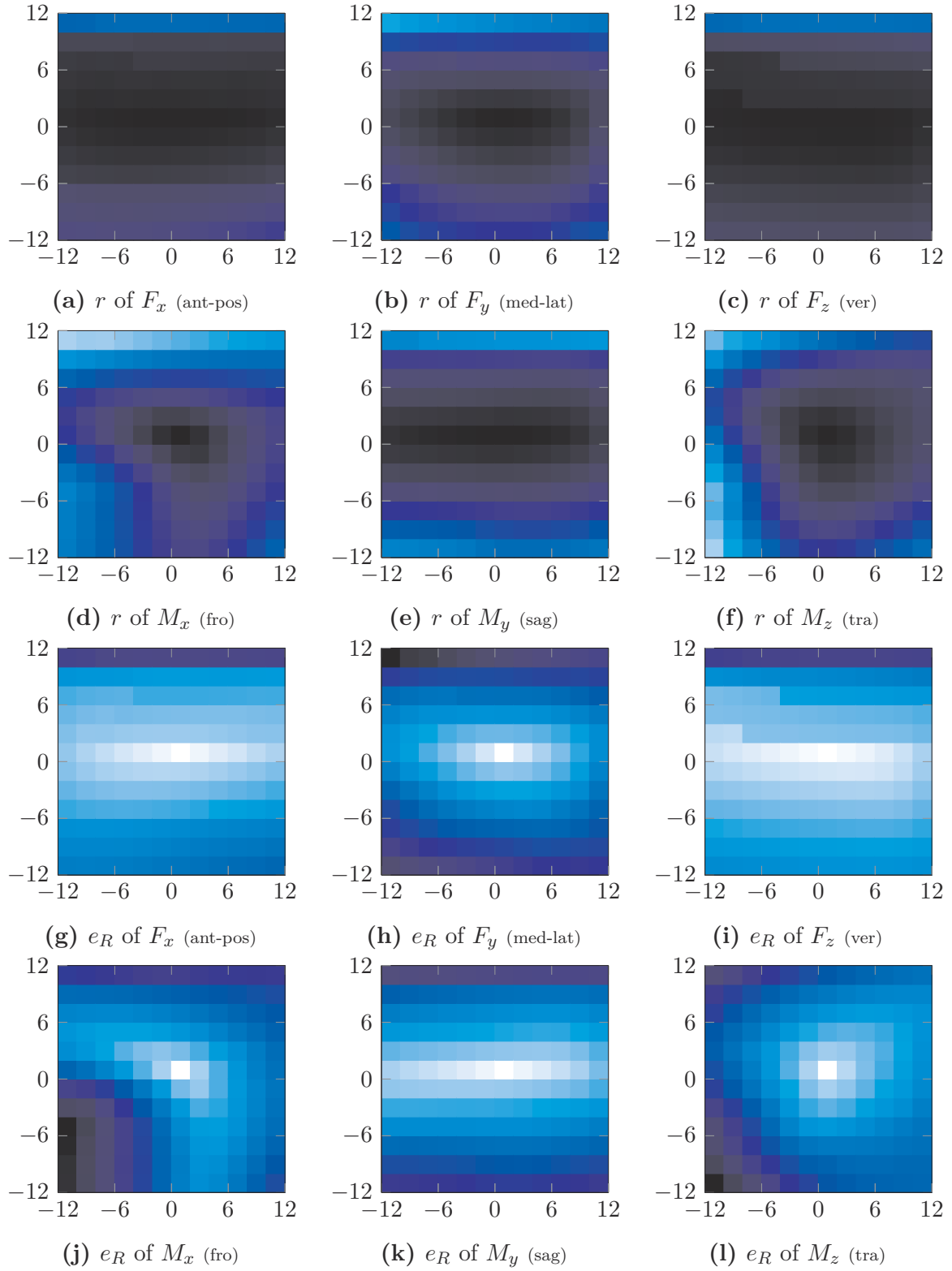


**Figure A.13:** Qualitative distributions for the thigh I2S calibration errors with a lateral initial IMU calibration.

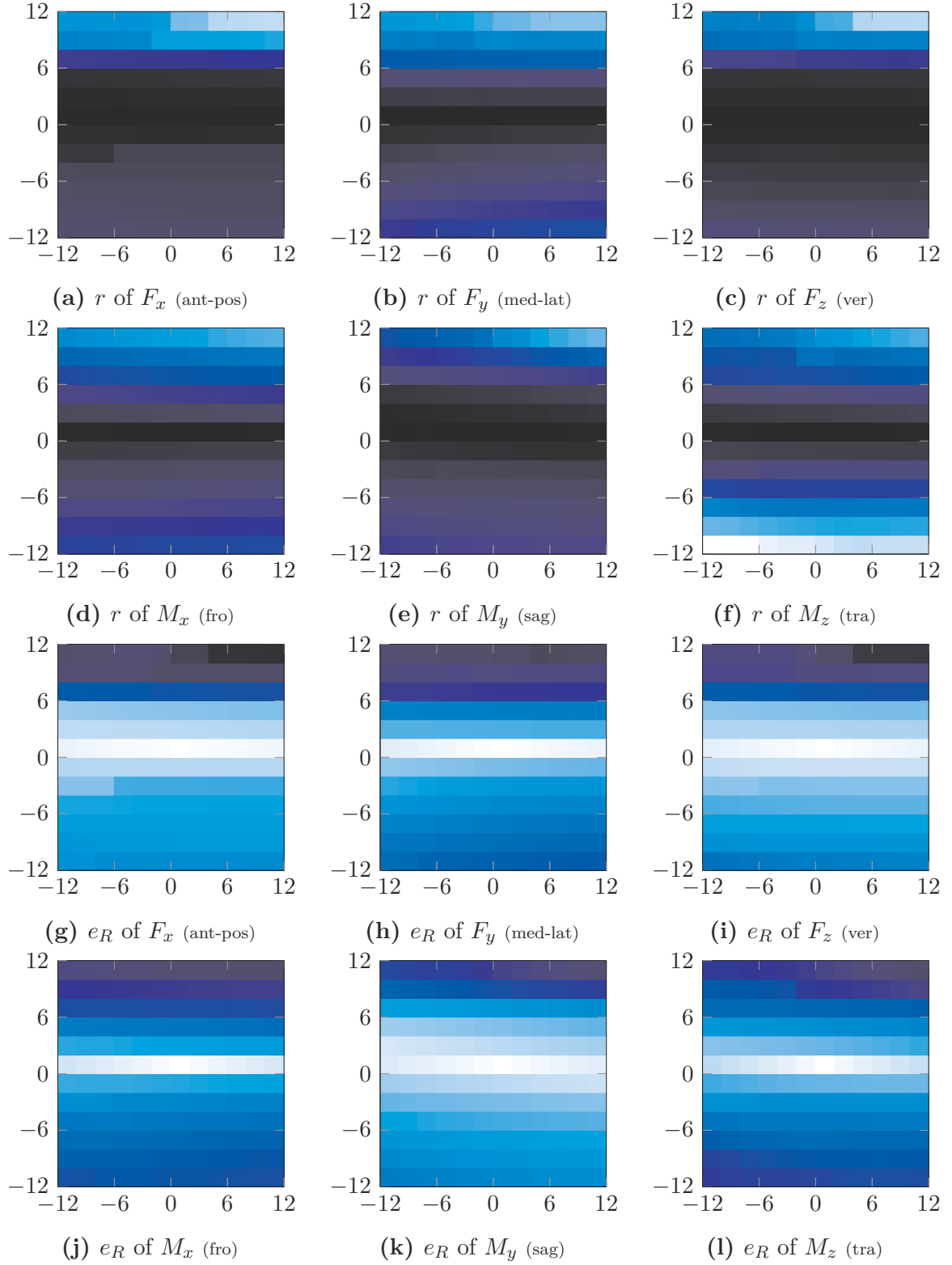


**Figure A.14:** Qualitative distributions for the shank I2S calibration errors with a lateral initial IMU calibration.

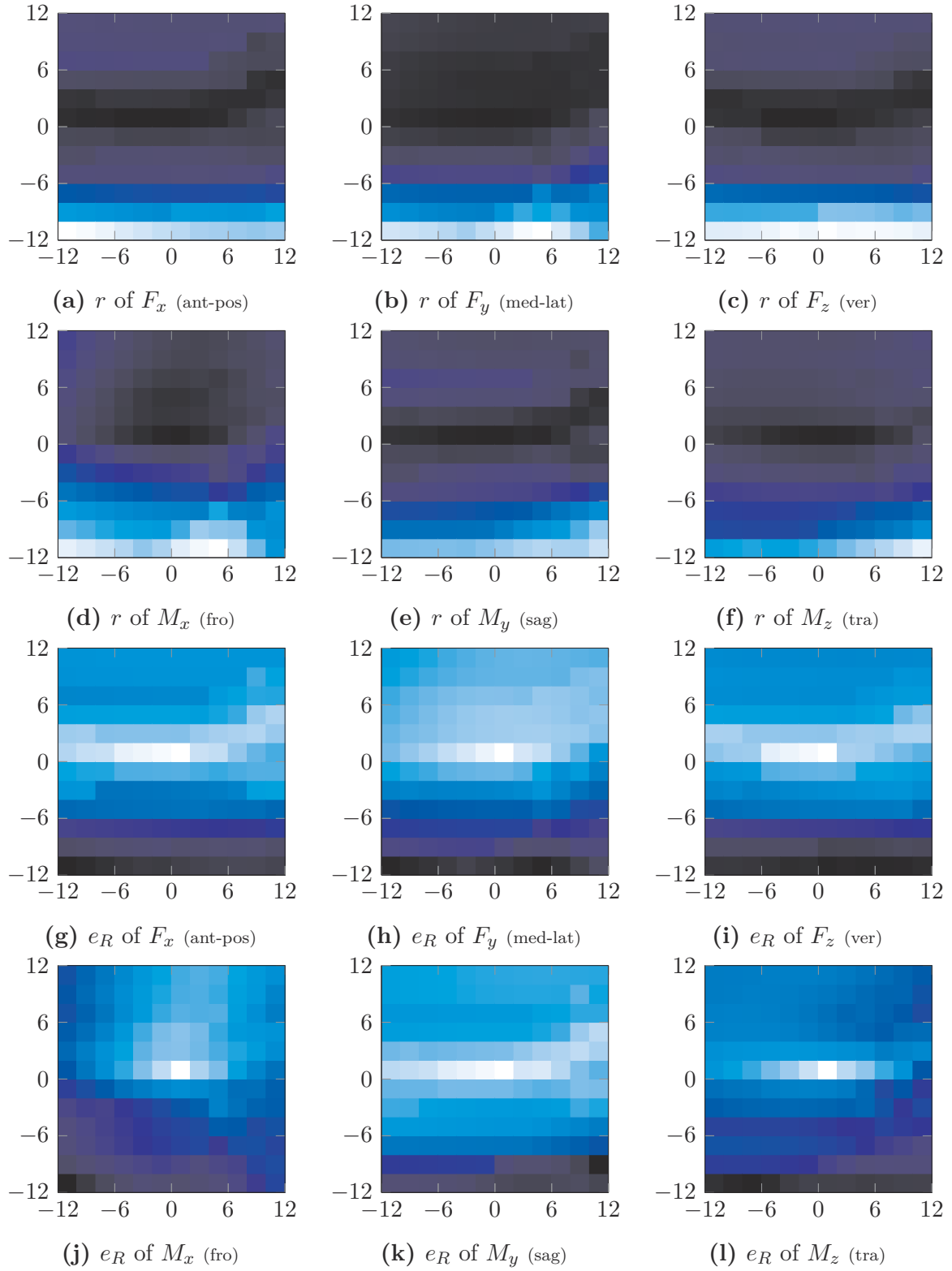


**Figure A.15:** Qualitative distributions for the foot I2S calibration errors with a lateral initial IMU calibration.